Computer-aided design of nanostructures from self- and directed-assembly of soft matter building blocks

by

Trung Dac Nguyen

A dissertation submitted in partial fulfillment
of the requirements for the degree of
Doctor of Philosophy
(Chemical Engineering and Scientific Computing)
in The University of Michigan
2011

Doctoral Committee:

Professor Sharon C. Glotzer, Chair
Professor Nicholas A. Kotov
Professor John Kieffer
Associate Professor Joerg Lahann
Associate Professor Max Shtein

Acknowledgments

I would like to express my gratitude to my advisor, committee, professors, friends and family members whose guidance, support and encouragement are invaluable for me throughout my graduate study.

To my advisor, Professor Sharon Glotzer, I thank you for your guidance, caring and support, for the intellectual freedom you allowed me to pursue and for all the opportunities and resources you provided. Your ideas, vision and passion in doing research have inspired me a lot to continue my career as a researcher.

To Professor Walter Weber Jr., I thank you for encouraging me to apply for the Chemical Engineering PhD program at the University of Michigan, which turned out to be my only opportunity to come to the US at the time. I thank Professor Robert Ziff for his advice and support since my first days in the department and during my time as a graduate student instructor. I would like to thank my committee members, Professor John Kieffer, Professor Nicholas Kotov, Professor Joerg Lahann and Professor Max Shtein for their helpful suggestions, comments and discussions. It is my honor to have had opportunities to work with Professor Kotov and Professor Lahann in numerous exciting projects, some of which are the milestones for my study.

I am grateful to my mentors, Dr. Mark Horsch and Dr. Zhenli Zhang, for their advice and knowledge during my early years as a graduate student. I am very fortunate to have Dr. Chris Iacovella, Dr. Aaron Keys, Dr. Aaron Santos, Dr. Stephanie Teich-McGoldrick and Dr. Chetana Singh as my labmates. I thank you all for uncountable helpful instructions, discussions and sharing.

To my friends, Eric Jankowski, Sean Langelie and Amir Haji-Akbari, I deeply appreciate your company. I thank Eric and Sean for Go lessons, for delicious food, and for our great moments. I thank Eric and Amir for their knowledge, experience and fascinating discussions on every randomly picked issue. My special thanks to Dr. Kevin Kohlstedt for his friendship, instructions and caring. Your company brings me joy and makes my last six years memorable for the rest of my life.

I am thankful to the rest of the Glotzer group, especially Dr. Joshua Anderson, Dr.

Michael Engel, Dr. Hao Jiang, Carolyn Phillips and Tony Sheh from whom I learnt a lot over the years. I thank Daniel Ortiz, Benjamin Schultz, Richmond Newman, Nguyen H. P. Nguyen and Pablo Damasceno for many interesting, both scientific and non-scientific, discussions. I greatly appreciate Dr. Greg van Anders, Ben, Richmond and Karen Coulter for their comments and suggestions in writing this dissertation.

I acknowledge the Vietnam Education Foundation for giving me the opportunity to pursue my graduate study in the United States. I acknowledge the Vietnam Education Foundation, the Air Force Office of Scientific Research under MURI grant FA9550-06-1-0337, and the U.S. Department of Energy, Office of Basic Energy Sciences, Division of Materials Sciences and Engineering under Award DE-FG02-02ER46000 for funding resources.

I highly appreciate the Center of Advanced Computing, Scientific Computing program and Chemical Engineering department staffs, especially Susan Hamlin, for their constant support.

I would like to extend my thanks to Trinh D. Tran, Loc H. Khieu, Nguyen H. P. Nguyen, Hai T. Nguyen, Dr. Hai H. Dinh, Dr. Hoa T. Trinh, Dr. Lam K. Huynh, Dr. Xuan V. Tran, Dr. Thanh B. Do and my Ann Arbor Vietnamese ”family”. Ann Arbor has become my second home in your presence. Your company, encouragement and sharing will always be remembered and appreciated.

To my Dad and Mom, Dac V. Nguyen and Thu M. Nguyen, and my brother Phi D. Nguyen, I cannot say thank you enough for your love, support and encouragement. Despite the physical distance, I always have you by my side. I also thank my big family at home for their love and encouragement.

Finally, to my darling wife, Huong Le, since I cannot express my gratitude to your sweet love, unconditional patience and incessant encouragement in words, let me just say I owe you this beautiful life.

Table of Contents

List of Tables

Table

List of Figures

Figure

List of Appendices

Appendix

Abstract

Functional materials that are active at nanometer scales and adaptive to environment have been highly desirable for a huge array of novel applications ranging from photonics, sensing, fuel cells, smart materials to drug delivery and miniature robots. These bio-inspired features imply that the underlying structure of this type of materials should possess a well-defined ordering as well as the ability to reconfigure in response to a given external stimulus such as temperature, electric field, pH or light. Over the last decades, endless efforts have been made to seek fabrication approaches that are robust and scalable for massive production of such structures. In this regard, self- and directed- assembly have been shown as potential approaches by which target structures are assembled from bottom up via the self-organization of an enormous number of elements, so called assembling building blocks. Given a diverse collection of nanometer-sized building blocks now available in various materials, shapes and compositions, we wish to find ”recipes” for assembling structures analogous to those that are known to have interesting properties in molecular and biological systems and functional at visible optical wavelengths.

In this thesis, we employ computer simulation as a design tool, demonstrating that various ordered and reconfigurable structures can be obtained from the self- and directed-assembly of soft matter nano-building blocks such as nanoparticles, polymer-tethered nanoparticles and colloidal particles. We show that, besides thermodynamic parameters, the self-assembly of these building blocks is governed by nanoparticle geometry, the number and attachment location of tethers, solvent selectivity, balance between attractive and repulsive forces, nanoparticle size polydispersity, and field strength. We demonstrate that higher-order nanostructures, i.e. those for which the correlation length is much greater than the length scale of individual assembling building blocks, can be hierarchically assembled. For instance, bilayer sheets formed by laterally tethered rods fold into spiral scrolls and helical structures, which are able to adopt different morphologies depending on the environmental condition. In addition to the reconfigurability of these hierarchically assembled helices and scrolls, we find that a square grid structure formed by laterally tethered nanorods can be transformed into a bilayer sheet structure, and vice versa, upon shortening, or lengthening,

the rod segments, respectively. From these inspiring results, we propose a general scheme by which shape-shifting particles are employed to induce the reconfiguration of pre-assembled structures. Finally, we investigate the role of an external field in assisting the formation of assembled structures that would not be accessible from self-assembly. As an example, we show the assembly of magnetic Janus particles with a highly ordered alignment and a tunable gradient density, which are likely to be applicable to photonic band gap materials. Our results and proposed methods serve not only as proofs of concept for designing functional nanostructured materials via ”bottom-up” approaches, but also to inspire further theoretical and experimental investigations.

Chapter 1
Introduction

1.1 Motivation

Mother Nature does an excellent job of creating sophisticated biological molecules and microstructures that are able to adapt to their surrounding environment. One of today's most appealing topics, nanotechnology, aims to extend what Mother Nature has done for the biological world, i.e. to fabricate functional nanostructures with arbitrary complexity that are able to adapt to environmental cues such as temperature, solution pH or electromagnetic field. Such novel reconfigurable structures would lead to our next generation of "smart" nanomaterials that should be useful in a wide variety of applications ranging from photonic band gap materials, negative refractive index materials, biosensing, drug delivery to nano-generators and nano-robots. Over the past decades, tremendous efforts have been made to realize optimal methods as well as to provide an increasingly powerful toolkit for the realization of these materials in the foreseeable future.

Notable advances in synthesis techniques have brought about a vast library of nanoscale building blocks that are greatly diverse in material, well controlled in shape and highly uniform in size. More interesting are unprecedented soft matter building blocks recently synthesized such as non-trivially shaped nanoparticles, polymer-tethered nanoparticles, lock-and-key colloidal particles and multi-compartmental particles[1–9]. The shape of the building blocks can even be manipulated, for example, upon heating and cooling, during and after their assembly[10–13]. The adaptability of the building blocks in response to changes in their environment, reminiscent of biological molecules, naturally makes them relevant for consideration in the context of reconfigurable assembled structures.

Pioneering experimental and computational studies have shown that "bottom-up" approaches such as self- and directed- assembly are advantageous over traditional top-down methods such as optical lithography and direct writing due to their scalability, robustness and cost-effectiveness. By varying thermodynamic parameters or by applying external potentials, we could expect to get control over the self-organization of elementary building

blocks such as block copolymers, nanoparticles and colloidal particles so that they assemble into target nanostructures. Numerous assembled structures have been reported with one-, two- and three-dimensional periodicity and with a high degree of complexity, for example, double gyroids, alternating diamond networks, face-centered cubic colloidal crystals and quasi-crystalline structures. Structures of far greater complexity can be synthesized when hierarchical assembly is involved. For example, polymer-tethered nanorods assemble into a flat sheet on a templated substrate in which the rods are perpendicular to the plane[8]. When the substrate is removed, the flat sheet folds into a tube, or a hollow sphere, or a hollow hemisphere depending on the geometry of the template upon heating. As another example, Srivastava and co-workers demonstrated that cadmium telluride (CdTe) tetrahedra first assemble into a crystalline bilayer ribbon with a finite width. The ribbons subsequently twist into helices with a tunable pitch upon adjusting the illumination density[14]. These inspiring results suggest that a combination of complexity and reconfigurability can be achieved with bottom-up techniques.

The availability of powerful assembly techniques and a versatile toolkit of assembling building blocks, as mentioned above, strongly motivate us to further the complexity of assembled nanostructures to another level. Since current experimental findings are mostly specific to particular systems, a generic and systematic design framework for engineering reconfigurable nanomaterials would be desirable from both theoretical and experimental perspectives. Over the past five years, such a framework has been developed step by step by experimental and computational studies. Previous simulations provided not only further insights into the self-assembly of various shape amphiphiles, nanoparticles and colloidal particles but also reliable predictions on fascinating possibly assembled structures[15–21]. As an effort to contribute to the design framework, in this thesis we are using computer simulation as a design tool to address the following topics:

(1) Identifying the key factors that influence the assembly of soft matter building blocks such as polymer-tethered nanoparticles and nanoparticles. Besides thermodynamic parameters, we show that the influential factors include nanoparticle geometry, the number and attachment location of tethers, solvent selectivity, balance between attractive and repulsive forces, nanoparticle size polydispersity, and field strength.

(2) Designing higher-order nanostructures, i.e. those for which the correlation length is much greater than the length scale of individual assembling building blocks. We show that bilayer sheets formed by laterally tethered rods fold into spiral scrolls and helical structures, which are able to adopt different morphologies depending on the environmental condition.

(3) Designing reconfigurable assembled structures. In addition to the reconfigurability of the hierarchical assembled helices and scrolls upon changes in their effective interactions,

we find that a square grid structure formed by laterally tethered nanorods can be transformed into a bilayer sheet structure as the rod segments is shortened, and vice versa. From these inspiring results, we propose a general scheme by which shape-shifting particles are employed to induce the reconfiguration of pre-assembled structures.

(4) Investigating the role of an external field in assisting the formation of assembled structures that would not be accessible from self-assembly. As an example, we show the assembly of magnetic Janus particles with a highly ordered alignment and a tunable gradient density, which are likely to be applicable to photonic band gap materials.

Given the close relation between simulation, experiment and theory in nanoengineering, we expect that our findings can not only serve as proofs of concept for designing reconfigurable nanostructures from bottom-up approaches, but also inspire experimentalists and theorists for further explorations.

1.2 Overview

This thesis is structured as follows: Chapter 1 discusses the motivation for conducting the studies in this thesis. Chapter 2 provides the fundamentals of soft matter building blocks: their fabrication, assembly methods and the applications of their assemblies. We discuss the coarse-grained models, simulation methods and packages extensively used throughout this thesis. In Chapter 3, we introduce our implementation of rigid body constraints in HOOMD-blue, a GPU-accelerated molecular dynamics package, hosted by the Glotzer group.

Chapter 4 investigates the equilibrium self-assembly of two types of soft matter building blocks. This chapter emphasizes key factors that influence the formation of self-assembled structures: building block anisotropy and force balance. We present the self-assembly of end- and laterally-tethered V-shaped nanoparticles in a selective solvent and a melt-like condition where the shape anisotropy plays a vital role. The phase diagrams of single end-tethered, double end-tethered and laterally-tethered V-shaped nanoparticles are reported.We also investigate the self-assembly of polydisperse nanoparticles into uniform size supraparticles in which a generic force balance allows for excellent control in the aggregate size. The self-limiting aggregation mechanism is shown to be applicable to various nanoparticle systems.

Chapter 5 focuses on the hierarchical self-assembly of laterally tethered nanorods. We show the formation of different higher-order morphologies from the scrolling of a bilayer sheet depending on the local packing of the assembling rods and solvent conditions. The

characteristic length of these structures is much greater than that of individual building blocks, and can be tuned by temperature and other environment factors. Interestingly, these hierarchically assembled structures are able to reconfigure under changes in the environmental conditions. The findings in this chapter serve as a proof-of-concept for a non-conventional design approach to engineering higher-order morphologies.

Chapter 6 furthers the results in the previous chapter by examining the ability of assembled structures to reconfigure under changes in the environment and building block geometry. We show that when the rod segments are shortened or lengthened, the assembled structure formed by laterally tethered rods reconfigures from a square grid phase to a honeycomb phase. We subsequently extend those results by proposing a generic strategy for engineering novel nanostructures with shape-shifting particles. We show that transforming the particle shape in an ordered structure could yield (i) more efficient assembly than self-assembling from disordered states at the same temperature, (ii) reconfigurability between ordered structures, and (iii) pathways to target structures that are inaccessible with traditional self-assembly approaches. The structural reconfiguration can also be induced by an external potential. We demonstrate the unique switching assembly of magnetic Janus particles driven by a gradient magnetic field. The reconfiguration of assembled structures either with shape shifting or with external potentials suggests many possibilities of designing functional nanostructures from bottom up.

Chapter 7 summarizes the contributions and discusses the outlook of this thesis.

Appendix A mentions the standard analysis tools used in the thesis including shape-matching order parameters. Appendix B presents preliminary results and ongoing work including the self-assembly of lock-and-key colloidal particles and patchy particles. Appendix C introduces the software VisualizerX for visualization and data analysis including the radial distribution function, bond order diagram and diffraction pattern.

Chapter 2
Background

In this chapter, we present a brief overview of the fabrication and assembly techniques of soft matter building blocks such as nanoparticles and polymer-tethered nanoparticles and potential applications of their assemblies. Since the unique anisotropy of these building blocks necessitates suitable modeling and simulation treatments, we discuss the general models used extensively throughout this thesis, which despite their simplicity are able to capture key interactions between these building blocks at nanometer and nanosecond scales. We explain the motivation for choosing molecular dynamics and Brownian dynamics as simulation methods. Other important topics such as numerical integrators, rigid body constraints and simulation procedure are also discussed. Finally, we introduce the simulation packages developed and employed including our own C++ code, HOOMD-blue and LAMMPS.

2.1 Assembly of soft matter building blocks

Soft matter refers to physical states in which the characteristic energy scale is comparable to thermal fluctuations or stresses at room temperature, for example, liquids, foam, gels and biological materials. To date, soft matter materials have been extensively used in a host of applications including optical and electronic devices, photovoltaics, biosensing and photonic band gap materials. It is the self-organization of the elementary components of soft matter materials, so called soft matter building blocks, such as block copolymers, nanoparticles, colloids and biological supramolecules at mesoscopic length scales (10-1000nm) that gives rise to interesting physical properties that are unavailable at both atomic and macroscopic levels. Central to the design of novel nanostructured materials are to tailor suitable building blocks and to control their assembly in an efficient and robust way. In the following sections, we discuss the fabrication and assembly of nanoparticles and polymer-tethered nanoparticles and the applications of their assemblies.

2.1.1 Fabrication

Over the last decade, the fabrication of nanoparticles has been of rapidly growing interest not only because individual NPs exhibit promising nanoscale opto-electronic properties but also because they are able to assemble into novel nanostructured materials. One of the most striking features of NPs is that their photonic and electronic properties are strongly dependent upon their size, shape and composition. Tremendous progress in synthesis techniques has been made, aiming at controlling these parameters for high yield and uniformity. NPs are now synthesized in different materials including semiconductor, metal and metallic oxides, and in different shapes (e.g. spheres, rods, cubes, polyhedra, triangular plates, hexagonal plates, stars, Vs) with size ranging from tens to hundreds of nanometers[22].

There are several ways to categorize currently available NP fabrication methods, for example, based on the environmental conditions (gas phase and aero-sol phase) or based on the preparation procedure (seed-mediated growth and redox transmetallation). Seed-mediated growth process has become a very popular method to control the nanoparticle shape. Seed-mediated growth fabrication typically involves two stages[22]. In the first stage, the material seeds are formed via a fast rate reaction in which the core materials are concentrated. The seeds are in general spherical in shape and 1-5nm in size. In the second stage, the reaction is slowed down and the seeds are slowly grown in size in the presence of stabilizers or capping agents. In many cases, the stabilizers play an important role in determining the final shape of the NPs by facilitating the crystallization growth of the precursors along particular directions while restricting others. For example, cobalt nanocrystals stabilized with alkylamine ligands on their 001 crystalline planes are limited to grow within the x-y plane, resulting in disc-shaped nanoparticles[11]. Another approach is to combine primitive components, e.g. rods, cubes and tetrahedra, into other shapes. As examples, V-shaped particles can be obtained from two rods and a tetrahedron or L-shaped particles from two rods and a cube. Manna demonstrated that growing rods on the four 111 planes of zinc blend tetrahedron cadmium selenide (CdSe) seeds results in nano-tetrapods[23]. Other parameters such as growth temperature, monomer concentration and the functional group and concentration of stabilizers were shown to have significant effects on the geometry of the resulted building blocks.

The functional group of the stabilizer, which may be polarized, solvo-phobic or solvophilic depending on the solvent condition, helps determine the short-ranged interaction between NPs. Tang et al. reported the formation of cadmium telluride (CdTe) tetrahedra coated with thioglycolic acid (TGA) molecules or 2-(dimethylamino)ethanethiol (DMAET) molecules; the former is negatively charged while the later positively charged and hydrophobic[24]. Furthermore, certain stabilizers (e.g. cetyltrimethylammonium bromide

(CTAB)) can react with polymers or biological molecules (DNAs and proteins), allowing for tethering the NPs with those molecules. Westenhoff et al. demonstrated that CdTe nanospheres are anchored to a polyelectrolyte film via anionic polyethylene glycol (PEG) tethers[2]. Parak and coworkers showed that the number of attached tethers on the surface of oligonucleotide-coated gold nanospheres can be controlled[1]. Pan et al. functionalized gold nanorods and nanospheres with nucleotides[6]. They also obtained an exotic nanoparticle shape composed of a nanorod and a nanosphere using nucleotide hybridization. DeVeries et al. placed polymeric molecules specifically at two polar defect positions, which are diametrically opposed on the surface of ligand-coated metal nanoparticles[4]. These polar defects result from the ordered phase separation in the monolayer coating. Nie et al. reported creating a polymer di-tethered gold nanorod, which is an intriguing mesoscopic analogy of an amphiphilic triblock copolymer[5]. The CTAB-coated gold nanorod, which is on average 8nm in diameter and 42nm long, is attached with multiple polystyrene chains at each end. These encouraging results suggest that precisely controlled fabrication of polymer-tethered shape nanoparticles can be achieved in the near future.

2.1.2 Self- and directed-assembly

Functional nanostructures are often of a length scale much bigger than individual building blocks. Self- and directed- assembly have been considered as powerful approaches for manipulating a large number of nanoscale building blocks into specific structures[25]. These bottom-up methods are advantageous over top-down methods like optical lithography and direct writing in the sense that they allow for scalable low-cost processing. The key challenge, however, is to design assembling rules that ensure the target structures be efficiently and reliably produced. During the last two decades, a massive body of experimental and theoretical work has been carried out to address this challenge.

In a self-assembly process, nanoscale building blocks spontaneously organize themselves under thermodynamic constraints. The driving force for this behavior is the minimization of free energy. For instance, a system of rod particles undergoes a liquid-nematic transition upon compression so as to minimize their potential energy while maximizing their orientational entropy. Likewise, a solution of amphiphilic end-tethered nanorods at a certain range of rod-tether relative volume fraction and concentration exhibits a microphase separation upon cooling, forming a double gyroid structure to minimize the interfacial tension while maximizing the rod-rod contacts and tether free volume[26]. While self-assembly processes governed by equilibrium thermodynamics in principle result in thermodynamically and mechanically stable structures, they are inevitably subject to unfavorable kinetic effects.

Engineering self-assembled structures essentially involves "tailoring" assembling building blocks[15, 27–29], tuning their effective interactions[30], and finding assembly pathways to avoid or overcome these kinetic traps[31].

Methods for designing self-assembled structures can be loosely divided into two approaches, namely inverse engineering and forward engineering. In the inverse approach, the goal is to find optimal interactions and interaction rules between assembling building blocks that stabilize a given target structure. For example, Torquato and coworkers using inverse statistical mechanical methods find optimal interactions between spherical particles that result in particular types of amorphous solids, quasicrystalline and crystalline structures within a certain range of density under melting temperature[32]. The parameterized interactions are optimized so as to maximize the target structure's energetic stability with respect to competing structures (previously chosen) under mechanical stability constraints. Hozmoz et al. designed optimal interaction rules between individual colloidal particles that substantially enhance the equilibrium probability of forming particular 2-, 4- and 8-particle clusters[30]. Although this approach provides the fundamental mathematical relationship between structural features and interactions, and by construction, can be applicable to arbitrary target structures, it is not always guaranteed that the optimized interactions could be attained in physical systems, and that the assembled structures would spontaneously emerge upon cooling from disordered states.

In the forward approach, the goal is to find assembled structures by rationally tailoring assembling building blocks and/or tuning their interaction strength and range. In this regard, the building blocks are functionalized with complementary DNA strands and attractive patches so that their self-assembly is favored towards specific target structures. For instance, Nie et al. demonstrated that gold nanorods functionalized with multiple polystyrene chains at two ends assemble into chain-like aggregates as desired[5]. Zhang and Glotzer predicted via simulation that patchy particles self-assemble into target diamond structures, rings, icosahedral clusters or sheets depending on the arrangement and geometry of the "sticky" patches[27]. While the target structures are known *a priori* only in certain cases, this approach is widely pursued because (i) it provides the fundamental knowledge of thermodynamic and structural behaviors, (ii) the building block interactions are experimentally justifiable, and (iii) the resulting assembled structures, if thermodynamically stable, are very likely to spontaneously emerge upon cooling from disordered states.

In 2003, Zhang, Horsch, Lamm and Glotzer proposed a remarkable and novel forward design framework by which the self-assembly of nanoparticles is facilitated by attaching to them a finite number of immiscible polymeric tethers at specific sites[15]. In a selective solvent, the immiscibility between the nanoparticles and their tethers leads to microphase

separation, similar to amphiphilic flexible block copolymers. Moreover, the phase behavior of these polymer-tethered nanoparticles becomes more sophisticated due to their asymmetric nature. That asymmetry, often termed as the building block anisotropy, characterized by the nanoparticle geometry and the number, attachment location and relative volume fraction of the tethers, adds a lot more flexibility to designing assembling building blocks[33]. Coupled with thermodynamic parameters and solvent selectivity, the building block anisotropy has been shown to have profound influence on the morphology of assembled structures. Follow-up mesoscale simulation studies have investigated the phase diagram of mono- and di-tethered spheres[34–36], end- and laterally- tethered nanorods[17–19], vertex- and facet-tethered nanocubes[20, 21, 37], end- and laterally-tethered V-shaped particles[38]. Examples of ordered assemblies observed in these studies include body-centered cubic micelles, hexagonally packed cylinders, double gyroid and diamond networks formed by tethered nanospheres[34–36]; tetragonally packed perforated lamellae, bilayer lamellar and tilted smectic phases formed by end-tethered nanorods[19]; chiral tilted smectic phase and honeycomb phases formed by tethered V-shaped particles[38].

Unlike in self-assembly, in a directed assembly process the organization of the building blocks is strongly driven by an external potential, for example, an electromagnetic field, gravity or a shear flow. In this case, the energy scale of the external field is often much greater than thermal energy. Applying external fields to guide the particle assembly is often employed as a complementary tool to self-assembly for a number of reasons[39]. First, applied fields may suppress gelation or kinetically trapped configurations that hinder or compete with equilibrium states, allowing the system to better explore the configuration space. Second, the building blocks may respond to changes in the applied field gradient or orientation, resulting in unusual non-equilibrium structures that are otherwise inaccessible. Third, from the experimental point of view, using an external field facilitates the search for interesting regimes in the phase diagram of the building blocks. However, care should be taken as the applied field may alter the phase diagram in an unexpected way or stabilize new phases. The flexibility of using external potentials lies in the way the field strength can be varied temporarily or spatially. Peng et al. showed that by applying an in-plane gradient magnetic field, the density of magnetic particles can be tuned spatially[40]. For Janus particles on a substrate, for which one of the hemispheres is conductive, staggered chains form as an electric field is applied parallel to the plane. An AC electric field can polarize colloidal rods and the induced dipole interaction gives rise to the angle alignment of the rods with the field direction[41]. In Chapter 6, we investigate an interesting application of a lateral gradient magnetic field to the assembly of Janus particles.

2.1.3 Applications of soft matter assemblies

Experiments have reported an enormous collection of nanostructures with one-, two- and three-dimensional periodicity formed by soft matter building blocks. These ordered structures have been shown to have unique properties that are inaccessible at both molecular and micron-sized scales. For example, two-dimensional ordered arrays formed by binary mixtures of nanoparticles can be used in novel electronic and optoelectronic applications[42, 43]. Diamond-cubic and quasicrystalline structures formed by di-tethered spheres may possess a robust photonic band gap at visible wavelengths[44]. Wires formed by metallic nanoparticles can be used in electric nano-circuits due to their enhanced conductivity along the long axis[45]. Helical structures formed by oblate particles and laterally tethered nanorods can provide unusual electronic properties along their columnar axis, or optical properties similar to cholesteric liquid crystals[46, 47]. Body-centered cubic and face-centered cubic crystalline structures formed by most of tethered nanoparticles are applicable to photonic crystals[44]. Chiral tilted smectic phases formed by achiral building blocks such as tethered V-shaped nanoparticles, similar to those observed in bent-core liquid crystals, may find themselves in novel optical applications as their characteristic length scale is in the range of visible wave lengths[48]. Applications of soft matter assembled structures can be found in solar cells[43], biosensing[49] and drug delivery[50] (also see the references therein) and more.

In summary, we have described how recent breakthroughs in the fabrication of nanoparticles and tethered nanoparticles have enabled opportunities to tailor building blocks with a high degree of shape complexity. We described how the organization of these nanoscale building blocks into interesting functional microscopic structures can be driven by thermodynamics (self-assembly) or by an external stimulus (directed-assembly). We have discussed the motivation for pursuing the forward design approach by briefly comparing it with the inverse engineering approach. From that, computer simulations naturally arise as a powerful tool to aid experimental and theoretical studies in designing nano building blocks and optimal assembling rules to obtain novel nanostructures. The following section will discuss the general model and simulation methods used throughout this thesis.

2.2 Simulation models, methods and packages

Improvements in computing power and techniques allow unprecedentedly close connection between experiment, theory and computer simulation. Simulation methods based on well-established theoretical foundations such as statistical mechanics and thermodynamics

allow for the validation of computer experiments. Furthermore, using computer simulations, one can not only broaden the investigated parameter space that is comparatively limited in experiments, but also have further insights into phenomena for which there is no guiding theoretical formulation. In particular, computer simulations are appropriate for designing nanostructures from the assembly of soft matter building blocks for two reasons. First, the building block anisotropy manifests itself through a large number of parameters such as the geometry of the nanoparticle, the number, length and attachment location of the tethers, nanoparticle-tether relative volume fraction, and so on. These parameters can be varied more rapidly and cost-effectively along corresponding ”axes of anisotropy” in computer simulations than in experiments.

Second, to date, there has been little theoretical progress reported in understanding the phase behavior of this building block family, probably due to their multidimensional anisotropy. By simulating coarse-grained models, we can identify the key factors that influence the physics of particular systems, for example, charge-dipole interaction, nanorod aspect ratio, nanosphere diameter, and tether bulkiness.

Developing models of physical systems that are suitable for computer simulation, by necessity, throws away some of the details of the system. This process, however, is far from arbitrary, in that considerable care must be taken to eliminate the details of the system that are irrelevant to the behaviors of interest, and to accurately characterize those that are key driving forces. Once a suitable coarse-grained model has been developed, a suitable simulation method must be chosen.

2.2.1 Models

Coarse grained models

We adopt generic, coarse-grained models to capture the essential physics of the studied systems similar to those that have been used extensively in the literature for soft matter systems. Each model building block is composed of a finite number of spherical beads: the beads in a rigid component are rigidly glued forming a specific shape; and those in a flexible polymeric tether are connected via finitely extendable nonlinear elastic (FENE) or harmonic springs. Using this bead-spring model, we can straightforwardly capture: (1) the geometry of the rigid components, (2) the flexibility of the tethers, (3) the attachment location of the tethers for tethered NPs, and (4) the location and width of the patches for patchy particles.

Force field

At nanometer scales, the interactions between the building blocks primarily involve excluded volume interactions, van der Waals interaction, screened electrostatics, solvophobic and solvophilic interactions, depletion forces and other molecular surface interactions. These interactions can be approximated by empirical pair potentials that have been widely used for block copolymers, surfactants, nanoparticles, colloids and other soft matter systems. For example, the van der Waals interaction and screened Coulombic interaction between charged surfaces in a solvent with dielectric contrast can be analytically modeled by the well-known DLVO potential[51–53]. In mesoscale coarse-graining modeling applications, the interaction between the particles and solvent molecules (and other supplementary agents) is often captured implicitly in the effective interaction between the particles. As such, the interaction between solvophilic (or hydrophilic) species can be modeled by an effective repulsion to reflect the tendency of the particles to maximize their energetically favorable contact with the solvent[51]. Meanwhile, the interaction between solvophobic (or hydrophobic) species can be modeled by a net attraction due to the enthalpic and entropic effects of solvent molecules tending to maintain their structure and mobility surrounding the particles. When colloidal particles are immersed in a sea of small non-absorbing polymer molecules, the particles are effectively "attractive" to each other as the polymer molecules tend to escape from the depletion region between the particles. This entropic force can be modeled by an attractive potential of mean force[51, 52]. Rigorous efforts are therefore required to develop an interaction model that fully captures those system-specific details[52]. In this thesis, we "coarse grain" over these details by using effective interactions to encapsulate qualitatively both energetic and entropic forces between the building blocks. For this purpose, the 12-6 Lennard-Jones (LJ) potential, which is originally used for modeling molecular systems, becomes our natural choice: its infinite repulsive term ($1/r^{12}$) represents the excluded volume interaction and its attractive term ($-1/r^6$) embodies the net attractive interaction. The interaction strength and range of the LJ potential can be adjusted independently as shown below. The LJ potential can also be superimposed with charge-dipole and dipole-dipole interactions when these interactions are considerable.

The effective attraction due to the van der Waals interaction and solvophobic interactions is modeled by the LJ potential truncated and shifted to zero at $r_C = 2.5\sigma$. We only consider the cases when the interactions are short-ranged due to the fact that the building blocks are often in aqueous conditions of finite dielectric constant, in which long-ranged electrostatic

interactions are strongly screened.

$$U_{LJ}(r) = \begin{cases} 4\varepsilon\left[\left(\frac{\sigma}{r}\right)^{12} - \left(\frac{\sigma}{r}\right)^{6}\right] + 4\varepsilon\left[\left(\frac{\sigma}{r_C}\right)^{12} - \left(\frac{\sigma}{r_C}\right)^{6}\right], & r \le r_C = 2.5\sigma \\ 0, & r > r_C = 2.5\sigma \end{cases} \tag{2.1}$$

where r is the center-to-center distance between two beads, ε is the energy well depth, σ is the length unit, being the bead diameter unless stated otherwise. For two beads differing in their diameter, the potential is shifted to the particle surface:

$$U_{LJ-shifted}(r) = \begin{cases} 4\varepsilon\left[\left(\frac{\sigma}{r-\delta}\right)^{12} - \left(\frac{\sigma}{r-\delta}\right)^{6}\right], & r \le r_C + \delta \\ 0, & r > r_C + \delta \end{cases} \tag{2.2}$$

where $\delta = (D_1 + D_2)/2 - \sigma$, D_1 and D_2 are the bead diameters. The interaction scale can be adjusted by varying ε; meanwhile, the interaction range can be tuned by varying σ and/or δ.

The repulsion between species due to their excluded volume interaction and hydrophilic interaction are modeled by the LJ potential truncated at its minimum and shifted to zero, often termed as the Weeks-Chandler-Andersen (WCA) potential[54]:

$$U_{WCA}(r) = \begin{cases} 4\varepsilon\left[\left(\frac{\sigma}{r}\right)^{12} - \left(\frac{\sigma}{r}\right)^{6}\right] + \varepsilon, & r \le r_C = 2^{1/6}\sigma \\ 0, & r > r_C = 2^{1/6}\sigma \end{cases} \tag{2.3}$$

Screened electrostatic interactions including charge-charge, charge-dipole and dipole-dipole interactions are superimposed to the pair potential based on the relevant physics of interest. The pair potentials used for these interactions will be mentioned when necessary.

The bonds between adjacent beads in a flexible tether and between a tether bead and a nanoparticle bead are modeled by FENE springs of which the elastic energy is given by[55]:

$$U_{FENE}(r) = \frac{1}{2}kR_0^2 \ln\left[1 - \left(\frac{r}{R_0}\right)^2\right] \tag{2.4}$$

where $R_0 = 1.5\sigma$ is the equilibrium distance. Unlike harmonic springs, FENE springs do not allow the bond length exceeds R_0 because the potential goes to infinity otherwise. The value of 1.5σ is chosen as to avoid crossing bonds. Note that in practice the FENE springs are coupled with the WCA potential to prevent the connected beads from overlapping.

The simulations are performed in reduced units so that the results are independent of

any specific chemistry. In most cases, we choose the natural units of the system based on the bead diameter (σ), bead mass (m), energy scale (ε). The time unit is then defined as $\tau = \sigma\sqrt{m/\varepsilon}$. For soft matter systems, typical values of these quantities are σ = 1-5nm, $m = 10^{-21} - 10^{-20}$kg, ε = 50-60kJ/mol, giving τ = 0.5ns. For self-assembly simulations, the energy scale is typically in the order of thermal energy, i.e. ε = 0.1-10k_BT. For directed assembly simulations, the energy scale of the external field is much greater than the thermal energy.

2.2.2 Simulation method

For soft matter systems of typical length scale (10-1000nm) and time scale (1ns-1ms), mesoscale simulation methods such as Brownian dynamics (BD), dissipative particle dynamics (DPD) and Monte Carlo (MC) simulations are widely preferred[52, 56]. In molecular dynamics based methods such as BD and DPD, the particles' position and velocity are determined by integrating the equation of motion according to the Newton's second law. The primary driving force on individual particles is the conservative force coming from the gradient of the interaction energy. The presence of additional forces such as dissipative forces and random forces models the effects of implicit solvent molecules. The time trajectory of the particles obtained from BD simulations represents the set of microstates in the canonical configuration space, providing time-averaged thermodynamic properties (e.g. temperature, pressure), structural properties (e.g. structure factor, diffraction pattern) and transport properties (e.g. diffusion coefficient, shear viscosity, thermal conductivity) of the system. Meanwhile, Monte Carlo simulations sample the configuration space based on the assumption that each accessible microstate of the system is associated with a given probability density function, which is valid for a system at equilibrium. The thermodynamic and structural properties of the system are then calculated based on an ensemble average. In this thesis, we choose molecular dynamics based methods, particularly, MD and BD, over Monte Carlo methods for the following reasons. First, we are interested in both thermodynamic and dynamic properties. The latter is important when the system is not necessarily in equilibrium. Second, since soft matter building blocks such as polymer-tethered nanoparticles consist of both rigid and flexible components and their assembly behavior of interest spans a wide range of volume fraction, Monte Carlo simulations are computationally expensive as compared to molecular dynamics based methods. Finally, massively parallel molecular dynamics simulation packages exist to allow simulations to be performed very quickly.

Molecular dynamics

Consider a system of N particles with positions $\mathbf{x}^N = (\mathbf{x}_1, \mathbf{x}_2, .., \mathbf{x}_N)$ and conjugate momenta $\mathbf{p}^N = (\mathbf{p}_1, \mathbf{p}_2, .., \mathbf{p}_N)$. The motion of individual particles is governed by the Newton's second law[56, 57]:

$$m\ddot{\mathbf{x}}_i(t) = \mathbf{F}_i^C(\mathbf{x}_i(t)) = -\nabla U(\mathbf{x}^N) \tag{2.5}$$

The equation indicates that the driving conservative force is given by the gradient of the potential energy $U(\mathbf{x}^N)$ evaluated at $\mathbf{x}_i$. In essence, MD simulations are performed by integrating the Newton's equation 2.5 to progress the particles' positions and momenta over time given the potential energy between interacting particles.

Another approach to look at the dynamics of the system is to use the Hamiltonian equations of motion[57, 58]:

$$\dot{\mathbf{x}}_i = \frac{\partial H}{\partial \mathbf{p}_i} = \frac{\mathbf{p}_i}{m_i} \tag{2.6}$$

$$\dot{\mathbf{p}}_i = -\frac{\partial H}{\partial \mathbf{x}_i} = -\nabla U(\mathbf{x}^N) \tag{2.7}$$

where the Hamiltonian of the system is defined as:

$$H(\mathbf{x}^N, \mathbf{p}^N) = U(\mathbf{x}^N) + K(\mathbf{p}^N) = U(\mathbf{x}^N) + \sum_i^N \frac{\mathbf{p}_i^2}{m_i} \tag{2.8}$$

where $U(\mathbf{x}^N)$ and $K(\mathbf{p}^N)$ are the potential energy and kinetic energy, respectively. Since we are considering the cases where the potential energy does not dependent upon particles' velocities and the kinetic energy is a homogeneous quadratic function of particles' velocities, the Hamiltonian is equal to the system total energy[58, 59]. The Hamiltonian equations of motion are derived from the Hamilton's Principle, or the principle of least action, which states that the system evolves to minimize the difference between the kinetic energy and potential energy[59]. The Hamiltonian equations of motion also imply that:

$$\frac{dH}{dt} = \frac{\partial H}{\partial t} + \frac{\partial H}{\partial \mathbf{x}_i}\dot{\mathbf{x}}_i + \frac{\partial H}{\partial \mathbf{p}_i}\dot{\mathbf{p}}_i = 0 \tag{2.9}$$

suggesting that the Hamiltonian, i.e. total energy in this case, is conserved during the time evolution. It follows that the $6N$ dimensional vectors $(\mathbf{x}^N, \mathbf{p}^N)$ obtained from integrating the equations of motion corresponding to the microstates with a given Hamiltonian in the phase space. As a result, performing MD simulations is equivalent to sampling configurations in

the microcanonical ensemble (NVE).

In soft matter systems, in which the characteristic energy scale is comparable to thermal energy, in order to map phase diagrams and reproduce experimental results, it is desired to modify the traditional MD to sample the system in other thermodynamic ensembles such as canonical ensemble (NVT) or isobaric-isothermal ensemble (NPT). For atomistic and molecular systems, this is normally done by deriving an extended Hamiltonian with the extra terms associated with the thermostat and/or barostat. The Hamiltonian equations of motion then include the equation of motion of the thermostat and barostat "positions" and "velocities". Further details on these methods are beyond the scope of this thesis and can be found in Reference [57]. For soft matter systems of interest, the dynamics of the particles is often in a much longer time scale as compared to that of solvent molecules, i.e. 10^{-9}s vs. 10^{-12}s, respectively. It is therefore physically well-motivated and computationally convenient to coarse grain over the motion of these molecules by incorporating their effects into the equation of motion of the particles. Dissipative particle dynamics (DPD) and Brownian dynamics (BD) are coarse-graining molecular dynamics based methods serving for that purpose whereby the equations of motion of individual particles are derived from Langevin dynamics[57]. The main difference between DPD and BD is that the former conserves momentum and thus reproduces hydrodynamic interactions while the latter does not, as described later.

In this thesis, we choose to use BD because (i) the inherent force field associated with DPD does not conserve the building block geometry but allows the particles to overlap; (ii) hydrodynamic interactions are not strictly required for assembling equilibrium structures[60]; and (iii) the implementation of BD in massively parallel codes is more straightforward than that of DPD.

Brownian Dynamics

In BD, in addition to the conservative force $\mathbf{F}_i^C$, each bead is subjected to random and drag forces $\mathbf{F}_i^R$ and $\mathbf{F}_i^D$, respectively, coming from the bombardment of surrounding solvent molecules, and its motion is governed by the Langevin equation[56]:

$$m_i\ddot{\mathbf{x}}_i(t) = \mathbf{F}_i^C(\mathbf{x}_i(t)) + \mathbf{F}_i^R(t) + \mathbf{F}_i^D(\dot{\mathbf{x}}_i) \tag{2.10}$$

Here m_i and $\mathbf{x}_i$ are the bead mass and position, respectively. The conservative force $\mathbf{F}_i^C$ is determined by the gradient of the pair-wise potentials between bead i and its neighbors within the pair potential cutoff. The random and dissipative drag forces represent the

bombarding effects of solvent molecules on a bead. The dissipative force is related to the bead velocity via Stokes' equation: $\mathbf{F}_i^D = -\gamma \mathbf{v}_i$, where γ is the friction coefficient and $\mathbf{v}_i$ is the bead velocity. The uncorrelated random force $\mathbf{F}_i^R$ has zero mean and relates to the dissipative force via the fluctuation-dissipation theorem:

$$\langle \mathbf{F}_i^R \rangle = 0 \tag{2.11}$$

$$\langle \mathbf{F}_i^R(t) \cdot \mathbf{F}_j^R(t') \rangle = 6\gamma k_B T / \Delta t \delta_{ij} \delta(t - t') \tag{2.12}$$

The combination of the random and drag forces serves as a thermostat for the system and helps to minimize numerical round-off errors that can accumulate during long simulation runs. Since the steady-state solution of the Langevin equation yields the Boltzmann distribution, BD simulations sample the canonical ensemble (NVT). We should note that due to the uncorrelated random forces exerted on individual particles, hydrodynamic interactions between particles are neglected, and hence, momentum is not conserved in BD. However, the lack of momentum conservation in equilibrium self-assembly does not affect the resulted structures if they are thermodynamically stable, as shown in Reference [60].

Velocity Verlet integrator

There are various methods to integrate the equations of motion 2.5 and 2.10 over time, for example, leap-frog algorithm, predictor-corrector algorithm, Runge-Kutta algorithm, Verlet and velocity Verlet algorithms[56, 57]. According to the Lyapunov instability, the obtained trajectory in an NVE simulation always diverges exponentially from the true trajectory over time with a given initial condition regardless of the numerical integrator. Nonetheless, this is not a serious problem to our study because we wish to measure macroscopic (time average) properties, not the exact time trajectory, of the system. Any integrator that samples correctly the desired thermodynamic ensemble would be sufficient[57]. This means the coordinate transformation made by the integrator from t to $(t + \Delta t)$ should be canonical, or equivalently, the volume of the sampled phase space should be preserved. Among above-mentioned methods, the leap frog and velocity Verlet algorithm are proved to preserve a pseudo-Hamiltonian, which converges to the true Hamiltonian of the system as the time step is infinitely small. As a result, these algorithms ensure the time trajectory conform to the expected thermodynamic ensemble given an explicit Hamiltonian[57]. The velocity Verlet algorithm has been implemented, and is even the default integrator, in various well-known MD packages such as DL_POLY[61], NAMD[62], LAMMPS[63] and HOOMD-blue[64].

In the velocity Verlet algorithm, each integration step consists of two stages[56, 57].

The first-half integration stage involves updating momenta by half time step and positions by full time step with the newly updated momenta:

$$\mathbf{v}(t+\Delta t/2) = \mathbf{v}(t) + \frac{\mathbf{f}(t)\Delta t}{2m} \tag{2.13}$$

$$\mathbf{x}(t+\Delta t) = \mathbf{x}(t) + \mathbf{v}(t+\Delta t/2)\Delta t \tag{2.14}$$

The net forces are then computed from the newly updated particle positions and used for updating the particles' momenta in the second-half integration stage:

$$\mathbf{v}(t+\Delta t) = \mathbf{v}(t+\Delta t/2) + \frac{\mathbf{f}(t+\Delta t)\Delta t}{2m} \tag{2.15}$$

The accuracy of the velocity Verlet algorithm is in the order of $(\Delta t)^2$. The splitting into two stages in the velocity Verlet algorithm is consistent with the Trotter splitting scheme applied for the Liouville operator acting on any function of the particle positions and momenta, for example, the Hamiltonian. Since the Jacobian of the coordinate transformations 2.13, 2.14 and 2.15 is unity, the overall transformation preserves the phase space volume[57].

Rigid body constraints

In certain modeling applications, it is necessary to keep the relative positions or angles within a group of atoms fixed during the course of a simulation. In modeling molecular systems, when the irrelevant high-frequency motion between atoms is irrelevant to the dynamics of interest, the atoms are usually constrained so that they do not move relative to each other. For example, in the TIP3P water model the H-O bond length and H-O-H bond angle are held fixed at 0.095nm and 104.42 degrees, respectively, making the water model a V-shaped rigid body[65]. For soft matter systems, as described in the previous section, to capture the geometry of shape nanoparticles and colloidal molecules, the beads within a nanoparticle should be rigidly linked together.

There are two well-known methods to model rigid body constraints: SHAKE-based methods and rigid body dynamics methods. In the SHAKE-based methods, the fixed bond lengths and angles are achieved by applying constrained forces to a group of atoms (i.e. a cluster) under consideration[57]. The calculation of these forces is iterated until the bond lengths and angles are close to the set values within a given tolerance. Although the SHAKE algorithm has been extended to handle arbitrary shapes, for example, via angle and dihedral angle constraints[66–68], and to avoid the iterative scheme, the computational cost of these algorithms often becomes prohibitive for parallel simulation codes as the number of

constraints per cluster increases.

In the rigid body dynamics methods, the group of coarse-grained beads within a nanoparticle is treated as a rigid body of which the equations of motion are solved via classical rigid body dynamics given that the body forces and torques are calculated from the forces exerted on constituent beads[69, 70]. This non-iterative method is suitable for our model nanoparticles, which are typically composed of more than five beads, because its computational cost is less than SHAKE as the number of beads per rigid body increases. Moreover, the accuracy in the bond lengths and angles is only bounded by computer numerical precisions. We have implemented rigid body dynamics integrators for NVE, NVT and NPT ensembles in HOOMD-blue. The major difference of these integrators from those previously implemented in LAMMPS and other molecular dynamics codes is that the equations of rotational motion are Hamiltonian, for which the numerical integrators are sympletic, i.e. time reversible and phase space volume preserving. Further details on these integrators will be discussed in Chapter 3.

Simulation procedure

To ascertain that the resulted structures are not kinetically trapped states, we perform simulations from different initial states, i.e. the particles are initialized with randomly distributed positions and velocities. The system is equilibrated in athermal condition, i.e. all interactions are purely repulsive, and brought to the target density by decreasing the simulation box length. The initial athermal condition is crucial for the system not to be biased by any, however weak, attraction, and to be as similar as possible to a disordered state. The disordered system at the target density is subsequently cooled down by decreasing temperature step by step until the change in the structural morphology is negligible. At each temperature step, the system is equilibrated for a sufficiently long time period depending on the system size, density and temperature. To further ensure that the final structure is not pathway dependent, we vary the cooling schedule, couple cooling with annealing, or heat the system back to the original temperature and redo the cooling. The particle positions and velocities and thermal quantities are periodically written to text files, and analyzed by post-processing codes.

2.2.3 Simulation packages

We used three simulation codes in this thesis: our own code, LAMMPS[63] and HOOMD-blue[64]. The reasons to use different codes are because of (i) the available computing resources at the time and (ii) some functionalities available in only one package but not in

the others. We implemented several study-specific functionalities into both LAMMPS and HOOMD-blue that have never been introduced in any open-source codes.

Our own simulation code originally inherits from the in-house C/C++ code developed by Dr. Zhenli Zhang and Dr. Mark A. Horsch in the Glotzer group. We have modified and extended the code using the object-oriented programming approach. The functionalities of this simulation package include a user-friendly input interface, a flexible design template for building block geometry, a driver to internally launch LAMMPS on multiple processors and a set of standard analysis tools. Another branch of this code was developed for specific studies that involve particle polydispersity, spatially dependent interactions, dipole interactions and self-limiting aggregation. This parallel code can run on shared-memory clusters and has good scaling up to 4 processors. We also developed a graphical user interface software module for molecular visualization and computer-aided design purposes, VisualizerX (Appendix C).

LAMMPS (Large-scale Atomistic/Molecular Massively Parallel Simulator)[71], a well-known open-source C/C++ code is hosted by Dr. Steve Plimpton at the Sandia National Laboratory. This is a general purpose parallel molecular dynamics code designed to run on distributed memory clusters using message-passing interface (MPI) programming libraries. The object oriented programming approach allows developers to implement additional functionalities straightforwardly while taking full advantage of parallel computing. The parallelization in LAMMPS is based on spatial decomposition in the sense that the simulation box is divided into non-overlapping domains, in each of which the atoms are managed by an individual processor. The best parallel performance is achieved when (i) the data transferred between processors is minimized, (ii) the computational load is balanced between processors, and (iii) the particle data managed by a processor fits its cache memory. Further details on how spatial decomposition is implemented in LAMMPS are given in Reference [71].

HOOMD-blue (Highly Optimized Object-oriented Many-particle Dynamics- Blue Edition), a newly born open-source C/C++ code is hosted by Dr. Joshua A. Anderson in the Glotzer group[72]. This is a general purpose molecular dynamics code designed for NVIDIA®graphics processing units (GPUs). Over the past three years, HOOMD-blue has gained a rapidly growing interest because of its impressive speedup as compared to other simulation packages for certain classes of problems including soft matter systems. Developers can add functionalities to HOOMD-blue by implementing plugins fairly easily. HOOMD-blue maximizes the GPU computing capacities by performing neighbor list building, force calculation and time integration all on the GPU. The best performance can be achieved when (i) the data transfers between CPU RAM and GPU memory are minimized,

(ii) the locality of the memory access on the device is maximized, and (iii) the number of idle computing units is minimized. Further details on the optimized algorithms are implemented in HOOMD are given in Reference [72].

During the course of this study, we have implemented various functionalities to LAMMPS and HOOMD-blue including force field, constraints and data analysis. In particular, we implemented the rigid body integrators using the quaternion scheme for NVE, NVT and NPT simulations and the energy minimizer for rigid bodies into HOOMD-blue. Further details on these contributions will be discussed in the following chapter.

Chapter 3

Rigid body constraints in molecular dynamics on graphics processing units

Rigid body constraints are commonly used in a wide range of molecular modeling applications from the atomistic scale, modeling the bonds in molecules such as water, carbon dioxide, and benzene, to the colloidal scale, modeling nanorods, cubes, plates, tetrahedra and patchy nanoparticles. While there exist parallel implementations of rigid constraints for molecular dynamics simulations for distributed memory clusters, these implementations have poor performance scaling as the number of rigid bodies and/or the number of particles in each body increases. On shared memory systems, such as multi-core CPUs and many-core graphics processing units (GPUs), rigid body constraints can be parallelized so that significantly better performance is possible. We have designed a massively parallel rigid body constraint algorithm, and implemented it in HOOMD-blue, a GPU-accelerated, open-source, general purpose molecular dynamics simulation package. For typical simulations, the GPU implementation running on a single NVIDIA® GTX 480 card is twice as fast as LAMMPS running on 64 Intel® Xeon® E5540 cores connected via 20GB/sec Inifiniband. In the HOOMD-blue code package, rigid constraints can be used seamlessly with non-rigid parts of the system, (e.g. point particles, bonded particles and walls), and with many different integration methods, including NVE, NVT, NPT, and Brownian Dynamics. We have also incorporated the FIRE energy minimization algorithm, reformulated to be applicable to mixed systems of rigid bodies and non-rigid particles. To our knowledge, HOOMD-blue is the first MD code to allow energy minimization to be applied to systems with rigid body constraints.[1]

[1] This chapter is adapted from Reference [73] T. D. Nguyen, C. L. Phillips, J. A. Anderson, S. C. Glotzer, Rigid body constraints realized in massively parallel molecular dynamics simulations on graphics processing units, *submitted*.

3.1 Introduction

Rigid body constraints refer to techniques in molecular modeling to fix the relative positions or angles within a group of atoms during the course of a simulation. For molecular systems, when the irrelevant high-frequency motion between atoms is irrelevant to the dynamics of interest, the atoms are usually constrained so that they do not move relative to each other. For example, in the TIP3P water model the H-O bond length and H-O-H bond angle are held fixed at 0.095nm and 104.42 degrees, respectively, making the water model a V-shaped rigid body[65]. For polymer-tethered nanoparticle and colloid systems, the beads within the nanoparticle should be rigidly linked together to capture the geometry of shape nanoparticles and colloidal molecules[15, 17–21, 27, 38, 74–77].

There are two well-known methods to model rigid body constraints: SHAKE-based methods and rigid body dynamics methods. In the SHAKE-based methods, the fixed bond lengths and angles are achieved by applying constrained forces to the group of atoms or particles under consideration[56, 57]. The calculation of these forces is iterated until the bond lengths and angles are close to the set values within a given tolerance. Although the original SHAKE algorithm has been extended to handle arbitrary shapes, for example, via angle and dihedral angle constraints[68], and to avoid the iterative scheme, the computational cost of these algorithms often becomes prohibitive for parallel simulation codes as the number of constraints per cluster increases. On the other hand, in the rigid body dynamics methods, the group of coarse-grained beads within a nanoparticle is treated as a rigid body of which the equations of motion are solved via classical rigid body dynamics given that the body forces and torques are calculated from the forces exerting on constituent beads. The rotational degrees of freedom of a rigid body are represented by a quaternion to avoid the singularity of the Euler angle representation, and to reduce the computational cost, numerical error accumulation and data storage of the rotational matrix representation. These methods can be added to a MD package with minimal modifications by taking advantage of the existing code that computes particle-particle interactions. Rigid body dynamics are available in MD software packages such as DL_POLY and LAMMPS, and have been used to model cubes, rods, bent rods, jacks, plates, bumpy spheres, water molecules and ions, and buckyballs[17–21, 27, 38, 74, 75, 78–81].

One problem that arises for both rigid body and SHAKE constraints is that they often cannot be used with complementary methods that would violate the constraints, such as energy minimization. Local energy minimization methods find a local minimum of the potential energy landscape given an initial configuration, in effect, quenching the system. Such methods are used to relax initial configurations, find zero temperature equilibrium

configurations of crystalline solids, native configurations of biomolecules, and low energy atom clusters[82], and can be an important step in protein folding algorithms[83]. One minimization technique commonly employed for unconstrained particles is the conjugate gradient (CG) method[84]. Applying this method to a system of rigid bodies may be possible, however we are unaware of any existing adaptation and do not attempt to derive one. Instead, we find that a straightforward application of the Fast Inertial Relaxation Engine (FIRE)[82] algorithm works for both unconstrained particles and rigid bodies while using the basic framework of the rigid body NVE dynamics method.

3.2 GPU-accelerated molecular dynamics

3.2.1 Graphics processing units

Modern graphics processing units (GPUs) deliver tremendous computational performance at a fraction of the cost and power consumption of a cluster of traditional CPUs. On a single silicon chip with three billion transistors, current GPU models provide a theoretical peak of 1.3 teraflops of compute throughput and 177 gigabytes per second (GB/s) of memory bandwidth from off-chip, or global, device memory[85].

The GPU hardware is different from a CPU in many ways. First and foremost, while a CPU core executes a single instruction at a time, a GPU executes hundreds. The processor chip on the NVIDIA® GeForce® GTX 480 (GF100), for example, contains 480 individual cores. Each core is capable of processing one single precision floating point or integer operation per clock tick. The cores on the GTX 480 are grouped into 15 streaming multiprocessors (MPs), which perform instruction scheduling and are each capable of maintaining up to 1536 independent computation streams or threads in flight at any time slice. Thus the GPU is only fully occupied when more than 23 thousand threads are executing on the device.

When launched, threads are grouped into blocks. Each thread can locally access its index within the block, threadIdx, the index of its block, blockIdx, and a small (up to 48KB) pool of shared memory also available to the other threads in the same block. For global memory transactions, the GF100 includes a full cache hierarchy with up to 48KB of hardware managed L1 cache in each streaming multi-processor, 768KB of shared L2 cache, and up to 6GB of device memory.

The performance of functions executed on the GPU, or kernels, can be limited by either the memory bandwidth between the cores and device memory, or the rate at which arithmetic

instructions are retired. In most molecular dynamics applications, the bottleneck is the device memory bandwidth. Optimal performance is obtained in these cases by carefully minimizing the amount of memory accessed and by tuning the access pattern to maximize cache hits. While the device memory bandwidth is fast, for example, for GTX 480 cards, 384-bit / 8 (memory interface width in bytes) $\times$ 1.848GHz (memory clock) $\times$ 2 (double data rate) = 177.4GB/sec, data transfers between host memory (accessible by the CPU) and device memory are typically 2-6GB/sec, depending on the hardware configuration. Thus, in order to maximize overall application speed, transfer between the host and device must be avoided whenever possible.

3.2.2 Molecular dynamics on GPUs – HOOMD-blue

The Compute Unified Design Architecture (CUDA®) programming environment, which was the first to enable general purpose computing on massively parallel GPUs, was released in 2007. HOOMD-blue, available under an open-source code license[72], differs from most other GPU-accelerated MD methods in that it implements every step of the computation on the GPU and avoids all host/device transfers, except when needed for disk I/O[72]. By avoiding both serial code bottlenecks and slow memory transfer between the host and device, HOOMD-blue reaches maximum performance on a single GPU. The most recent release version 0.9.1 deployed on a single GTX 480 performs at a speed equivalent to LAMMPS run on 50-90 Intel® Xeon® E5540 CPU cores on an Infiniband-connected cluster.

HOOMD-blue implements the standard velocity Verlet algorithm employed by many classical MD frameworks[72]. In each time step, the state of a many-particle system is updated in a number of stages. First, the particles position and velocity are updated in the first half integration step using the forces from the previous time step (1). Second, the particles are binned into a cell list. From this cell list, a neighbor list is constructed for each particle that contains the indices of all the particles within the specified interaction range (2). The neighbor list is consulted when computing the pair forces between all interacting pairs of particles (3). Next, additional forces, e.g. bonds, constraints and thermostats, are accumulated into the particle force (4). Finally, the computed forces are used to update the particles in the second half integration step forward to a full time step (5). Each phase consists of one or more kernels that are executed on the GPU and all necessary data structures are stored in device memory. Different versions of each phase can be interchanged to implement numerous force fields and ensembles, thereby enabling diverse simulation possibilities in a single code package. The rigid body constraints are implemented into this framework at phases (1) and (5).

3.3 Algorithms

3.3.1 Rigid body dynamics

A system contains N particles where each may or may not belong to a rigid body, for a total of N_{bodies} rigid bodies. Consequently, each rigid body b is composed of N_b particles indexed by $C_b = [c_{b_1}; c_{b_2}; ..; c_{bN_b}]$. For example, C_2 = [5; 6;..; 16] gives the indices of the N_2 = 12 constituent particles of body number 2. The center of mass of body b is located in the space frame at position $\mathbf{x}_b$, moving at a velocity of $\mathbf{v}_b$. It has a mass M_b and inertia tensor $\mathbf{I}_b$. The orientational degrees of freedom include its angular momentum $\mathbf{L}_b$ and a unit quaternion $\mathbf{q}_b = [q_0, q_1, q_2, q_3]$ representing its orientation: $\mathbf{q}_b^T \mathbf{q}_b = 1$. In the body frame, a body's center of mass is at the origin and $\mathbf{I}_b$ is diagonal. Thus

$$\mathbf{x}_{bk} = \mathbf{x}_b + \mathbf{R}(\mathbf{q}_b)\mathbf{d}_{bk} \tag{3.1}$$

$$\mathbf{v}_{bk} = \mathbf{v}_b + \omega \times (\mathbf{R}(\mathbf{q}_b)\mathbf{d}_{bk}) \tag{3.2}$$

where $\mathbf{d}_{bk}$ is the displacement vector that defines the position of the particle with respect to the body frame (k = 1; 2;..; N_b), ω is the body angular velocity in the space frame, which is related to the angular momentum by: $\omega = \mathbf{R}(\mathbf{q}_b)(\mathbf{I}_b)^{-1}[\mathbf{R}(\mathbf{q}_b)]^T \mathbf{L}_b$; and $\mathbf{R}(\mathbf{q}_b)$ is the rotation matrix which converts a vector from the body frame to space frame:

$$\mathbf{R}(\mathbf{q}_b) = \begin{pmatrix} q_0^2+q_1^2-q_2^2-q_3^2 & 2(q_1q_2+q_0q_3) & 2(q_1q_3-q_0q_2) \\ 2(q_1q_2-q_0q_3) & q_0^2-q_1^2+q_2^2-q_3^2 & 2(q_2q_3+q_0q_1) \\ 2(q_1q_3+q_0q_2) & 2(q_2q_3-q_0q_1) & q_0^2-q_1^2-q_2^2+q_3^2 \end{pmatrix} \tag{3.3}$$

The net force and torque acting on body b in the space frame are the sums of the forces and torques resulting from the particle-particle forces exerting on its constituent particles:

$$\mathbf{f}_b = \sum_{k=1}^{N_b} \mathbf{f}_k \tag{3.4}$$

$$\mathbf{t}_b = \sum_{k=1}^{N_b} (\mathbf{R}^T \mathbf{d}_{bk}) \times \mathbf{f}_k \tag{3.5}$$

The Newtonian equations of motion of the body b are given by classical mechanics:

$$\dot{\mathbf{x}}_{cm} = \mathbf{v}_{cm} \tag{3.6}$$

$$\dot{\mathbf{v}}_{cm} = \mathbf{F}/m \tag{3.7}$$

$$\dot{\mathbf{L}} = \mathbf{T} \tag{3.8}$$

$$\dot{\mathbf{q}} = \frac{1}{2}\mathbf{A}(\omega)\mathbf{q} \tag{3.9}$$

where the 4-by-4 matrix $\mathbf{A}(\omega_b)$ is defined in Reference [56]. By integrating these equations of motion, we obtain the trajectory of the body b with the total energy conserved. Given the existing velocity Verlet integrator used for non-rigid particles, it is natural to use the same integrator for rigid bodies. Note that the quaternion equation 3.9 should be solved iteratively in the first integration stage.

The first-half integration stage consists of the following step:

$$\mathbf{v}_b(t+\Delta t/2) = \mathbf{v}_b(t) + \frac{\mathbf{f}_b(t)\Delta t}{2m} \tag{3.10}$$

$$\mathbf{x}_b(t+\Delta t) = \mathbf{x}_b(t) + \mathbf{v}_b(t+\Delta t/2)\Delta t \tag{3.11}$$

$$\mathbf{L}_b(t+\Delta t/2) = \mathbf{L}_b(t) + \frac{\mathbf{t}_b(t)\Delta t}{2} \tag{3.12}$$

$$\mathbf{q}_b(t+\Delta t/2) = Q(\mathbf{q}_b(t), \Delta t, \mathbf{L}_b(t+\Delta t/2), \mathbf{I}_b) \tag{3.13}$$

where $Q(.)$ is the iterative solver based on the Richardson method. The position and velocity of constituent particles are calculated from Equations (3.1, 3.2). The body forces $\mathbf{f}_b(t+\Delta t)$ and torques $\mathbf{t}_b(t+\Delta t)$ at the next step are then calculated before proceeding with the second-half integration stage:

$$\mathbf{v}_b(t+\Delta t) = \mathbf{v}_b(t) + \frac{\mathbf{f}_b(t+\Delta t)\Delta t}{2m} \tag{3.14}$$

$$\mathbf{L}_b(t+\Delta t) = \mathbf{L}_b(t) + \frac{\mathbf{t}_b(t+\Delta t)\Delta t}{2} \tag{3.15}$$

The equations (3.10, 3.11, 3.12, 3.13, 3.14, 3.15) have been implemented in LAMMPS and HOOMD-blue. To avoid the iterative method when solving the quaternion equation, an alternative is to employ the quaternion scheme proposed by Miller et al.[70] The idea is to propose a Hamiltonian of the rotational degrees of freedom $H_{rot}(\mathbf{q}, \mathbf{p}_q)$ from which the rotational equations of motion for quaternion and its conjugate momentum can be derived.

The quaternion scheme is shown to be conceptually advantageous over the iterative scheme. First, despite its energy conservation, the iterative scheme does not have a direct connection to statistical mechanics. On the other hand, the quaternion scheme due

to its Hamiltonian nature samples the microcanonical ensemble (NVE). Second, the velocity Verlet integrator when applied for this scheme is time reversible and phase space volume preserving, allowing for a better stability in a long-term simulation. Finally, it is straightforward to simulate rigid bodies in other thermodynamic ensembles, e.g. NVT and NPT, by deriving the extended Hamiltonian in a similar manner to non-rigid particles. We have implemented the integrators for rigid bodies for NVE, NVT and NPT ensembles in HOOMD-blue according to the algorithms discussed in the work of Kamberaj et al.[86] We should note that while both the NVT quaternion scheme and traditional Langevin thermostat yield the canonical ensemble, the former is a better choice when (i) simulating rigid bodies consisting of a large number of particles as the random forces in BD are likely canceled out, hindering the diffusion of individual bodies, or (ii) transport properties are of interest because hydrodynamic interactions are not included in BD. Additionally, thermostats are attached to both translational and rotational degrees of freedom in the NVT integrator, which is not the case for the traditional Langevin thermostat.

3.3.2 Energy minimization

The FIRE algorithm[82] works in conjunction with any MD integrator to compute a trajectory to a local energy minimum. At each iteration step, the integrator is used to advance the positions and velocities for all the particles in the system, given the computed forces. FIRE modifies velocities and the step size by the following prescription. As long as the particles in the system are moving in directions that lower the energy of the system as a whole, and have been for a sufficient number of steps, particle velocities and the step size are increased, subject to limits. As soon as the particles are no longer moving so as to lower the energy of the whole system, all particles are brought to a halt, the step size is decreased, and new velocities are generated in the direction of the force on each particle. Convergence to a minimum energy is attained when the root mean square force and change in the energy of the system are below set tolerances. In reference[82], FIRE is demonstrated to be effective and surprisingly fast compared to competing schemes, even for systems with millions of degrees of freedom.

3.4 Implementation

Augmenting HOOMD-blue to include rigid body constraints is accomplished in two parts. First, the following data structures are added to hold the dynamic, static and computed

properties for each body: $\mathbf{x}_b$, $\mathbf{v}_b$, $\mathbf{L}_b$, M_b, $\mathbf{I}_b$, N_b, $\mathbf{C}_b$, $\mathbf{d}_{bk}$, $\mathbf{f}_b$ and $\mathbf{t}_b$. Each quantity with a single subscript is stored in a simple array. Those with two subscripts are stored in padded matrices where the second index is the fastest varying index. Second, new routines are written that integrate the equations of motion of the rigid bodies in the system, with separate versions for the NVE, NVT, and NPT ensembles.

To attain maximal performance, all data structures are stored in device memory and all integration steps are carried out on the GPU. No communication is required between the host and the device to advance the system. Although padded matrices waste some memory in systems where different bodies contain different numbers of particles, they enable contiguous memory accesses in the integration kernels.

3.4.1 Molecular dynamics

In HOOMD-blue, the integration of Newton's equations of motion for rigid bodies, Equations, is distributed over five kernels. The first two kernels update the state of the body and its constituent particles. Next, one kernel sums the force and torque on each body from the forces applied to its particles. Finally, two kernels apply the second half of the update to the state of the body and its particles. Pseudocode describing the basic structure of these kernels is provided in Algorithm 1 and Algorithm 2. Within the pseudocode, device memory reads/writes are indicated by a double arrow, and local memory writes by a single arrow. The performance of each of these kernels is bound by device memory bandwidth. Memory accesses are ordered to be contiguous so as to best utilize the cache hierarchy on GF100 and maximize their performance.

The first kernel, detailed in Algorithm 1, updates the state of the rigid body at the beginning of the time step. Each thread loads state data for its assigned body from global memory, updates the position, orientation, velocity, and angular momentum following Equations (3.10, 3.11, 3.12, 3.13), and writes the updated state back to global memory. All memory transactions made by Algorithm 1 are contiguous. The second kernel, detailed in Algorithm 2, sets the constrained position and velocity of each particle that belongs to a rigid body. One block of threads is assigned to each body. At the beginning of the kernel, one thread loads the state of the rigid body into shared memory and a barrier synchronization is performed. Then, all threads participate in computing $\mathbf{x}_i$ and $\mathbf{v}_i$. Each thread computes these quantities for several particles i, where $i = c_{bk}$ and $k = \text{threadIdx} + w \cdot \text{blockDim}$, in a loop over $w = 0; 1; 2; 3; ..$ This sliding window construction handles bodies of arbitrary size with a single fixed block size. The matrices $\mathbf{C}_b$ and $\mathbf{d}_{bk}$ are stored with k as their fast index so that the reads on lines 15 and 16 of Algorithm 2 by neighboring threads are contiguous in

Algorithm 1 Update bodies in the first-half step

Require: $\lceil N_{bodies}/\text{blockDim} \rceil$ blocks run on the device

1: $b \leftarrow \text{blockIdx} \cdot \text{blockDim} + \text{threadIdx}$
2: **if** $b < N_{bodies}$ **then**
3: $M \Leftarrow M_b$
4: $\mathbf{I} \Leftarrow \mathbf{I}_b$
5: $\mathbf{x} \Leftarrow \mathbf{x}_b$
6: $\mathbf{v} \Leftarrow \mathbf{v}_b$
7: $\mathbf{f} \Leftarrow \mathbf{f}_b$
8: $\mathbf{t} \Leftarrow \mathbf{t}_b$
9: $\mathbf{L} \Leftarrow \mathbf{x}_b$
10: $\mathbf{q} \Leftarrow \mathbf{q}_b$
11: $\mathbf{v} \leftarrow \mathbf{v} + \mathbf{f} \cdot dt/(2M)$
12: $\mathbf{x} \leftarrow \mathbf{x} + \mathbf{v} \cdot dt$
13: $\mathbf{L} \leftarrow \mathbf{L} + \mathbf{t} \cdot dt/2$
14: $\mathbf{q} \leftarrow Q(\mathbf{q}, \mathbf{L}, \mathbf{I}, dt)$
15: $\omega \Leftarrow (\mathbf{R}(\mathbf{q})\mathbf{I}[\mathbf{R}(\mathbf{q})]^{-1})\mathbf{L}$
16: $\mathbf{x} \Rightarrow \mathbf{x}_b$
17: $\mathbf{v} \Rightarrow \mathbf{v}_b$
18: $\mathbf{L} \Rightarrow \mathbf{L}_b$
19: $\mathbf{q} \Rightarrow \mathbf{q}_b$
20: $\omega \Rightarrow \omega_b$
21: **end if**

memory. The writes on lines 19 and 20 may or may not be contiguous, depending on the order in which particle indices are stored in $\mathbf{C}_b$. To avoid this potential performance hit, all particles in body b are grouped together and listed in order in $\mathbf{C}_b$. Next, particle-particle forces are computed via the standard MD force calculation kernels. Then the net force $\mathbf{f}_b$ and torque $\mathbf{t}_b$ on each body are calculated in the third kernel (Algorithm 3). As in Algorithm 2, one block of threads is assigned to each body. Each thread k loads c_{bk}, $\mathbf{d}_{bk}$, and the particle force $\mathbf{f}_k$ from global memory and the net force and torque are summed using a standard parallel reduction performed in shared memory. The resultant $\mathbf{f}_b$ and $\mathbf{t}_b$ are then written out to global memory. In the fourth kernel, the velocity and angular momentum of each rigid body are updated again via Equations 3.14 and 3.15. One thread is assigned to each rigid body in a manner analogous to Algorithm 1. Finally, in the fifth kernel, each body's particles are set to their updated constrained velocity. One block of threads is assigned per body. The kernel is nearly identical to Algorithm 2, except that only the particle velocity is calculated and written to global memory.

All particles that are not part of a rigid body are updated to the next step by the existing standard MD integration kernels. The contribution from rigid body constraints to the net

Algorithm 2 Update particles in the first-half step

Require: $\lceil N_{bodies} \rceil$ blocks run on the device
1: $b \leftarrow$ blockIdx
2: **if** $b < N_{bodies}$ **then**
3: $n \Leftarrow N_b$
4: $\mathbf{I} \Leftarrow \mathbf{I}_b$
5: $\mathbf{x} \Leftarrow \mathbf{x}_b$
6: $\mathbf{v} \Leftarrow \mathbf{v}_b$
7: $\mathbf{L} \Leftarrow \mathbf{L}_b$
8: $\mathbf{q} \Leftarrow \mathbf{q}_b$
9: $\omega \Leftarrow \omega_b$
10: **end if**
11: syncthreads()
12: **for** $w = 0$ to n/blockDim **do**
13: $k \leftarrow w \cdot \text{blockDim} + \text{threadIdx}$
14: **if** $k < n$ **then**
15: $i \Rightarrow c_{bk}$
16: $\mathbf{d} \Rightarrow \mathbf{d}_{bk}$
17: $\mathbf{v} \leftarrow \mathbf{v} + \omega \times (\mathbf{R}(\mathbf{q}) \cdot \mathbf{d}_{bk})$
18: $\mathbf{x} \leftarrow \mathbf{x} + (\mathbf{R}(\mathbf{q}) \cdot \mathbf{d}_{bk})$
19: $\mathbf{v} \Rightarrow \mathbf{v}_i$
20: $\mathbf{x} \Rightarrow \mathbf{x}_i$
21: **end if**
22: **end for**

virial is also calculated in the particle kernel (Algorithm 2)[87], however, we exclude that code segment here for simplicity.

For NVT and NPT integrators, the body update kernels in two stages (Algorithm 1) are modified with the update of the quaternion and its conjugate momentum as given by Reference [86]. The particle update kernels (Algorithm 2) remain unchanged. For the BD integrator, a separate force kernel is invoked before the body forces and torques are computed, accumulating the random and drag forces to the constituent particles in rigid bodies.

3.4.2 Energy minimization

We extend FIRE to a system containing rigid bodies by adding the orientation of the rigid bodies to the degrees of freedom and use the rigid body NVE integrator to advance the positions, velocities, orientations, and angular velocities of the bodies. Both the center of mass velocities and the angular velocities of all the bodies are reset to zero if the energy

Algorithm 3 Compute body forces and toques

Require: $\lceil N_{bodies}/numBodiesperBlock \rceil$ blocks run on the device
Require: **sf**[blockSize] and **st**[blockSize]
1: $numThreadsperBody \leftarrow$ blockDim/threadIdx
2: $m \leftarrow$ threadIdx$/numThreadsperBody$
3: **if** threadIdx$\%numThreadsperBody == 0$ **then**
4: $b \leftarrow$ blockIdx $\cdot\, numBodiesperBlock + m$
5: **if** $b < N_{bodies}$ **then**
6: $idxBody[m] \leftarrow bodyIndices[b]$
7: $\mathbf{q}[m] \Leftarrow \mathbf{q}_b$
8: **else**
9: $idxBody[m] \leftarrow -1$
10: **end if**
11: **end if**
12: syncthreads()
13: $nWindows = \lceil nmax/windowSize \rceil + 1$
14: $\mathbf{pf} = 0$
15: **for** $w = 0$ to $nWindows$ **do**
16: $k \leftarrow w \cdot windowSize +$ threadIdx$\%windowSize$
17: **if** $k < nmax$ **then**
18: $pidx \leftarrow c(idxBody[m], k) = idxBody[m] \cdot nmax + k$
19: $\mathbf{pf} \leftarrow \mathbf{pf} + \mathbf{f}[pidx]$
20: **end if**
21: **end for**
22: syncthreads()
23: **sf**[threadIdx] $\leftarrow$ **pf**
24: $offset \leftarrow \min(windowSize, nmax)/2$
25: **while** $offset > 0$ **do**
26: **sf**[threadIdx] $\leftarrow$ **sf**[threadIdx] + **sf**[threadIdx $+ offset$]
27: **end while**
28: **if** threadIdx mod $numThreadsperBody == 0$ **then**
29: $\mathbf{f}_b \leftarrow$ **sf**[threadIdx]
30: **end if**

of the system stops decreasing. Convergence is reached when the root mean square force, root mean square torque, and change in the energy of the system are below set tolerances. Reference [82] points out that all degrees of freedom must be comparable for the algorithm to work. In practice, we find that the orientation is a sufficiently comparable degree of freedom and that it does not require special handling.

3.5 Validation and performance

3.5.1 Molecular dynamics

The rigid body constraint algorithm is well established in serial and parallel CPU codes and is mathematically no different when implemented on the GPU. However, to verify the correct function of our code, various quantities are checked for validity including energy and momentum conservation in the NVE ensemble, as well as temperature and pressure stability and the correct distribution of energy over the degrees of freedom in the NVT and NPT ensembles. Numerous rigid body systems are also simulated side-by-side on both the CPU and GPU to compare the results and evaluate their relative performance. The performance scaling of the GPU-accelerated algorithm is tested with simulations of a system of "patchy particles" studied by Zhang et al.[27]. These supraparticles shall be subsequently referred to as "patchy nanospheres" to avoid confusion. Each patchy nanosphere is a rigid body composed of 90 particles distributed on the surface of a sphere. Two attractive patches, each constructed from two linear arrangements of particles that interact with Lennard-Jones pair potentials, are placed at an angle $\theta = 2\pi/5$ with respect to the center of the body. Such patchy particles self- assembles into rings containing six patchy nanospheres[27]. The chosen benchmark systems consist of 225, 667, and 2000 patchy nanospheres resulting in 20250, 60030, and 180000 individual particles, respectively. Each system was annealed to an equilibrium structure at $k_BT/\varepsilon = 1.0$.

Figure 3.1 shows the system of 225 patchy nanospheres. Each simulation is executed using both the LAMMPS and HOOMD-blue code packages. LAMMPS simulations are deployed in parallel over 1, 2, 4, 8, 16, 32, 64, and 128 cores on the Nyx cluster at the University of Michigan. The nodes used are HP ProLiant DL1000 models with Intel® Xeon® E5540 15 processors operating at 2.53 GHz and connected via 20GB/s Infiniband. All nodes have identical software configurations, running an x86 64 install of RHEL 5.5, CUDA 3.0, and NVIDIA® drivers 195.36.24. The HOOMD-blue simulations were performed on a custom built workstation with a single NVIDIA® GTX 480. It also contains an AMD® Athlon™ II X4 630 processor operating at 2.8 GHz and runs CentOS 5.5, CUDA 3.0, and NVIDIA® drivers 260.19.21.

Performance results are measured by the number time steps that are executed per second and are shown in Figure 3.2 . For the 20K and 60K particle systems, LAMMPS achieves peak performance at 32 and 64 cores, respectively. For the 180K particle system LAMMPS no longer scales well at 128 cores; the performance is only 11% faster than it is at 64 cores. The reason for the poor scaling is the inter-node communication of the rigid body data

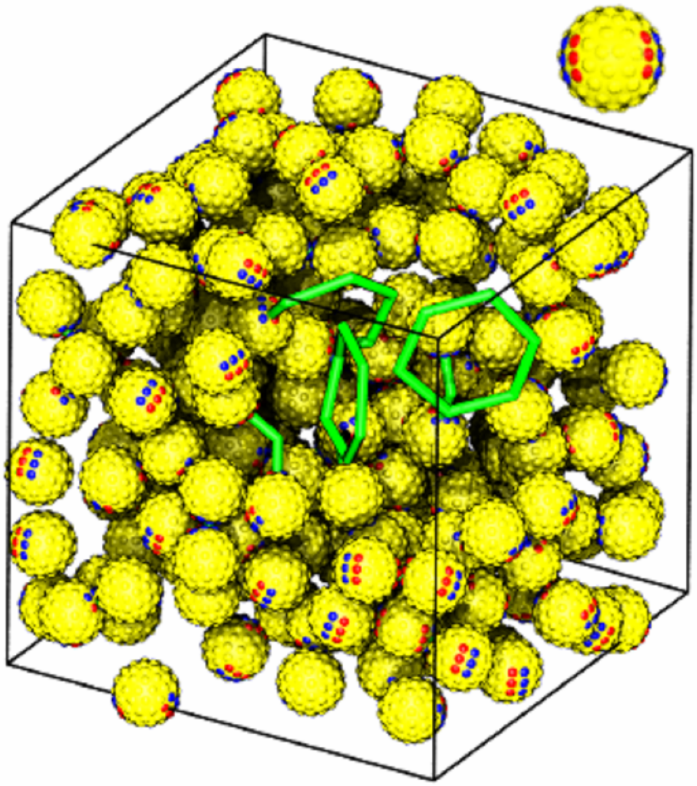

Figure 3.1 A system of 225 patchy nanospheres, each composed of 90 particles. The red and blue particles are attractive patches on the surface of the body. A single patchy nanosphere is shown in the upper right for reference. The nanospheres have been made invisible in the front-most.octant so that the ring structure formed by the invisible nanospheres can be shown in green. All system snapshots in this section are composed in VMD and raytraced with Tachyon unless stated otherwise.

structures during the time step. LAMMPS uses spatial decomposition to parallelize a MD simulation over many cores. In simulations of rigid bodies on a CPU cluster, the particles of a given body can be distributed over an arbitrary number of cores. The force and torque summation is performed by an all-reduce operation that returns results from all nodes to each node. In comparison, the GPU-accelerated implementation is deployed on a single GPU and requires no inter-node or even host-device communication. The equivalent operation to the all-reduce operation is performed within a block on a single streaming multi-processor. Consequently, HOOMD-blue attains a level of performance for rigid body simulations that cannot be reached with a parallel CPU-only code. For these patchy nanosphere benchmarks in particular, over a wide range of system sizes HOOMD-blue is 2.5-3.6 times faster than LAMMPS at its peak performance for any number of cores.

We also tested systems that mix rigid bodies and unconstrained particles. One example, shown in Figure 3.3 , is a system of polymer-tethered nanorods originally studied in

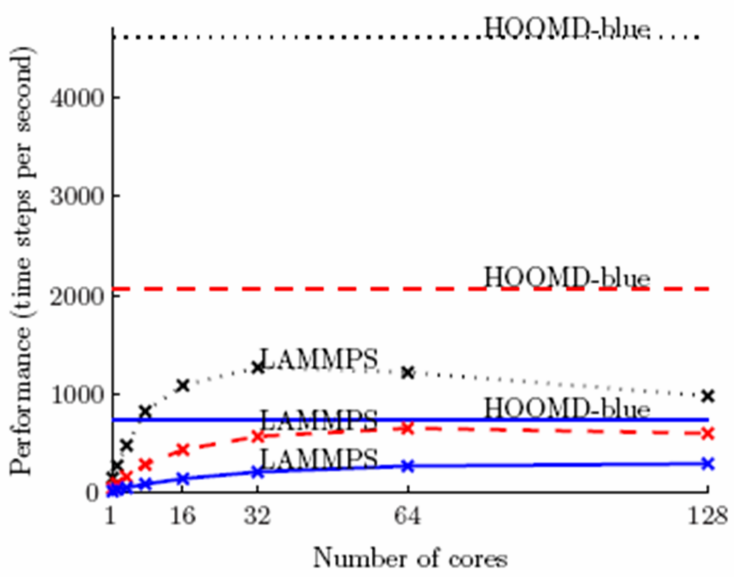

Figure 3.2 Performance in time steps per second obtained while running a simulation of 225 (dotted lines), 667 (dashed lines), and 2000 (solid lines) rigid bodies consisting of 20250, 60030, and 180000 particles respectively. LAMMPS performance on 1, 2, 4, 8, 16, 32, 64, and 128 CPU cores is compared to HOOMD-blue performance on a single NVIDIA®GTX 480 (indicated by the horizontal lines).

Reference [77] using LAMMPS. In this simulation, each tethered rod is composed of a five particle rigid rod and a nine particle flexible tether. One thousand tethered rods, for a total of 14000 particles, are placed in a box with packing fraction of 0.22. Rod particles are attracted to each other via a shifted Lennard-Jones pair potential with an interaction cutoff of 2.5 distance units. All other particle interactions are WCA volume excluding. The system is in an NVT ensemble with a kinetic temperature of $k_BT/\varepsilon = 1.4$. At these parameters the tethered nanorods self assemble into lamellar bilayers[77]. Simulations are executed with HOOMD-blue on three modern NVIDIA® GPUs, a GTX 480, a Tesla™S1070, and a Tesla™ S2050. The Tesla S1070 and S2050 are installed in the Nyx cluster environment where they are hosted by IBM System x3455 nodes each with two AMD® Opteron™ 2356 processors operating at 2.3 GHz. The LAMMPS simulations were deployed over 1, 8, 32, 64, and 128 cores of the Nyx cluster in the same configuration used for the patchy nanosphere runs. The results of this side-to-side comparison are shown in Figure 3.4 . HOOMD-blue running on a GTX 480 executes the tethered nanorod simulation at 1791 time steps per second, which is 2.5 times faster than LAMMPS running at peak performance in parallel on 64 CPU cores.

We also validate the NPT integrator by mapping the equation of state for soft tetrahedra. Each tetrahedron consists of 35 particles with 5 touching particles on each edge.

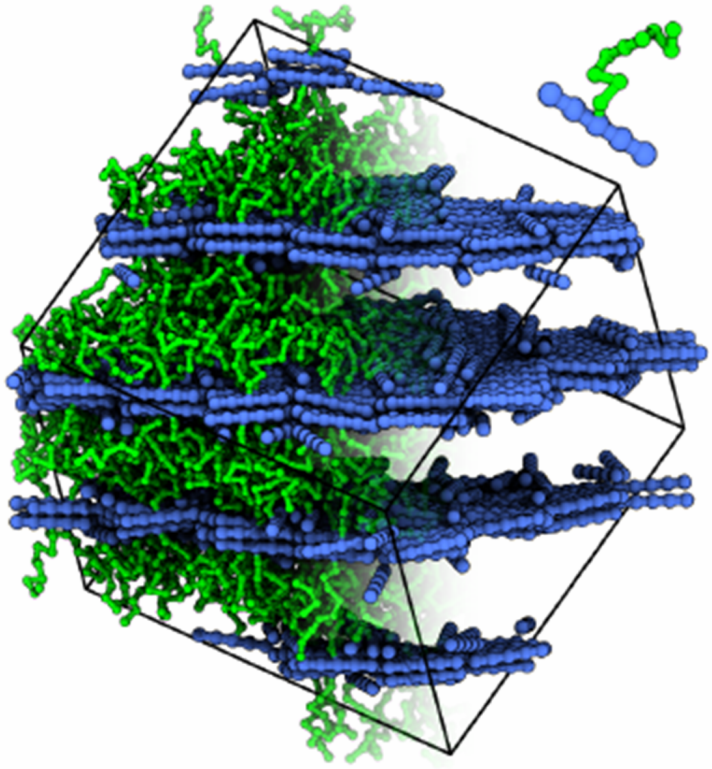

Figure 3.3 A system of one thousand tethered nanorods that have self-assembled into a lamellar bilayer. The upper right inset depicts a single tethered nanorod for reference. Each tethered nanorod is modeled by five particles rigidly connected in a line, attached to a flexible tether of nine particles. Bonds, both rigidly constrained and unconstrained, are shown as cylinders. Tethers have been removed from view in the right half of the image.

The particles interact with each other via the purely repulsive Weeks-Chandler-Andersen potential. Figure 3.5 shows the equation of state obtained from simulations of $N_P = 328$ tetrahedra. The system undergoes a first-order phase transition from a liquid state to a crystalline state. The transition occurs at $P^* = 55 - 60$, consistent with the results obtained by Haji-Abkari et al. with hard tetrahedra[88]. In the crystalline state, the tetrahedra form a 12-fold quasi-crystalline structure.

3.5.2 Energy minimization

Figure 3.6 demonstrates FIRE applied to an arrangement of rods and free particles. The rods are rigid bodies composed of five particles placed on a line. Rod particles interact with other rod particles by the attractive Lennard-Jones (LJ) potential. Free particles interact by the attractive LJ potential as well. However, rod particles and free particles interact by

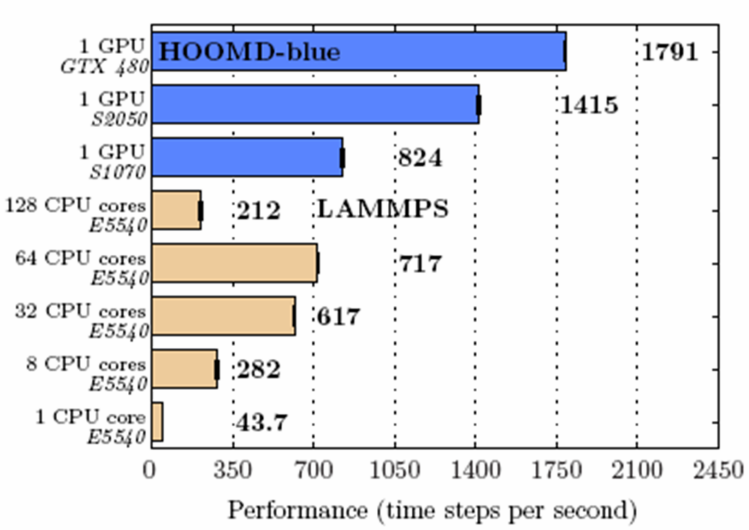

Figure 3.4 Performance in time steps per second obtained for a simulation of one thousand tethered nanorods (14000 total particles) on various hardware configurations. Each benchmark is performed 50 times. Bars are plotted at the median value and error bars display one standard deviation of variability.

a WCA volume excluding potential. An energy minimization is performed with a force tolerance of 10^{-4}, a torque tolerance of 0.1, and a change in energy tolerance of 10^{-12}. The FIRE energy minimization causes the rods to collapse into a hexagonally packed bundle and the free particles to collect into a droplet outside of the rod bundle after 60684 iterations. Only the first five percent of the time steps are spent collapsing the rod bundle. The rest are needed to collect the dispersed LJ droplets into a single droplet.

3.6 Conclusion

We discussed how a rigid body constraint algorithm is incorporated into HOOMD-blue, a massively parallel GPU-accelerated MD application. All data structures are stored on the GPU in order to attain the highest level of performance possible by avoiding costly transfers between the host and device. The performance of the kernels implementing the rigid body integration steps is limited only by the device memory bandwidth. This is achieved by carefully avoiding unnecessary device memory accesses and arranging the access patterns so as to make optimal use of the cache hierarchy on the GF100. Methods for simulating NVE, NVT, and NPT ensembles of rigid bodies are implemented in HOOMD-blue version 0.10.0, which is available free and open source. While two orders of magnitude increases in computational speed over a single CPU core have already been documented for this code

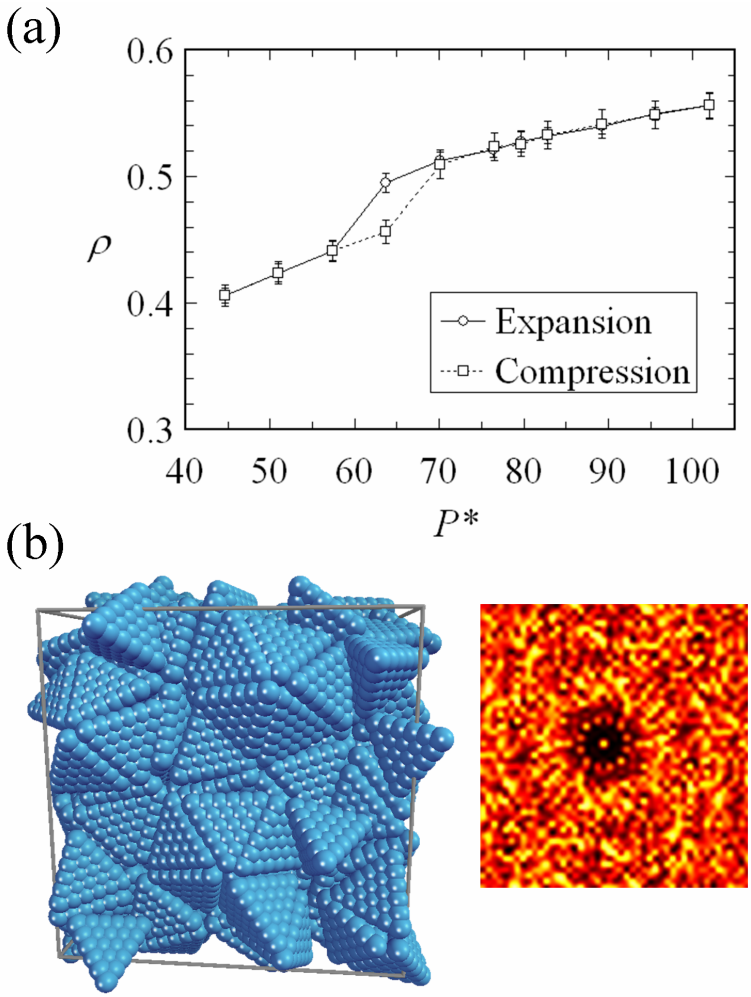

Figure 3.5 (a) Equation of state for tetrahedra interacting with the WCA potential. The reduced pressure $P^* = PL^3/\varepsilon$ where L is the effective edge length of each tetrahedron, ε is the energy scale of the Weeks-Chandler-Andersen potential. (b) Snapshot of the system at the crystalline state (left) and the diffraction pattern (right) showing peaks indicative of a 12-fold symmetry.

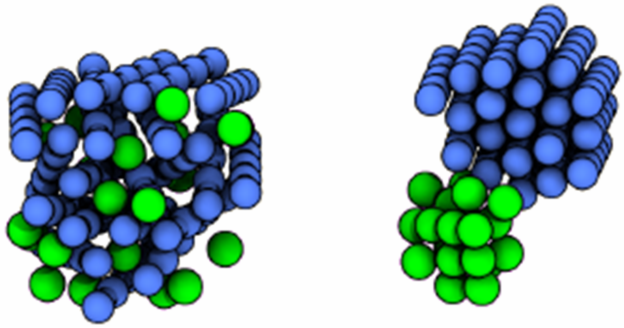

Figure 3.6 Left: Initial configuration of randomly placed rods (blue) intermixed with free particles (green). Rods are attracted to rods and free particles are attracted to free particles. Right: Final configuration after the FIRE energy minimization converges.

package running basic MD simulations[72], the GPU is especially well-suited for rigid body constraints. Two case studies are presented in this paper where HOOMD-blue consistently executes 2.5-3.6 times faster than the peak performance of the LAMMPS code package parallelized over any number of cores. We introduced a modest adaptation to the FIRE energy minimization algorithm that makes it suitable for use with rigid bodies. To our knowledge, HOOMD-blue is the first MD code to allow energy minimization to be applied to systems with rigid body constraints. With GPU acceleration, MD simulations of systems of rigid bodies can now be carried out on larger systems and for longer time scales on a single workstation than was previously possible even on large clusters. This advance will allow simulations of diverse systems, from molecules to nanoparticles, and explorations of previously inaccessible phase spaces.

Chapter 4
Equilibrium self-assembly

In this chapter, we investigate the self-assembly of two types of soft matter building blocks, tethered V-shaped nanoparticles and metallic/semiconductor nanoparticles. The former is a shape amphiphile similar to previously studied building blocks such as tethered nanospheres, tethered nanorods and tethered nanocubes but with a bent-shaped head group reminiscent of liquid crystalline bent-core molecules. The latter represents a broad family of recently synthesized particles that exhibit many unique interesting photonic and electronic properties. Despite the fact that their self-assembly in equilibrium is primarily governed by thermodynamics, these building blocks exhibit distinct assembly behaviors due to the uniqueness in their geometry and interaction, giving rise to fascinating assembled structures.

4.1 Self-assembly of tethered V-shaped nanoparticles

We use Brownian dynamics to investigate the self-assembly of single endfd-tethered, laterally- tethered and double end-tethered V-shaped nanoparticles. The simulation results are compared with model bent-core molecules without tethers and polymer-tethered nanorods to elucidate the combined effects of V-shaped geometry and the immiscibility between the V-shaped nanoparticles and the tethers on the self-assembled structures. We show that the V-shaped geometry significantly alters the phase diagram of tethered nanoparticles, and further, the immiscibility between particles and tethers leads to structures not previously predicted for bent-core molecules. Examples of mesophases predicted include honeycomb, hexagonally packed cylinders and perforated smectic phases.[1]

[1]This section is adapted from Reference [38] T. D. Nguyen, Z. Zhang, S. C. Glotzer, Molecular simulation study of self-assembly of tethered V-shaped nanoparticles, *Journal of Chemical Physics* 129, 244903-11, 2008.

4.1.1 Introduction

Polymer-functionalized nanoparticles have been proposed as promising building blocks for the bottom-up fabrication of nanostructures[15]. Recent experimental studies suggest that precise control over positioning polymeric chains onto the surfaces of nanoparticles will become viable in the near future. For example, Pan and co-workers[6] synthesized tethered gold nanorods and nanospheres by nucleotide hybridization. DeVries et al.[4] tailored the surface of spherical metal nanoparticles with self-assembled surfactants, inducing active poles to which they attached 11-mercaptoundecanoic acid (MUA). Nie et al.[5] synthesized CTAB-coated Au nanorods with thiol-terminated polystyrene chains of molecular weight $M_n = 12000$ attached at two ends. Simulations predict that the thermodynamic immiscibility between nanoparticles and their polymeric tethers will produce a collection of ordered structures, similar to those occurring due to microphase separation in block copolymers and surfactants[15–21, 33, 34]. However, in contrast with block copolymers and surfactants which consist of only flexible components, the local packing of hard nanoparticle "blocks" or "headgroups" gives rise to additional orientational ordering within the self-assembled meso-structures. While theoretical progress has been less developed due to the complicated entropic interactions between such asymmetric building blocks[89–93], computer simulations provide a potential means to tackle the problem. Using mesoscale simulations, Zhang et al.[15] showed the distinct local packing configurations that could be formed from tethered rods, disks, triangles and hexagons in complex 3D morphologies. Horsch and co-workers[17, 19] predicted that end-tethered nanorods can form chiral, twisted hexagonally packed cylinders which are the consequence of the competition between energetic and entropic effects. They further predicted that laterally-tethered nanorods would form novel bilayer sheet-like structures at high packing fraction[18]. It is therefore suggestive that geometrical anisotropy, in terms of aspect ratio and asymmetry, is an important factor that substantially affects the phase behavior of tethered nanoparticles[19, 34].

It has been argued that nanoparticle systems may form self-assembled structures that mimic those found in molecular liquid crystals[25, 33]. Molecular liquid crystals exhibit many exquisitely ordered phases that arise from packing considerations. One such molecule that has received particular attention because it is achiral, yet forms chiral phases, has a rigid V-shape unit; it is also known as a "banana" or bent-core molecule. In 1996, Niori[94] was the first to experimentally demonstrate that these molecules form various unprecedented liquid crystalline (LC) phases. Columnar rectangular ribbons (B1)[95–99], chiral tilted smectic (B2)[99–104], twist grain boundary (B4)[101, 105–107] and polar splaying, undulated layers (B7)[96, 103, 108] are popularly reported mesophases formed by these molecules. Depending on the chemical nature of the molecules as well as their bending

angle and terminal chain length, different temperature-dependent phase transitions have been observed. Owing to its unique geometry, bent-core molecules exhibit spontaneous chiral structures and switchable polar ordering that are not inherent to linear molecules. Of particular interest is the spontaneous development of superstructural chirality which can be employed in a variety of optical and electronic applications including photonic band gap materials[109] and, more recently, negative refractive index materials[110–114].

Molecular chirality and long-range polar interactions are proposed theoretically[90, 92], computationally[115–119] and experimentally[101, 113] to be two major factors leading to the spontaneous formation of chiral structure and helical morphologies in the "B" phases of bent-core molecules. At mesoscopic length scales, however, these two ingredients are not easily experimentally reproduced. Alternatively, Xu and Selinger[120] proposed that steric interactions might be sufficient for chiral desymmetrisation and that neither molecular chirality nor dipole-dipole interactions are necessary. In their Monte Carlo simulations, coarse-grained V-shaped molecules with soft repulsive interactions indeed exhibit a chiral smectic phase with a random inter-layer polar distribution. Johnston et al.[116] demonstrated that bent-core molecules interacting via a Gay-Berne potential, which is essentially a directional Lennard-Jones potential, assemble into a twist grain boundary phase. The simulated super-helical structure is in good agreement with previous experimental work in the literature. Dewar et al.[121] reported a tilted smectic-B phase with a coarse-grained bead-chain model and a Lennard-Jones pair-wise interaction. They argued that this "bumpy" model is physically relevant due to the fact that the bent-core units are normally made up of several aryl groups. Actual bent-core molecules, however, are synthesized with flexible terminal chains; these parts of the molecule have been often excluded in previous theoretical or computational work. Recently, Dewar and Camp[122] studied systems of bent-core molecules with two short flexible tails, one at each end. They demonstrated that, as compared to previous rigid models, the flexible model led to enhanced fluctuations in the smectic-layer structures, which is in better correspondence with those in actual smectic liquid crystals. However, in their configurational-bias Monte Carlo simulations, they ignored steric interactions between tails on different molecules. The prior simulation studies of tethered nanoparticles described earlier suggest that these flexible segments may play an important role in the self-assembly of these molecules.

In this study, we investigate the self-assembly of polymer-tethered V-shaped nanoparticles. The simulation results are compared with both the model bent-core molecules without tethers and polymer-tethered nanorods, a limit of tethered V-shaped nanoparticles in which the opening angle is 180 degrees. Our study thereby elucidates the combined effects of V-shaped geometry and the immiscibility between the V-shaped nanoparticles and the tethers

on the self-assembled structures. We show that the V-shaped geometry significantly alters the phase diagram of tethered nanoparticles, and further, the immiscibility between particle and tethers leads to structures not previously predicted for bent-core molecules.

4.1.2 Model and simulation method

We utilize minimal, coarse-grained models and Brownian dynamics (BD) to study the phase behavior of a solution of tethered V-shaped nanoparticles (TVNs) in three dimensions. Our minimal models, which are not restricted to any specific system but instead pertain to a general class of tethered nanoparticles, are developed based on empirical potentials that are successful in capturing the relevant physics of block copolymers, surfactants and colloidal particles[25, 123]. A primary advantage of this approach is that the liquid crystal behavior of the V-shaped nanoparticles and the complex entropic interactions arising from the asymmetry between the rigid nanoparticles and the flexible polymer tethers are automatically incorporated. In this study, we aim to investigate the role of the number and position of tethers of fixed length, the opening angle of the V shape nanoparticles, and the immiscibility between tether and particle, on the resulting self-assembled morphologies.

Model

The computationally efficient model of V-shaped particles that we study here consists of five beads with diameter 1.0σ, arranged rigidly in the shape of the letter "V". The center to center distance between two adjacent beads in a particle is 1.0σ. The particles are connected to tethers via finitely extensible, nonlinear, elastic (FENE) springs[124]. Previous simulations of tethered nanorods showed that rod roughness, which is controlled by the number of beads used to represent the particle, have little effect on the self-assembled structures[19]. Additionally, this model closely relates to the previous simulations of bent-core molecules[120, 121] and recently synthesized colloidal particles[125, 126]. The opening angle of the V group is set to be 140 deg which is the angle normally attained for actual bent-core molecules and used in previous simulations[116, 117, 120, 121]. Flexible tethers are modeled as linear chains consisting of four beads of diameter 1.0σ bonded together via FENE springs. The tether length is chosen to be roughly equal to the distance between two V ends, allowing for direct comparison with moderate aspect ratio tethered nanorods[17, 19]. We consider three geometries of TVNs that are single-end, double-end and laterally tethered as illustrated in Figure 4.1.

To account for solvent selectivity, we assume that the solvent is poor for the nanoparticles

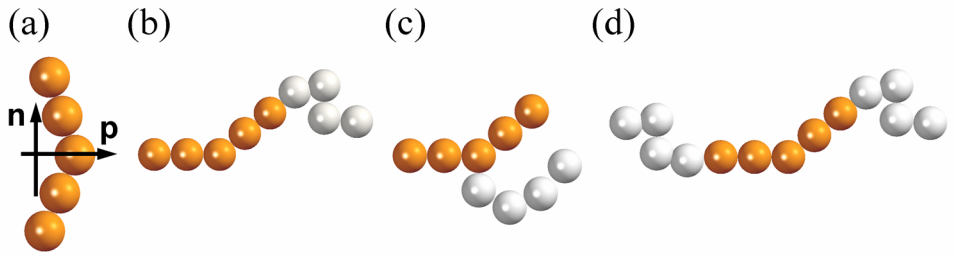

Figure 4.1 Model (a) V-shaped nanoparticle with unit end-to-end vector **n**, and unit polar vector **p**, (b) single end-tethered, (c) laterally-tethered and (d) double end-tethered V-shaped nanoparticles.

and good for the tethers for all cases unless otherwise indicated. The effective interaction between solvophobic V-shaped particles is therefore modeled by a 12-6 Lennard-Jones (LJ) potential between the individual beads of the particles, truncated and shifted to zero at $r_C = 2.5\sigma$, to incorporate short range attraction and excluded volume interaction. The non-bonded interaction between solvophilic tethers is modeled by the purely repulsive Weeks-Chandler-Andersen (WCA) potential between tether beads. WCA is essentially a Lennard-Jones potential truncated and shifted to zero at its minimum.

The thermodynamic immiscibility between nanoparticles and tethers is represented by using the repulsive WCA potential for nanoparticle-tether interactions. In our simulations, the potential energy well depths are chosen to be identical for nanoparticle-nanoparticle, nanoparticle-tether and tether-tether interactions $\varepsilon_{NP-NP} = \varepsilon_{NP-T} = \varepsilon_{T-T} = \varepsilon$. The natural units for these systems are the diameter of a bead, σ, the mass of a bead, m, and the Lennard-Jones well depth, ε. The time scale is defined as $\tau = \sigma\sqrt{m/\varepsilon}$ and the dimensionless temperature is $T^* = k_B T/\varepsilon$. The number density is defined as $\rho = N/V$, where N is the total number of beads and V is the box volume.

Simulation method

We use Brownian dynamics to simulate systems of tethered V-shaped nanoparticles in constant volume and temperature, i.e. the canonical ensemble. We sampled the phase diagram of mono-tethered V-shaped nanoparticles at nine different number densities ρ ranging from 0.1 to 0.9, corresponding to volume fractions from 0.005 to 0.47. The systems are initially athermal, where all interactions are treated with the repulsive WCA potential, at high temperature ($T^* = 1.6$) and low concentration. The simulation box is gradually rescaled until the target concentration is reached. At the target concentration, the system is allowed to become isotropic before selective solvent interactions are activated. We then quench the system following a stepping schedule with a temperature step $\Delta T = 0.1$. At each

intermediate temperature, the systems are equilibrated until the fluctuation of the potential energy falls below 5% over several million time steps. To ascertain that any observed phases are not affected by our finite box size, we simulated systems with N_P = 200, 600, 1000, 1200, 2000 and 3000 building blocks for a fixed number density. We also repeat the simulations with different cooling paths to help avoid kinetically trapped structures at certain concentrations and to ascertain that the predicted structures are independent of thermodynamic path. Using this procedure, we obtained metastable states only when trying to produce perforated lamellar phases with single end-tethered V-shaped nanoparticles in small system sizes, e.g. with N_P = 200 and 600 building blocks. For larger systems, we always achieve equilibrium structures regardless of the cooling schedule. The simulations presented in this work were performed with in-house code, and represent approximately 5000 hours of CPU time on Power G5 2.0 GHz processors.

4.1.3 Results and discussion

Single end tethered V-shaped nanoparticles

The phase diagram of single end-tethered V-shaped nanoparticles is similar to that of tethered nanorods[17], reproducing all phases except the tetragonally perforated smetic phase. Similar to end-tethered nanorods, we observe micelles ordered in a body-centered cubic mesophase structure, hexagonally packed cylinders, hexagonally perforated smectic layers and smectic layers as the volume fraction of the building blocks increases (Figure 4.2). Although the bend in the nanoparticle geometry does not substantially change the mesophase classification, it does change the local packing of the particles within the aggregates, as follows:

Spherical micelles (M) For number densities from 0.1 to 0.3, for $T^* < 0.8$, single end-tethered V-shaped nanoparticles aggregate into micelles. As concentration increases, the micelles are ordered into a body centered cubic morphology (Figure 4.3(a)). To quantify the shape of the micelles, we compute the asphericity parameter[19] which is defined as:

$$A_S = \frac{1}{2}\left\langle \sum_{i>j}^{3} \left(R_i^2 - R_j^2\right)^2 \right\rangle / \left\langle \left(\sum_{i>j}^{3} R_i^2 \right)^2 \right\rangle \tag{4.1}$$

where R_i^2 is the eigen-value of the gyration tensor of each micelle and the average is performed over all micelles in the size range. The asphericity parameter A_S may vary from zero for a spherical micelle to unity for a rod-shaped micelle. Table 4.1 shows that at $\rho = 0.2$,

$T^* = 0.8$, the majority of micelles consist of 35 to 65 particles where the asphericity parameter is close to zero, indicative of a spherical shape. In contrast with the micelles predicted for end-tethered nanorods[19], snapshots of these spherical micelles in Figure 4.3(b) show that the tethers tend to extend radially from the center of the micelle, resulting in an isotropic inter-micelle interaction.

Table 4.1 Average asphericity parameter calculated for the micelles formed by single end-tethered V-shaped nanoparticles at $T^* = 0.8$ and $\rho = 0.2$.

Micelle size	Asphericity parameter
35-40	0.02±0.019
40-45	0.02±0.014
45-50	0.02±0.017
50-55	0.03±0.015
55-60	0.02±0.015
60-65	0.03±0.011

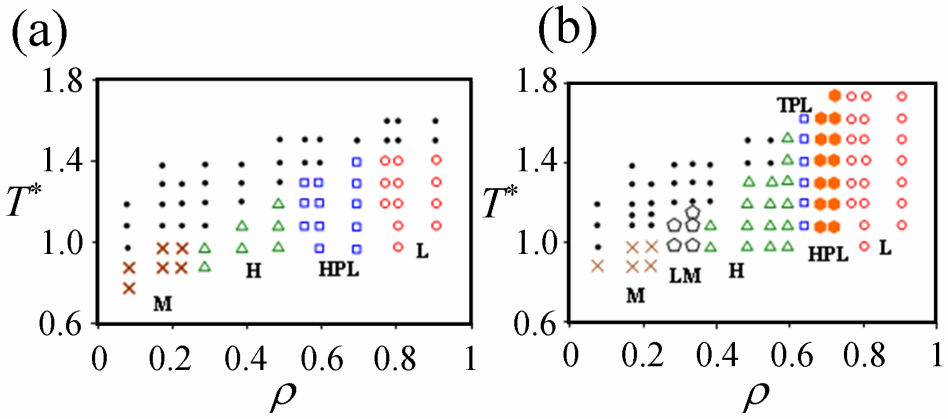

Figure 4.2 Phase diagrams of (a) single end TVNs and (b) end-tethered nanorods (Reproduced from [17].) Black filled circles are disordered states. Symbols indicate ordered mesophases. Left: spherical micelles (M), hexagonally packed cylinders (H), hexagonally perforated smectic (HPL), smectic (L). Right: cubic micelle phase (M), long micelle (LM), hexagonally packed cylinders (H), tetragonally perforated smectic (TPL), hexagonally perforated smetic (HPL) and smectic (L).

Hexagonally packed cylinders (H) For $0.3 < \rho < 0.56$, hexagonally packed cylinders are formed for $T^* < 1.2$ (Figure 4.4(a)). Hexagonally packed cylinders are theoretically predicted and experimentally observed for bent-core molecules[127][55], block copolymers[56] and other shape amphiphiles such as end-tethered nanorods[17, 19], tethered nanospheres[34], and tethered nanocubes[20]. Although there are random defects along each cylinder, the packing of the nanoparticles within each cylinder is similar to that predicted for the rectangular columnar phase (B1) of bent-core molecules[98], in which the V-shaped nanoparticles nest together in cross section with the polar direction perpendicular

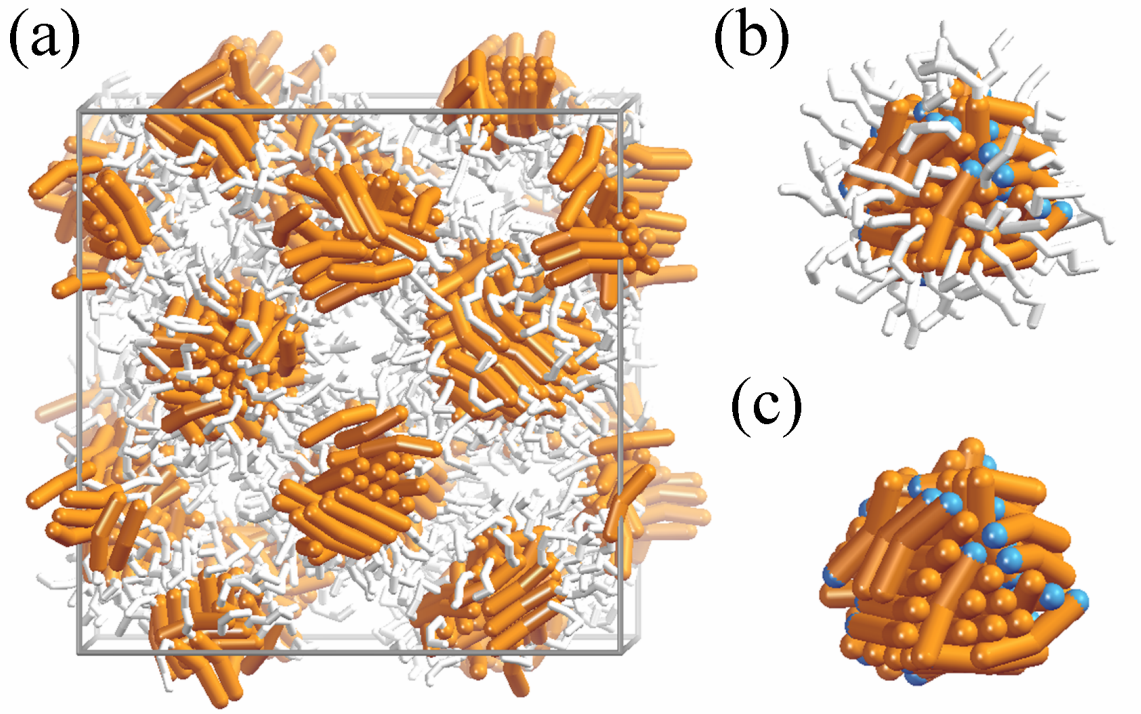

Figure 4.3 (a) BCC micelles (M) formed by N_P = 1000 single end-TVNs at $T^* = 0.8$ and $\rho = 0.3$. The circles are guides to the eyes: the smaller circles indicate the micelles in the center of a unit cell, the larger circles indicate the micelles on the corners. (b) Snapshot of a spherical micelle consisting of 57 building blocks. (c) The micelle core with tethers removed. Rod ends without tethers are colored blue.

to the cylinder axis (Figure 4.4(b)). Nonetheless, while the nested packing of V-shaped nanoparticles is strongly energetically favored, it also induces an entropic penalty that can be mitigated either by nanoparticles tilting with respect to the interfacial normal, increasing the distance between tether anchor points, or by switching the anchor points randomly from one side to another. Additional entropy is achieved by randomly alternating the polar direction of bundles of nested nanoparticles, to reduce the tether overcrowding (Figure 4.4(c)). This suggests that it is the immiscibility of tethers and particles, which is absent in previous simulations of bent-core molecules[128], that results in additional orientational order within each cylinder. Moreover, Figure 4.4(c) also indicates that the nanoparticle-tether junctions are ordered locally into a hexagonal packing, and thus are restricted to planar interfaces which prohibit a relative twist between adjacent nanoparticles. This explains why single end-tethered V-shaped nanoparticles do not exhibit a smooth and uniform twist along the cylinders as predicted for end-tethered nanorods[19].

3D hexagonal perforated smectic phase (HPL) For $0.56 < \rho < 0.7$, we observe an intermediate morphology between columnar and lamellar phases (Figure 4.5(a)). As ρ increases

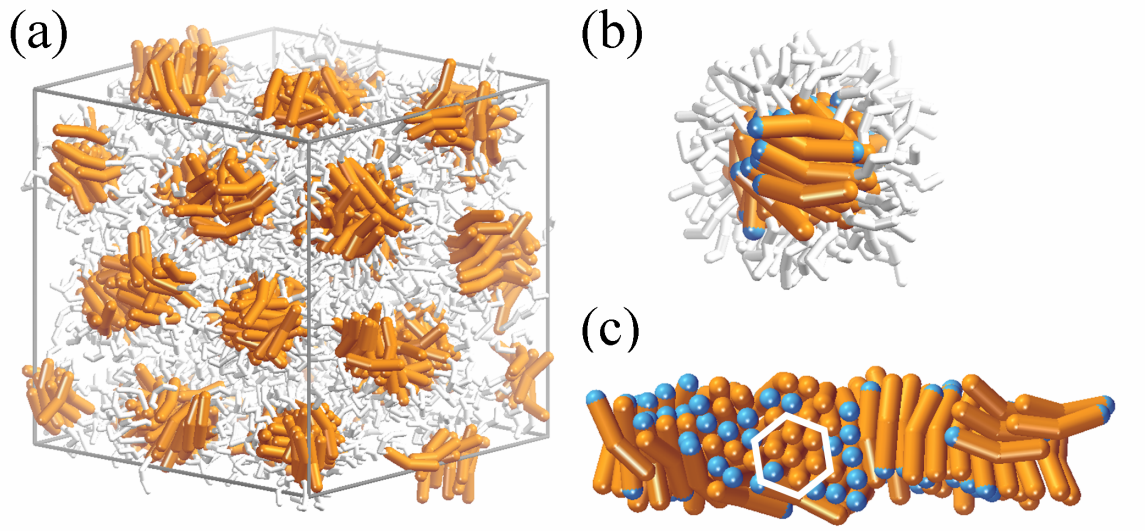

Figure 4.4 (a) Hexagonally packed cylinders (H) formed by N_P = 600 single end TVNs at $T^* = 0.8$ and $\rho = 0.4$. (b) An example of the cross-section of a cylinder. (c) A snapshot of a cylinder with tethers removed. Ends without tethers are colored blue.

from that of the cylinder phase, the repulsion between aggregates induces a morphological change towards a higher interfacial surface to volume ratio. When quenching a disordered system, we observe that the nanoparticles first form interconnected tubes with the tethers extending outside. As T^* decreases further, the interconnected tubes merge and rearrange into sheets to maximize the distance between repulsive aggregates and minimize interfacial areas. Because the sheets are formed by the combination of tether-coated interconnected tubes, they are perforated by the tethers already occupying the merge space. Packing the nanoparticles into sheets is energetically favorable for the nanoparticles, but is entropically unfavorable for the tethers. The entropic penalty induced by the high grafting density of the tethers can then be alleviated by the following factors. First, the nanoparticles pack with tether anchor points distributed randomly on both sides of the sheet. Second, the perforations in each sheet are ordered into a hexagonal lattice as shown in Figure 4.5(b), which allows for a uniform distance between neighboring perforations, and hence, reduces the entropic penalty caused by packed nanoparticles between perforations. And finally, the perforations are arranged between sheets in a 3D ordering to maintain the constant and lowest concentration of tethers at each perforation. Since the perforations in layers closely relate to the excluded volume interactions between the tethers, these 3D structures have not been predicted for bent-core molecules in previous simulations where the terminal chains were ignored[120, 121].

We did not observe the tetragonally perforated smectic phase as predicted for tethered

nanorods in Reference [17], even within the same window of number densities. As pointed out in Reference [17], the key factor that gives rise to the tetragonally perforated lamellar phase is that the nanorods must align with the sheet normal. This orientation is clearly impossible for bent rods.

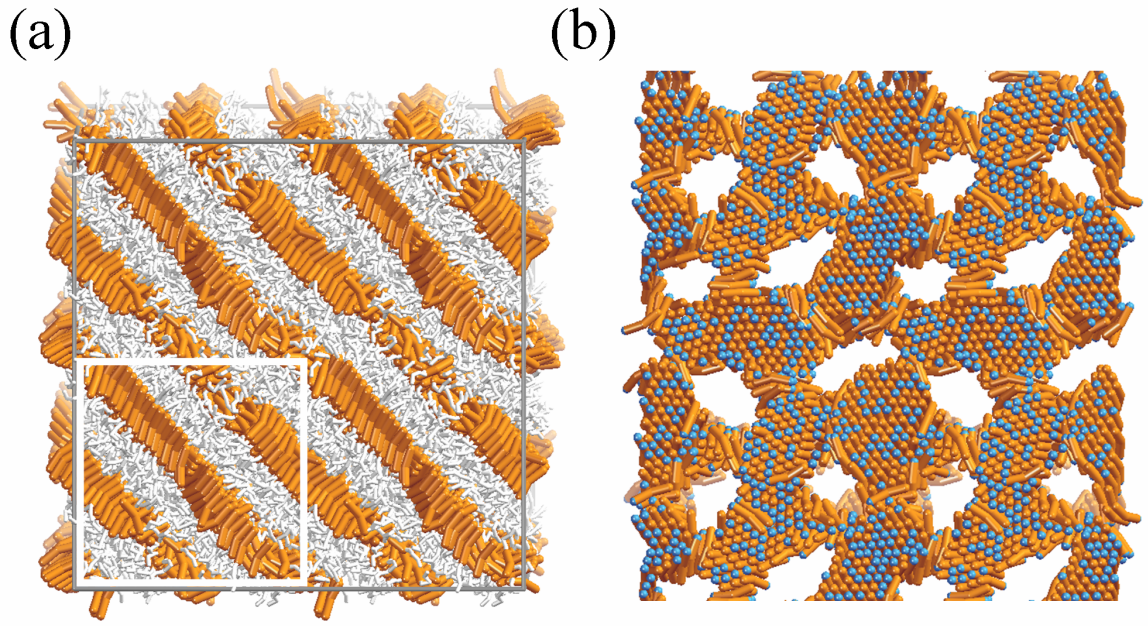

Figure 4.5 (a) Perforated smectic (PL) formed by N_P = 2000 single end TVNs at $T^* = 1.3$ and $\rho = 0.6$. The unit cell is highlighted. (b) Snapshot of a perforated layer with tethers removed. The ends without tethers are colored blue.

Smectic phase (L) At $0.8 \leq \rho \leq 0.9$ we observe a smectic phase at temperatures at and below $T^* = 1.4$. As compared to end-tethered nanorods [17] which form smectic phases at $T^* \approx 4.0$, the packing of V-shaped particles into layers is more difficult, requiring alignment along two axes vs. one. Consequently, at high density, ordered phases appear at lower temperatures as compared with tethered rods. With $N_P = 2000 - 3000$ building blocks, we observe three independent layers as shown in Figure 4.6(a). Here the intralayer fluctuation is much less than in the lamellar phase formed by tethered nanorods [17] because the V-shaped nanoparticles nest within each other to achieve optimal packing, thereby providing additional stability within each layer. Moreover, as indicated by the split second peak of the two-dimensional nanoparticle-nanoparticle distance correlation function (Figure 4.6(b)), the nanoparticles within each layer pack into a regular hexagonal lattice [121] with tether anchor points alternated randomly on both sides to reduce the grafting density of tethers. Edge-on views of the layers (Figure 4.6((a)) show that the nanoparticles exhibit a uniform tilt with respect to the interfacial normal, maximizing the distance between tether-anchor points, and thus, allowing the tethers to have more free volume. For $0.9 < T^* < 1.4$, the

tilt angle varies from $29^\circ - 31^\circ$, which is consistent with previous simulations[121] and experimental observations[102, 104]. Interestingly, owing to their two-dimensional geometry, the tilting V-shaped nanoparticles result in a well-defined handedness within each layer, which is unavailable for the smectic phase in tethered nanorod systems. Figure 4.6(c) reveals that V-shaped nanoparticles within a sheet tilt to allow for an efficient packing of adjacent spherical beads. To quantify the handedness of each layer, we measure the average chiral order parameter with the RMS average chiral fluctuations:[120]

$$\bar{\chi} = \frac{1}{M}\sum_{i=1}^{M}\chi_i \tag{4.2}$$

$$\chi_{RMS} = \frac{1}{M}\sum_{i=1}^{M}(\chi_i - \bar{\chi})^2 \tag{4.3}$$

Here χ_i is the chiral order parameter of a V-shaped nanoparticle which is defined as:[120]

$$\chi_i = [(\mathbf{m}\times\mathbf{n}_i)\cdot\mathbf{p}_i](\mathbf{m}\cdot\mathbf{n}_i) \tag{4.4}$$

Here $\mathbf{m}$ is the local sheet normal, and $\mathbf{n}_i$ and $\mathbf{p}_i$ are the end-to-end vector and unit polar vector of the nanoparticle, respectively. At equilibrium, for all layers, the average chiral order parameter is remarkably greater than the RMS average chiral fluctuations, indicative of a well-defined chirality. For example, for the snapshot shown in Figure 4.6a) we obtain $(\bar{\chi};\chi_{RMS})$ = $(-0.41\pm0.006;\ 0.04\pm0.011)$, $(0.39\pm0.008;\ 0.09\pm0.018)$ and $(-0.42\pm0.004;\ 0.04\pm0.001)$ for each layer, respectively. Although the current results are reminiscent of the chiral smectic C phase (B2) formed by bent-core molecules, we hypothesize that the chirality varies randomly from layer to layer because adjacent layers are only weakly coupled by the excluded volume interactions between the tethers[120]. This can be attributed to the absence of directionally-favored interactions to help guide the inter-layer correlation as in the simulations of Johnston et al.[116]

Laterally tethered V-shaped nanoparticles

The previous simulations of Horsch et al.[18] showed that laterally-tethered nanorods form stepped ribbons and two kinds of bilayer sheets with different crystalline interlayer packing of symmetry P_2 and C_{mm}, respectively, in a solution good for the tethers and poor for the nanorods; the bilayer sheet mesophases have been recently confirmed experimentally[129]. The interaction between tethers are modeled by the repulsive WCA potential in that case. Meanwhile, for bent-core molecules in a melt state, it is reasonable to assume that the

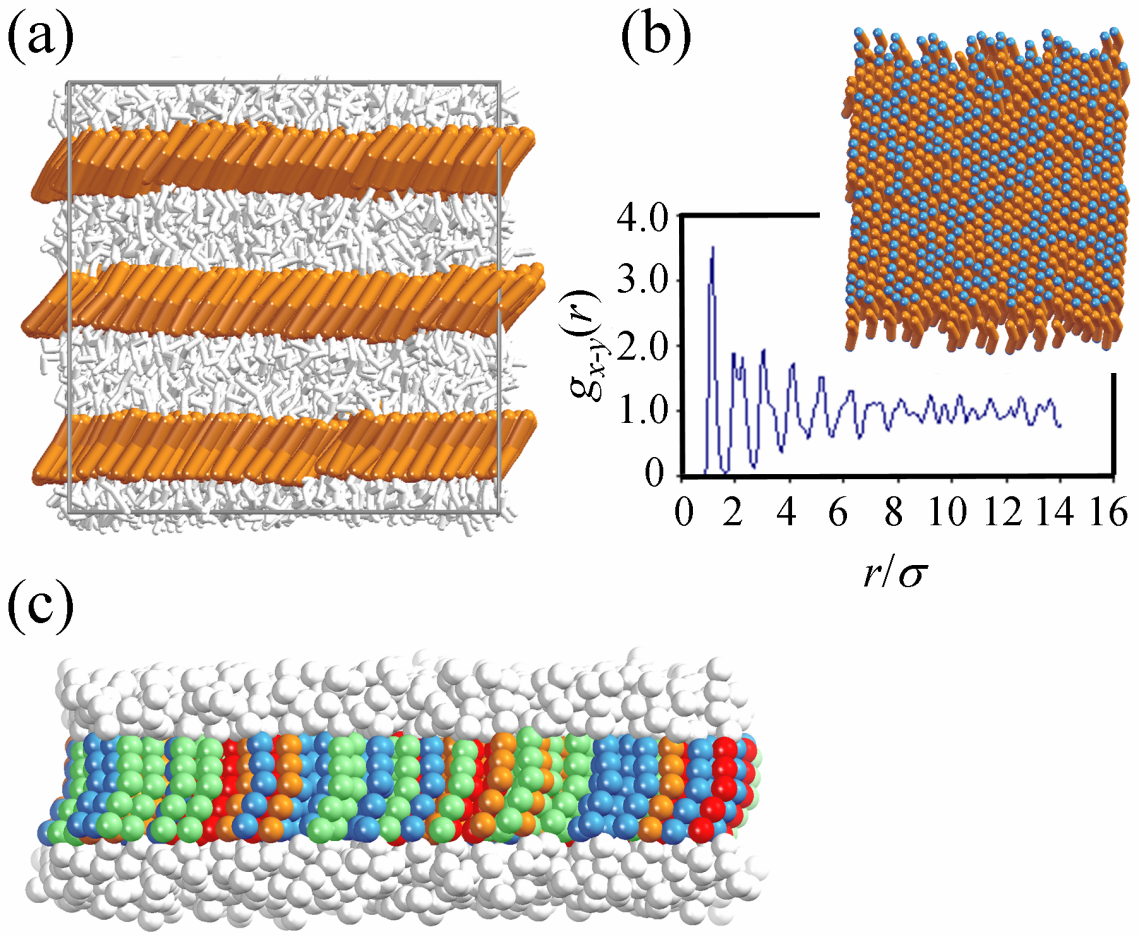

Figure 4.6 (a) Smectic phase (L) formed by N_P = 2000 single end-TVNs at $T^* = 1.3$ and $\rho = 0.8$. (b) Nanoparticle distance correlation within the layer shown in the inset. The blue ends are without tethers. (c) Local packing of the bumpy V-shaped nanoparticles within a sheet.

terminal hydrocarbon chains are attractive to each other and repulsive to the rigid aromatic cores. Consequently, to compare laterally tethered V-shaped nanoparticles with laterally tethered nanorods with implications for bent-core molecules, we examine both cases of the tether interactions independently.

Non-attractive tethers In contrast with the laterally tethered nanorod system, we find that laterally TVNs do not assemble into stepped ribbons and bilayer sheets with different rod packing within the layers. Instead, we observe an interconnected tube phase and a lamellar phase neither of which have been previously reported for V-shaped nanoparticles. The phase behavior is strongly dependent upon the nanoparticle geometry as shown in Figure 4.7. Moreover, as compared to laterally-tethered nanorods[18], we observe a decrease in the disorder-order temperature of the lamellar phase (Figure 4.7(b)), reflecting the complex

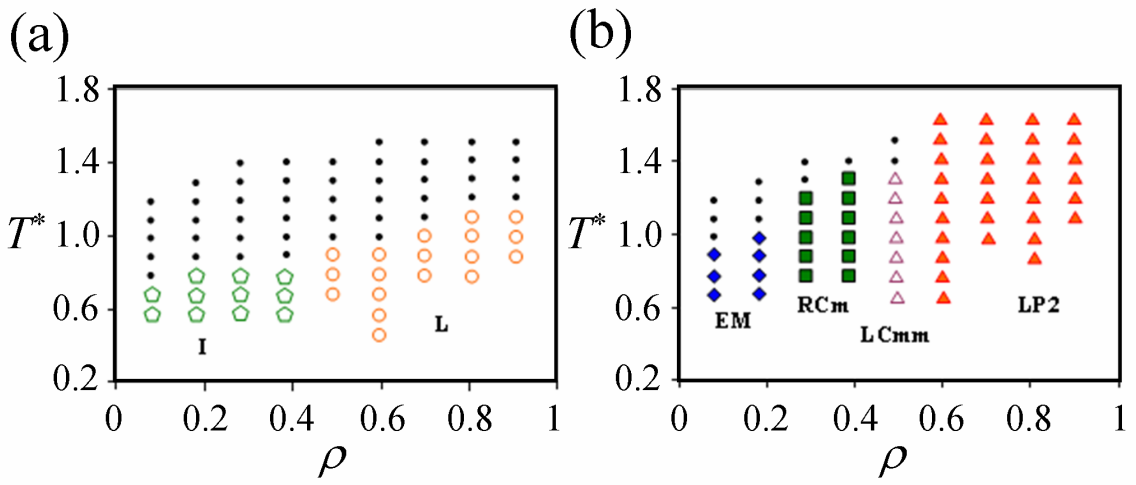

Figure 4.7 Phase diagrams of (a) laterally TVNs and (b) laterally-tethered nanorods (Reproduced from [19]). Black filled circles indicate disordered states. Symbols indicate ordered mesophases. Left: interconnected tubes (I) and lamellae (L). Right: elongated micelles (EM), stepped ribbons ($R_{C_{mm}}$), C_{mm}-packing lamellae ($L_{C_{mm}}$) and P_2-packing lamellae (L_{P_2}).

shape of the V-shaped nanoparticles compared to nanorods and the relative difficulty of the ordering process at high densities.

Interconnected tubes (I) Complex 3D morphologies are formed for $0.2 < \rho < 0.5$ (Figure 4.8(a)). We find that in these structures the V-shaped nanoparticles form a network of interconnected tubes without any specific order. These complex structures result from the competition between the V-shaped nanoparticles attempting to maximize their contacts and the tethers attempting to minimize their elastic strain. The nonzero curvature in the networks is formed as a compromise between the V-shaped nanoparticles aggregating to minimize energy and the tethers extending to maximize entropy. To ascertain the equilibrium nature of this structure, we ran five simulations with different cooling paths at each concentration. The average nanoparticle distance correlation (not shown) and the system potential energy at the target temperature indicate that these structures are stable and reproducible. Though we have not been successful in determining if these structures have any specific periodic ordering, the existence of this mesophase demonstrates that a bend in the nanoparticle shape can lead to a substantial change in the phase behavior of laterally-tethered nanorods.

Lamellar phase (L) We find a lamellar phase at number densities from 0.5 to 0.9 at $T^* < 0.9$ (Figure 4.8(b)). The lamellar phase here is completely different from the tilted smectic phase formed by either end-tethered V's or end-tethered nanorods[17, 19], in that the V-shaped nanoparticles lie in the plane of each layer. In that respect, the morphology is more similar to that observed for laterally-tethered nanorods[18], although here the particles do not form bilayer sheets. However, the observed morphology is similar to lamellar

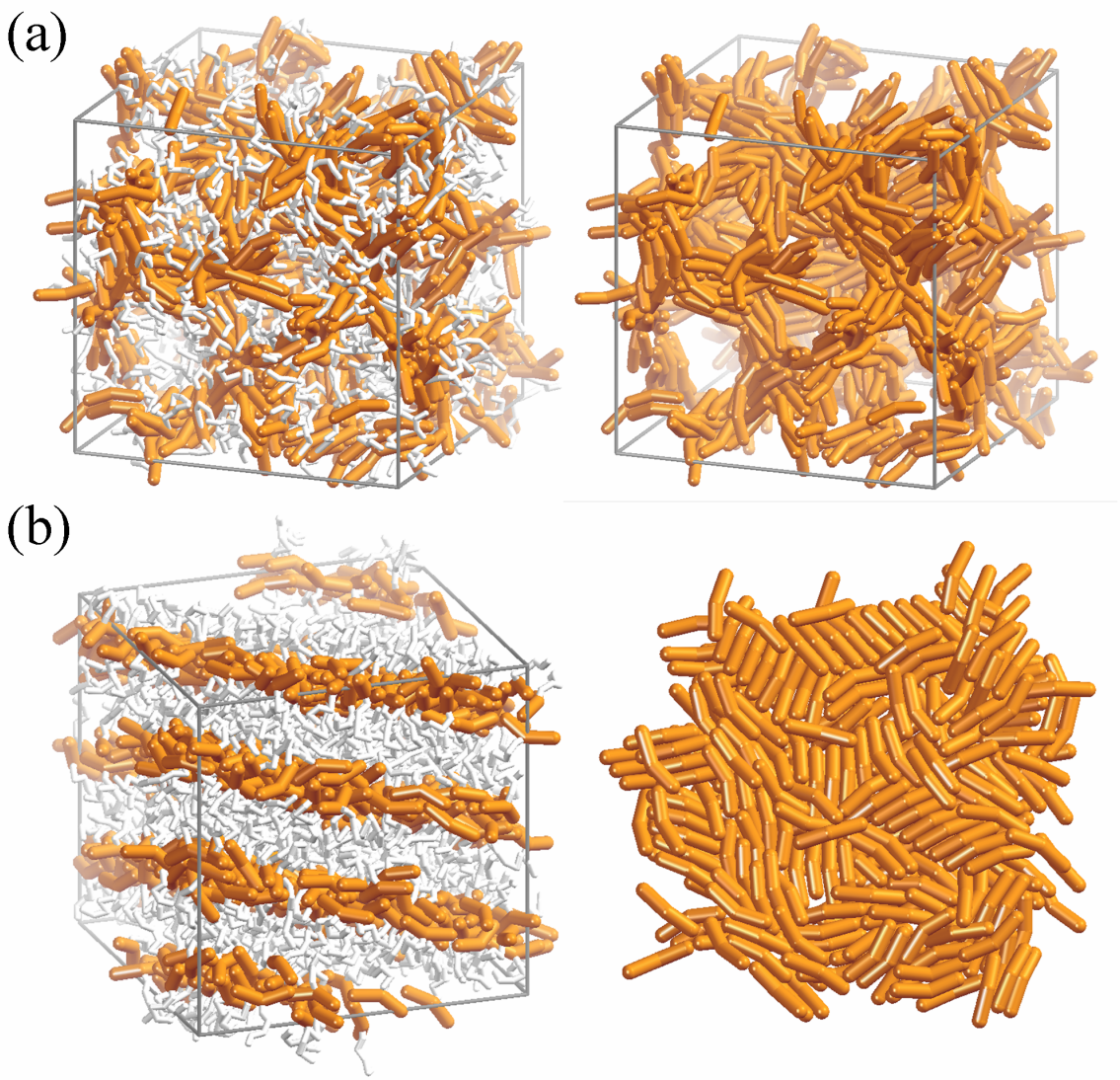

Figure 4.8 Structures formed by N_P = 1200 laterally TVNs. (a) Interconnected tubes (I) at $T^* = 0.8$ and $\rho = 0.4$. The image on the right shows the structure with tethers removed. (b) Lamellar phase (L) at $T^* = 1.0$ and $\rho = 0.6$. The image on the right shows an example of a layer with tethers removed.

structures that are experimentally observed and theoretically predicted for lateral rod-coil block copolymers[130]. Figure 4.8(b) shows that within a sheet the V-shaped nanoparticles fit together locally to maximize their contacts, but there is no long range order because their alignment is randomly disturbed by the tethers attempting to maximize their free volume.

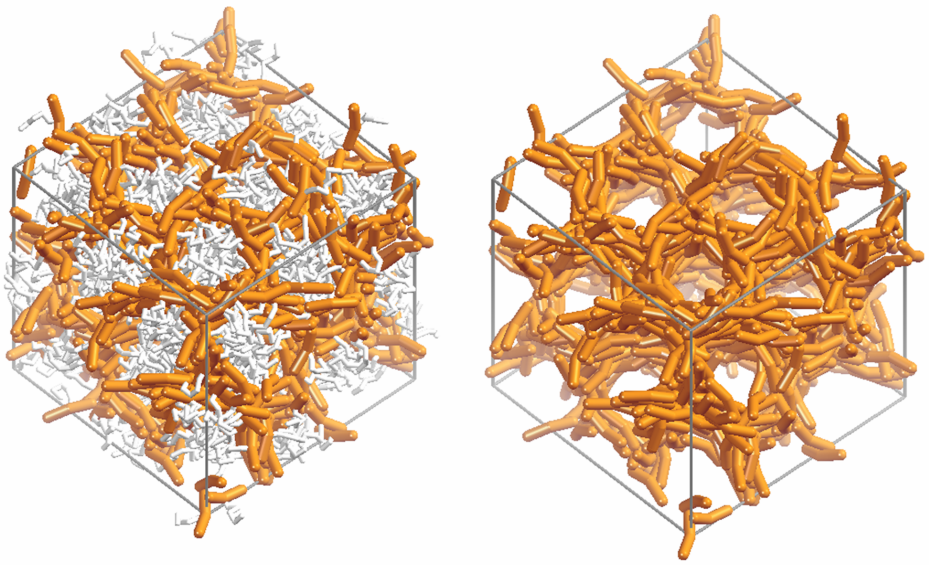

Figure 4.9 Honeycomb phases formed by N_P = 1000 laterally TVNs at $T^* = 1.3$ and $\rho = 0.6$. The image on the right shows the structure with tethers removed.

Attractive tethers To model the attraction between tethers we use the Lennard-Jones potential between tether beads instead of the WCA potential used in the previous case. Interestingly, we observe the honeycomb structures as shown in Figure 4.9 (over a wide range of number densities from 0.3 to 0.8. The honeycomb structures are in agreement with those experimentally observed for lateral rod-coil block copolymers[130] where the incompatibility between rods and coils plays a vital role in the microphase separation of the system. Simulation snapshots reveal that the tethers pack into hexagonally packed cylinders and the V-shaped nanoparticles form a connected network (Figure 4.9). The radius of the cylinders approximates the average end-to-end distance of the tethers. It is therefore evident that a change in the interaction between the tethers results in a complete change of the phase behavior of the system.

Double end tethered V-shaped nanoparticles

The phase diagram of double end tethered V-shaped nanoparticles with attractive V particles and repulsive tethers is sketched in Figure 4.10. As compared to single end TVNs, we

also observe cubic ordered micelles, elongated micelles and hexagonally packed cylinders; however, no smectic phases are found, presumably because of the high volume fraction of the tethers.

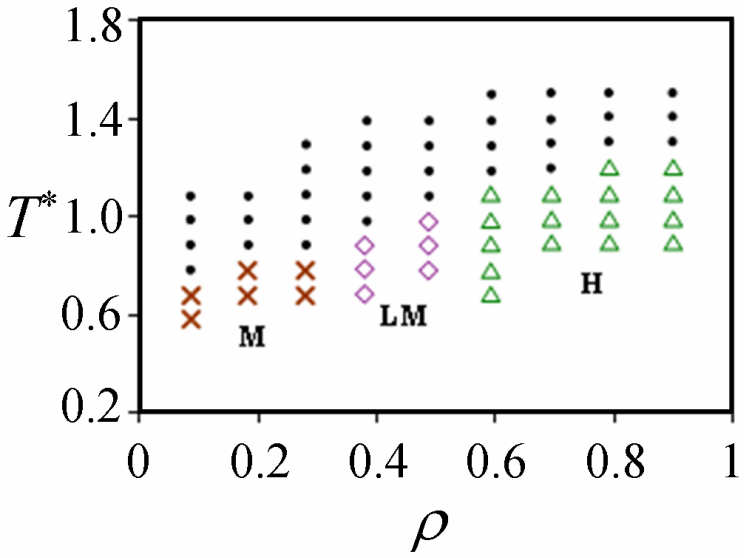

Figure 4.10 Phase diagram of double end TVNs. Black filled circles are disordered states. Symbols indicate ordered mesophases: spherical micelles (M), long micelles (LM) and hexagonally packed cylinders (H).

Spherical micelles (C) For $0.1 < \rho < 0.3$, we observe micelles as $T^* < 0.8$ as shown in Figure 4.11(a). At sufficient concentrations, the micelles form a body-centered cubic morphology. The average number of V-shaped nanoparticles in each micelle is smaller than the micelles formed by single end-tethered nanoparticles, presumably due to the larger excluded volume of the tethers attached at both ends of the V-shaped nanoparticles. Figure 4.12 shows the remarkable difference in the average size of the micelles formed by single end-tethered and double end-tethered nanoparticles. We use the asphericity parameter to quantify the micelle shape and find that the micelles are also spherical. For example, at $\rho = 0.3$ and $T^* = 0.5$, we obtain $A_S = 0.02 \pm 0.018$, indicative of spherical shape. Additionally, simulation snapshots (Figure 4.11(b)) reveal that within a micelle the nanoparticles assume a twist between neighbors to compensate for the elastic strain in the tethers.

Long micelles (LM) For $0.3 < \rho < 0.4$, elongated micelles are formed at $T^* < 1.0$ (Figure 4.13(a)). As the concentration of the system increases, the micelles expand to accommodate more V-shaped nanoparticles. We observe that the micelles are stretched into rod-like aggregates because of the nanoparticles attempting to nest together to minimize energy and the tethers attached at their two ends attempting to maximize their free volume (Figure 4.13(b)). One consequence of this is that the micelles grow into irregularly twisted ribbons

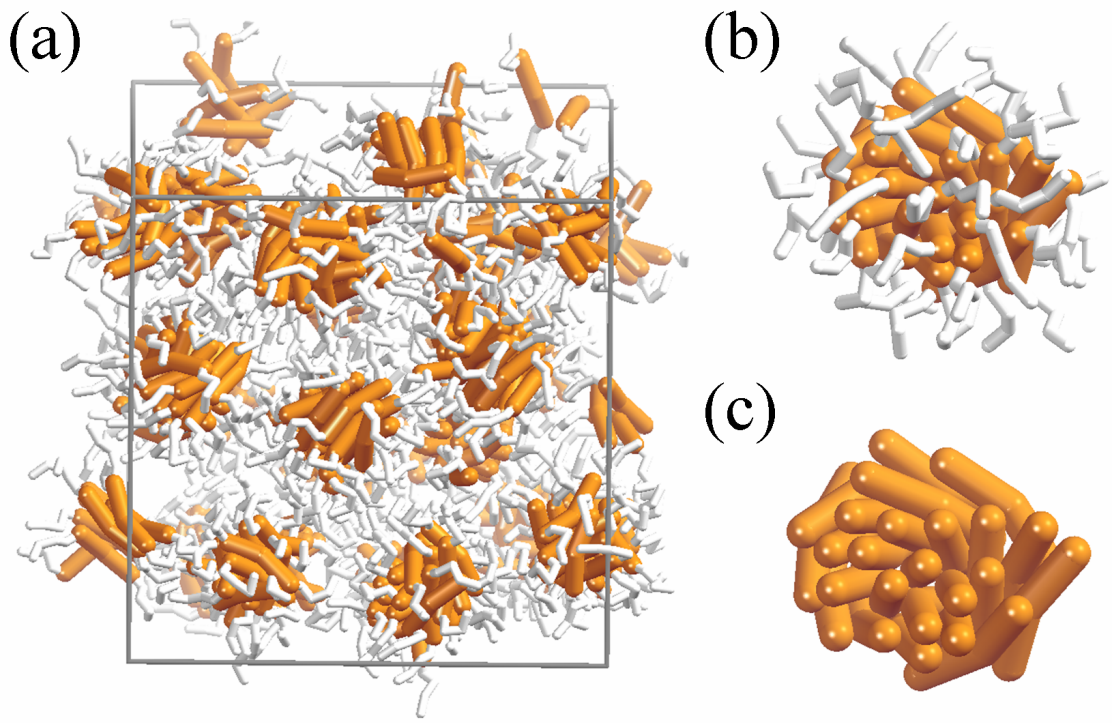

Figure 4.11 (a) BCC micelles (M) formed by N_P = 600 double end TVNs at $T^* = 0.7$ and $\rho = 0.3$. (b) Snapshot of a spherical micelle consisting of 19 building blocks. (c) The micelle core with tethers removed.

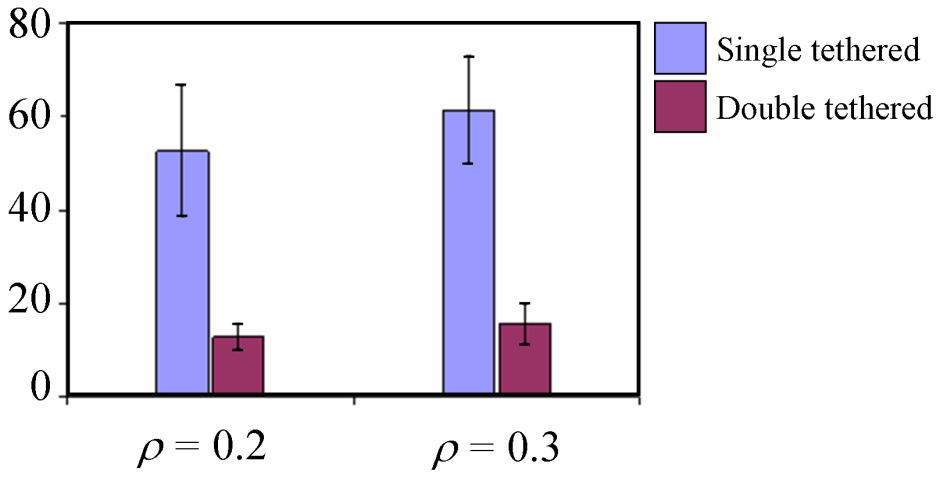

Figure 4.12 Average size of micelles (i.e. number of nanoparticles per micelle) formed by single end TVNs (light color) and double end TVNs (dark color).

of which an example is shown in Figure 4.13(c). We again use the asphericity parameter to quantify the micelle shape and an example of the asphericity parameter as a function of the micelle size is given in Figure 4.14. The asphericity parameter of large micelles approaches unity, indicative of rod-like shapes. Although the micelle size is non-uniform, we observe that the micelles are nematically ordered. Similar to the tethered nanorod system[19], the nematic order here results from the anisotropic interaction between micelles, which, because of their rigid cores, behave like rods.

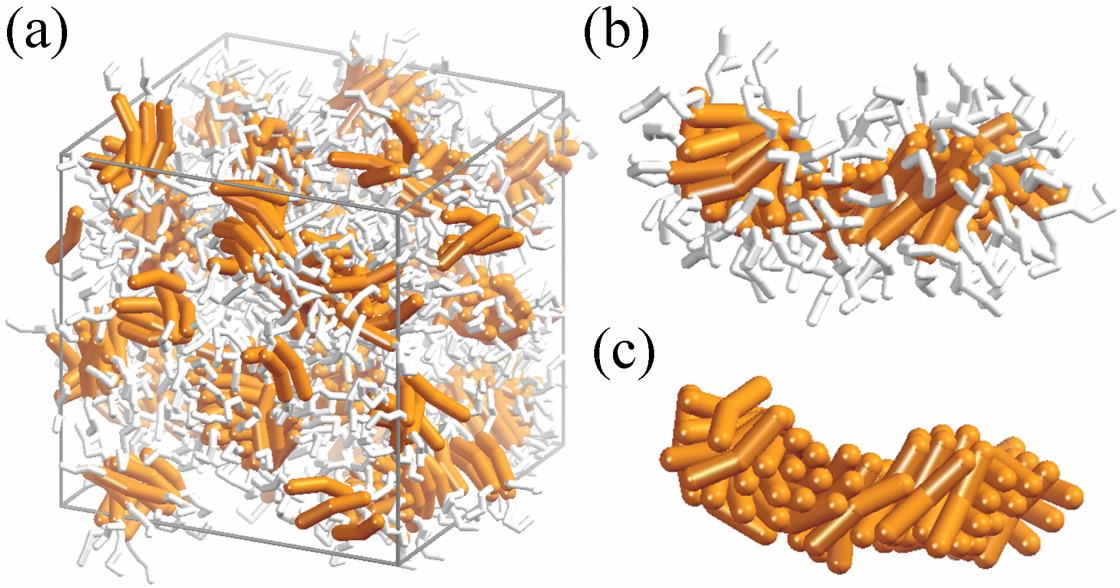

Figure 4.13 (a) Elongated micelles (LM) formed by N_P = 600 double end TVNs at $T^* = 0.9$ and $\rho = 0.5$ (b) Snapshot of an elongated micelle consisting of 45 building blocks. (c) The micelle core with tethers removed.

Hexagonally packed cylinders (H) As the concentration of the system increases, nematically ordered elongated micelles grow and merge to form cylinders. We observe a hexagonally packed cylinder phase as the number density is increased from 0.4 to 0.8 and $T^* < 1.2$ (Figure 4.15(a)). Although the hexagonally packed cylinder phase is commonly seen in nanoparticle-polymer systems, it is not usual in bent-core molecule systems. In the columnar phases formed by bent-core molecules, the columns form a rectangular lattice and within each column the molecules are proposed to pack in parallel such that their polar direction is either parallel (B1) or perpendicular ($B1_{rev}$) to the cylinder axis[98, 131]. Gorecka et al. reported the first examples of hexagonally packed columnar phases (Col_h) for polycatenar bent-core molecules[127]. They further predicted that the cross section of each column consists of four molecules organized into a star-like shape. In our cylinder phase, however, the V-shaped nanoparticles are not only favored to nest together to maximize their contacts, but they also tilt with respect to the interfacial normal to increase the distance

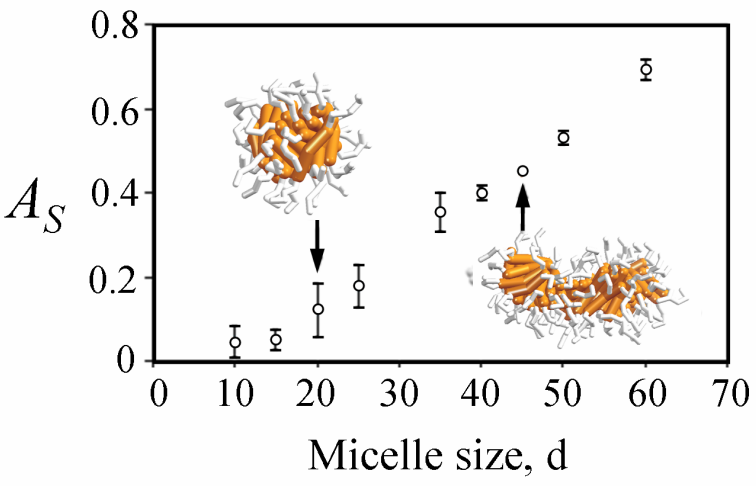

Figure 4.14 Shapes of micelles formed by N_P = 600 double end TVNs at $T^* = 0.9$ and $\rho = 0.5$. The asphericity parameter is plotted as a function of the size, d, of the micelle. Individual micelles of size d = 19 and d = 45 are added as nsets to aid the visualization of the asphericity parameter.

between tether anchor points, leading to a twist between nanoparticles in each cross section (Figure 4.15(b)). An example of a cylinder in Figure 4.15(c) shows that the twist in the cylinders is more irregular and randomly disturbed than that in the case of single end-tethered V-shaped nanoparticles, apparently due to the higher density of the tethers. Because the repulsive tether-coated cylinders are effectively repulsive to each other, the hexagonal lattice is entropically favored to maintain a constant spacing between neighbors.

It is interesting to note that, despite the similarity between our model double end TVNs and the model molecules used in Reference [122], we do not observe any smectic-layer structures. This can be attributed to the exclusion of the dipole-dipole interaction between the V groups and the inclusion of the excluded volume interaction between the tethers in our simulations. Double-end TVNs are an example of ABA triblock copolymers in which the B group has a rigid bent shape. Therefore, we expect their mesophases to be similar in part to those known for ABA triblock copolymers. Depending on the relative volume fraction of A and B copolymers, self-assembled structures can range from spherical micelles, cylinders, 3D bicontinuous, perforated lamellae and lamellae[132]. In our simulations, a double-TVN is analogous to an A4B5A4 triblock copolymer where lamellar structures are suppressed, presumably due to the high relative volume fraction of tethers, which dominates entropic effects. We further postulate that in order for the double end tethered V-shaped nanoparticles to assemble into smectic phases as in bent-core molecules the tethers should be significantly shorter than the rigid nanoparticle. We have examined model building blocks with the tethers consisting of two beads (e.g. the A2B5A2 configuration) to test this hypothesis. Preliminary results indicate that lamellar structures are eventually formed at sufficiently

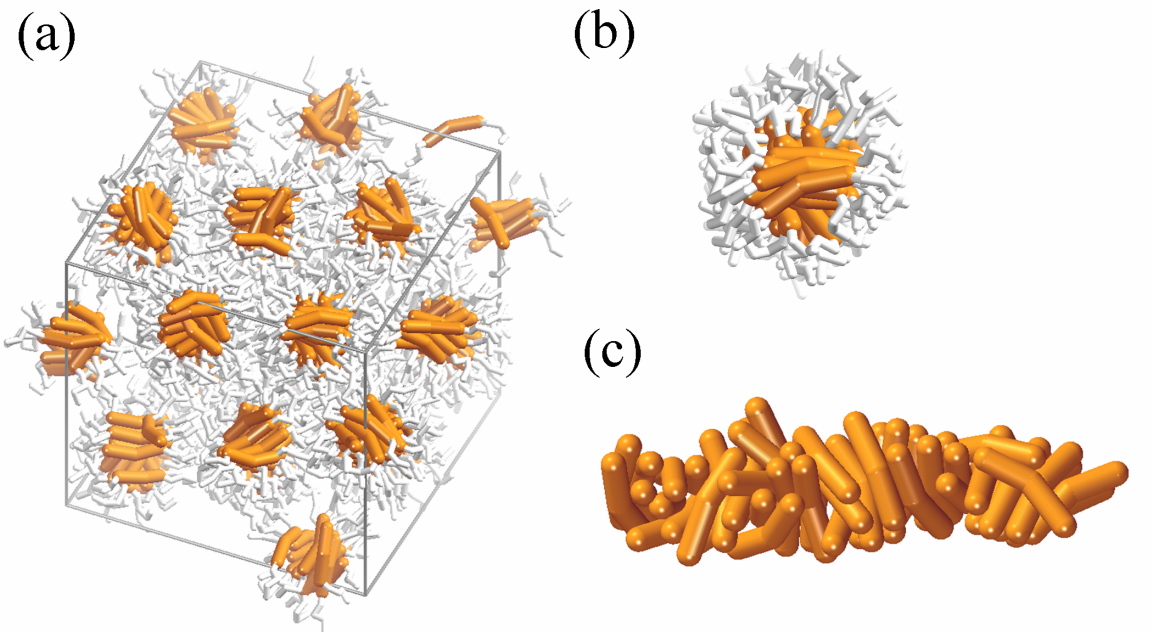

Figure 4.15 (a) Hexagonally packed cylinders (H) formed by N_P = 600 double end TVNs at $T^* = 0.7$ and $\rho = 0.5$ (b) Snapshot of the cross-section of a cylinder. (c) Snapshot of a cylinder with tethers removed.

high concentrations (e.g. $\rho = 0.8$) (Figure 4.16). Further investigation of this geometry will be the focus of future work.

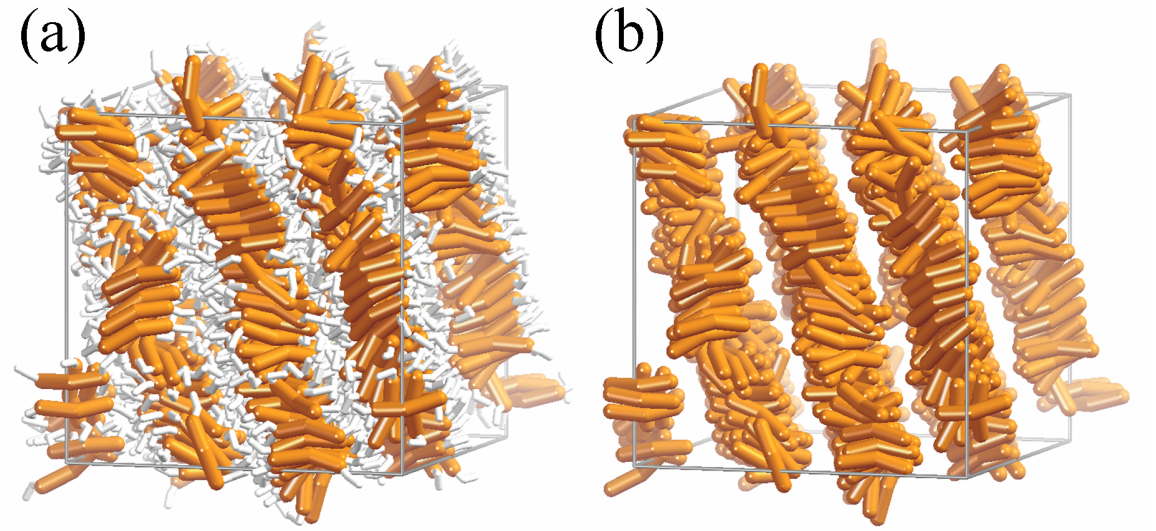

Figure 4.16 (a) Smectic phase formed by N_P = 1000 double end TVNs, of which each tether consists of two beads, at $T^* = 0.9$ and $\rho = 0.8$. (b) The structure with tethers removed for a clear visualization of layers.

4.1.4 Conclusion

We present here the phase diagrams of tethered V-shaped nanoparticles with three different geometries. We have demonstrated that building block architecture significantly affects both the mesophase behavior and local packing of self-assembled structures. While the phase behavior of single end-tethered V-shaped nanoparticles has much in common with end-tethered rods, the local packing within the mesophases is distinguished by the neat packing of the V-shaped nanoparticles. Most interesting is the spontaneous chiral symmetry breaking occurring due to the emergent chirality of V-shaped nanoparticles in smectic phases, which is unavailable for linear nanorods. For laterally tethered V-shaped nanoparticles, the bent-shape geometry completely changes the phase behavior as compared to that of laterally-tethered linear rods, resulting in a previously unreported interconnected structure as well as a lamellar phase. By changing the interactions between tethers from repulsive to attractive, we observe a completely different morphology, the honeycomb structure, over a wide range of concentrations. Meanwhile, the bulkiness of immiscible tethers in the double end-tethered V-shaped nanoparticle, a mesoscale analog of bent-core molecules, is shown to suppress the formation of lamellar structures. Instead we observe a hexagonally packed cylinder phase where the local packing has not been predicted for bent-core molecules. Our results also indicate that short-range interactions and excluded volume – though sufficient to induce chiral symmetry breaking in smectic-like phases as previous computational work reported – would not be adequate to produce any long-range ordered structures such as the twist grain boundary (B4) or tilted smectic (B2) phases with bent-core molecules.

4.2 Self-limiting aggregation of polydisperse nanoparticles

Recent experiments have shown that inorganic nanoparticles (NPs) comprised of CdSe, CdS, ZnSe, and PbS with highly non-uniform size distributions spontaneously assemble into uniformly sized supraparticles (SPs) with core-shell morphology. The uniformity of the SPs results from a self-limiting growth process which distinguishes them from other NP assemblies and agglomerates. We develop a coarse-grained model of the NPs to elaborate experimental findings, demonstrating that the formation of the spherical SPs is governed by a balance between electrostatic repulsion and van der Waals attraction. Furthermore, simulations reveal that the core-shell morphology is a consequence of the size segregation due to NP polydispersity. The generic nature of these interactions provides great versatility in the composition, size and shape of the constituent NPs, and leads to a large family of

self-assembled structures, including hierarchically organized colloidal crystals[2]

4.2.1 Introduction

Nanoparticles (NPs) are known to assemble into larger microscale structures under conditions of strongly anisotropic interactions[14, 24, 25, 134] when prepared as binary mixtures of monodisperse NPs, or when highly monodisperse with mostly isotropic repulsion[37, 135–147]. The faceted shapes of crystalline NPs in particular facilitate attraction along specific axes and increase the complexity of the produced structures. For the majority of diverse NP assemblies forming spontaneously in bulk solutions[42, 148–150], the aggregation occurs continuously until the components are exhausted as their net interaction is purely attractive. In many cases the aggregation can be affected by strongly non-equilibrium processes, and therefore, the products depend on kinetic factors and especially on the uniformity of the individual NPs. A self-limiting self-assembly process involving only inorganic particles, highly non-uniform in size, and resulting in highly ordered terminal structures would be conceptually different from currently known self-organization reactions at the nanoscale. If such assemblies could be fabricated easily and inexpensively, they would have significant practical implication for a host of applications ranging from transformation optics to photovoltaics and drug delivery. Since self-limiting structures are common in biological systems, their realization for inorganic nanocrystals might lead to unexpected parallels between the world of inorganic colloids and biomacromolecules, while providing key insights into the fundamental ingredients needed for the self assembly of uniform structures whose complexity can ultimately compete with the sophistication and dynamism of biological systems. Here we show that such assembly is indeed possible and requires only competing, isotropic forces. The assembly mechanism is simple, yet generic, and can lead to complex semiconductor and metal-semiconductor SPs displaying a significant degree of geometrical uniformity and geometrical shapes both with and without anisotropy, beginning from precursor NPs highly non-uniform in size.

The section is structured as follow. First, we introduce the key experimental results and analysis from Kotov group, showing the evidence of highly uniform SPs due to a self-limiting aggregation process and of the core-shell morphology. Next, we propose a coarse-grained NP model with which the balance between van der Waals attractions and electrostatic repulsions is reproduced. The self-limiting aggregation occurs as the repulsion

[2]This section is adapted from Reference [133] Y. Xia, T. D. Nguyen, M. Yang, B. Lee, A. Santos, P. Podsiadlo, Z. Tang, S. C. Glotzer, N. A. Kotov, Self assembly of self-limiting, monodisperse supraparticles from polydisperse nanoparticles, *submitted*.

strength between the NPs increasing monotonously with the aggregate size balances with their net attraction. We further demonstrate that the remarkable amount of NP polydispersity helps stabilize the formation of the core-shell structure.

4.2.2 Experiment results from Kotov group

Cadmium selenide (CdSe) NPs stabilized by short and highly charged citrate anions were adopted as an initial model system because of their well-established optical properties, and the possibility to combine strong electrostatic and van der Waals interactions. The NPs are polycrystalline and have irregular spherical shapes with no pronounced facets or anisometry. Growth and assembly of CdSe NPs occurred simultaneously in aqueous solution at 80°C. When necessary the reaction was slowed down or interrupted by cooling the reaction media. Within 20 min of the reaction, one can clearly observe SPs with a median diameter d_{SP} = 22±2.4 nm and size distribution δ_{SP} = 11%, as determined by transmission electron microscopy (TEM). The constituent NPs have average diameter d_{NP} = 2.9 ± 0.7nm and TEM size distribution δ_{NP} = 25%.

As the reaction progresses, the SPs grow in diameter to 33±2.5 nm, 42±3.5 nm and 49 ± 4.1nm for 120, 1080, and 2400 min reaction times, respectively. Approximating the TEM diameters, we refer to these samples as CdSe-30, CdSe-40, and CdSe-50. During the reaction, the NPs within the SPs increase in size to 3.5±0.80 nm in CdSe-30, 4.5±1.1 nm in CdSe-40, and 5.4±1.4 nm in CdSe-50. The reduction of the polydispersity in SPs (8-10%) compared to the individual units of which they are comprised (25-30%) occurs in all samples, as confirmed by several independent experimental techniques.

The intermediate stages of the assembly process were monitored at 40°C. We observed that CdSe first nucleates and grows to form individual NPs (Figure 4.17(a)). Next, some NPs assemble into elongated aggregates (Figure 4.17(b)) which later evolve into loose, more isometric clusters comprised of 15-25 NPs. Finally, the intermediate clusters undergo compaction to produce denser and more monodisperse SPs (Figure 4.17(d)). The same sequence of assembly stages is also deduced from the combination of dynamic light scattering and UV-vis absorption data cumulatively expressed in Figure 4.17(e), trace 1. The size ratio dSP/dNP initially increases following the transition from individual NPs to loose clusters. After that, d_{SP}/d_{NP} decreases when the clusters get compacted.

The internal structure of individual SPs is investigated by fitting the scattering function data from experiments with that calculated from a core-shell model. Starting from an aggregate with a dense packing of NPs with the size distribution of 25%, the NPs in the core of the aggregate are randomly removed one by one. The scattering function is then calculated for

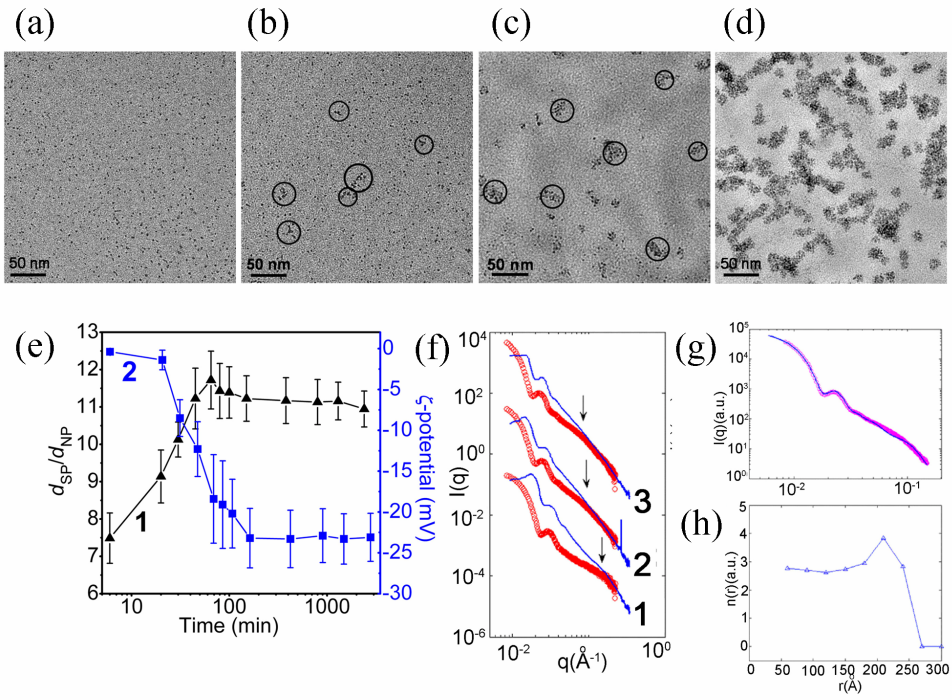

Figure 4.17 Intermediate stages of formation of SP at 40°C (a-d) and detailed structural characterization of SPs (e-h). 5 min (a), 9 min (b), 15 min (c), and 19 min (d). (e) The experimental dependence of dSP/dNP and the electrokinetic ζ-potential on reaction times. d_{SP} and d_{NP} were measured by DLS and UV-vis spectroscopy, respectively. Electrokinetic ζ-potential was measured by DLS. (f) SAXS curves for CdSe-30 (1), CdSe-40 (2), and CdSe-50 (3) SPs. Red and blue lines represent solution and dried samples, respectively. Inflection points are marked by arrows. (g) The measured data for CdSe-50 in solution (magenta) and calculated curves from core-shell SP model (blue). (h) The radial distribution of the number of subunits for core-shell SP model for CdSe-50. Experimental results are produced by Kotov group.

the remaining NPs after each removal. The process finishes when the calculated scattering function matches well with the experimental data (Figure 4.17(g)). The radial distribution of the number of NPs for final core-shell SP aggregate is measured, revealing a core-shell morphology (Figure 4.17(h)).

That the polydisperse NPs assemble into monodisperse, spherical SPs rather than aggregates or precipitates with a broad size distribution and/or irregular shapes, suggests that the agglomeration of the NPs here is both thermodynamic and self-limiting. Considering the high negative charge of the citrate-stabilized NPs, it is logical to assume that electrostatic interactions play an important role in the self-limiting behavior of the otherwise attractive NPs. Indeed, investigation of the evolution of the electrokinetic ζ-potential during the formation and maturation of SPs (Figure 4.17(e)) shows that, although initially small (0-5 mV), it increases substantially as the SPs grow, and stabilizes when the SPs reach the stage

of compact assemblies. Thus we hypothesize that the reason for the ultimate cessation of SP growth is the strong electrostatic repulsion between SPs and between SPs and NPs, which must ultimately balance the van der Waals attraction between NPs. We then perform mesoscale simulations on a coarse grained model of the NPs to systematically test different combinations of forces, NP shapes, and assembly conditions that might be reasonably expected in this system.

4.2.3 Simulation

Model

The primary interactions between NPs in this system are expected to be excluded volume interaction, van der Waals attraction and screened electrostatic repulsion. The potential energy between two NPs can thus be modeled as:

$$U(r) = 4\varepsilon\left[\left(\frac{\sigma}{r}\right)^{12} - \left(\frac{\sigma}{r}\right)^{6}\right] + A\frac{\exp(-\kappa r/\sigma)}{r/\sigma} \tag{4.5}$$

where r is the center-center distance between two NPs. The excluded volume and van der Waals attraction is modeled by the Lennard-Jones 12-6 potential, truncated and shifted to zero at $r_C = 2.5\sigma$. The screened electrostatic repulsion is modeled by the Yukawa potential with A being the strength of the electrostatic repulsion. A is proportional to the particle surface charges and inverse of medium dielectric constant; κ is the inverse screening length; ε is the van der Waals attraction strength; and σ is the length unit. For the interaction distance r_{ij} between particles i and j with different diameters d_i, and d_j, respectively, is $r = r - [(d_i + d_j)/2 - \sigma]$. The attraction strength, $\varepsilon = k_B T(d_i^3 + d_j^3)/2\sigma^3$, is proportional to the volume of the interacting particles.

At a given reduced temperature $T^* = k_B T/\varepsilon$, we find there is a value of the repulsion strength $A = A_{agg}$ below which the NPs aggregate as the electrostatic repulsion becomes weaker than the van der Waals attraction. Since the van der Waals attraction strength between NPs varies with their size, A_{agg} depends, in principle, upon the NP size. For the range of NP polydispersity of interest, i.e. $\delta_{NP} < 30\%$, we used an average value of A_{agg} averaged over all particle polydispersities and observe the dependence of A_{agg} upon T^* (Figure 4.17). Without any loss in generality, we simulated the system at $A_0 = 1.0k_B T$ and $T^* = 0.2$, for which A_{agg} is approximately $6.0k_B T$.

To capture, in a coarse-grained way, the influence of the collective electrostatic interaction of NPs within a SP on approaching NPs, we postulate that the repulsion strength A

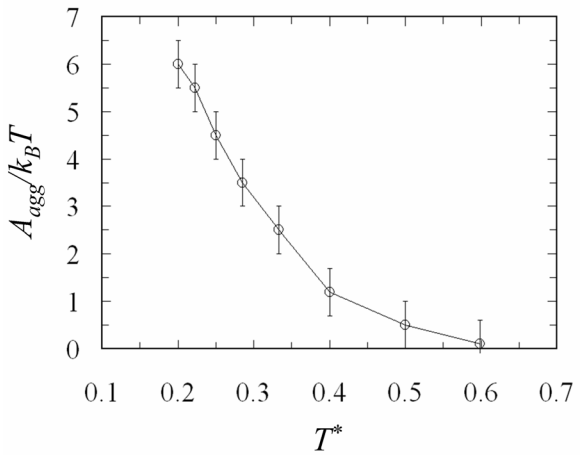

Figure 4.18 Dependence of the segregating/aggregating repulsion strength A_{agg} on T^*, averaged over different values of polydispersity δ_{NP} = 0%, 10%, 20% and 30%. Error bars are standard deviations from the mean value.

should vary with the volume of the SPs to which each NP belongs. To a first-order approximation, we can assume a linear relationship between A and the total volume of the NPs in an SP, V. We denote V_{max} as the SP volume at which $A = A_{agg}$. Consider two NPs belonging to SP i and j, whose size is V_i and V_j, respectively. The possible interparticle interactions (corresponding repulsion strength and inverse screening length) are summarized in Table 4.2. Here we define $s = (A_{agg} - A_0)/(V_{max} - V_{NP})$ as the rate of change of the electrostatic repulsion with respect to the aggregate volume during assembly, where $V_{NP} = \pi\sigma^3/6$ is the average NP volume. We should note that in our model s (and V_{max}) is an input parameter and not calculated from the intrinsic properties of the nanoparticle system.

Simulation method

To carry out the simulation, a fixed number of NPs are initially placed at random locations in a cubic box with periodic boundary conditions. We use Brownian Dynamics (BD) to simulate the time evolution of the system under conditions of constant volume and constant temperature. Further details on the Brownian dynamics simulation method can be found in Chapter 2. During a simulation run, we look for the SPs formed in the box every 1000 time steps. The cutoff distance used to partition the NPs into SPs is chosen to be 1.4σ to take into account thermal noise and size polydispersity while minimizing the probability of counting different but nearby SPs as one cluster.

To ascertain whether the predicted SP assemblies represent thermodynamic equilibrium structures, we simulate different numbers of particles varying from 100 to 10000 particles

Table 4.2 Interparticle interaction parameters depending on the cluster volume that the particles residing as well as the relative position of the particles with respect to the cluster center of mass.

i and j in the same cluster	
$V_i \leq V_{max}$	$A = A_{agg}$ $k = k_{solvent} = 0.2\sigma^{-1}$
$V_i > V_{max}$	In the core: $A = A_{inner} > A_{agg}$ $k = k_{inner} = 0.1\sigma^{-1} < k_{solvent}$ In the shell: $A = A_{agg} V_i / V_{max}$ $k = k_{solvent}$
i and j from different clusters	
$V_i \leq V_{max}$; $V_j \leq V_{max}$; $V_i + V_j < V_{max}$	$A = A_0 + (V_i + V_j - V_{NP})(A_{agg} - A_0)/(V_{max} - V_{NP})$ $k = k_{solvent} = 0.2\sigma^{-1}$
$V_i \leq V_{max}$; $V_j \leq V_{max}$; $V_i + V_j > V_{max}$	$A = A_{agg}$ $k = k_{solvent}$
$V_i \geq V_{max}$ or $V_j \geq V_{max}$	$A = A_{agg}(V_i + V_j)/V_{max}$ $k = k_{solvent}$

from different initial conditions and random seeds, and at different concentrations. We also gradually compressed the box size to increase the NP density from ≈ 0.01 to ≈ 0.1, and observed that SPs of size V_{max} do not merge. The rate of change of the charge-charge repulsion strength with respect to the SP volume, s, varies from $0.02k_BT/V_{NP}$ to $0.4k_BT/V_{NP}$, corresponding to V_{max} varying from $250V_{NP}$ to $13V_{NP}$, respectively. The natural units are the mean particle diameter σ, particle mass m, and Lennard-Jones well depth, ε. The time unit is then defined as $\tau = \sigma\sqrt{m/\varepsilon}$. The time step used in our BD simulations is chosen to be $\Delta t = 0.005\tau$. The screening length $1/\kappa$ is chosen to be 5.0σ for the particles in the shell and outside the clusters, and 10σ for the particles in the core. For our NP system, the typical values of these parameters are σ = 5nm, ε = 50-60kJ/mol, T = 300K and $m = 10^{-21}$kg. In the case where the NPs are considered to have non-negligible dipole moments, we model the dipole by a pair of oppositely charged $(+/-q)$ points separated by a distance (d) within each spherical NP, and with dipole moment 10D, 100D and 1000D. The systems are equilibrated for $(50-100)\times 10^6$ time steps until the potential energy plateaus, corresponding to approximately a time span of 2-5ms.

Results and discussion

Based on all simulation runs, we found that the case of spherical NPs with $\delta_{NP} = 20\%$ interacting only via repulsive electrostatic and attractive vdW forces describes the assembly process nearly perfectly. We find that simulated systems of NPs with $\delta_{NP} = 0 - 30\%$ follow the same assembly stages as in experiments (cf. Figure 4.19(a) and Figure 4.17(a-d)). At the final stage, the monodisperse SPs are close to spherical in shape (Figure 4.20). The size distributions at sV_{NP}/k_BT = 0.05; 0.067 and 0.1 exhibit a sharp peak at V_{max} = $100V_{NP}$; $75V_{NP}$ and $50V_{NP}$, respectively (Figure 4.21), confirming that the SPs are uniform in size with different increasing rates of the repulsion strength. As s increases, the value of V_{max} at which $A = A_{agg}$ decreases, indicating that the SPs will have a smaller self-limiting size. From experimental results of CdSe-50 (i.e. the stable state), the average SP diameter is approximately 10 times bigger than the average NP diameter, giving $V_{max} \approx 1000V_{NP}$ and $s \approx 0.005k_BT/V_{NP}$.

The spikiness of the real SPs as compared to the simulated SPs is likely due to the fact that NPs can continue to grow after their assembly into SPs, especially those in the outer shell of a SP. This growth should be anisotropic due to a higher concentration of ions outside the SPs, and a tendency for radially outward growth of NPs in the outer shell of the SPs. Once a SP reaches a size where the electrostatic repulsion energy between NPs in the SP and the newly arrived NPs outside the SP equals the attractive energy associated with vdW interactions, the agglomeration stops. Importantly, we find that self-limiting behavior occurs only if the electrostatic repulsion increases monotonically with the volume of the SP being assembled. Otherwise, NPs continue to aggregate, regardless of screening length.

SPs assembled *in-silico* from NPs with $\delta_{NP} = 20\%$ exhibit a sharp peak in the cluster size distribution (Figure 4.19(b)) at a single value of d_{SP}, reproducing the size monodispersity observed in experiments. The size distribution of the simulated SPs is fitted well by a normal distribution with standard deviation of 8% (Figure 4.19(b)), which is very close to the experimentally observed size distribution. The plateau system potential energy (Figure 4.22) indicates that the system is at steady state. Additionally, the fluctuation in the average number of NPs per SP around V_{max} (Figure 4.22, inset) implies that the particles are able to attach to and detach from the SPs under thermal noises, and that the formation of multiple separate SPs is not a kinetically trapped configuration but a thermodynamic equilibrium state. To further ensure that the SPs are not a consequence of kinetic effects, we gradually increase the NP packing density from ≈ 0.01 to ≈ 0.1 to reduce the average distance between the SPs, and observe that the SPs do not merge into larger SPs, as would be the case if the observed configuration were not in thermodynamic equilibrium. The time evolution of the asphericity parameter (Figure 4.23, left) and SP volume (Figure 4.23, right)

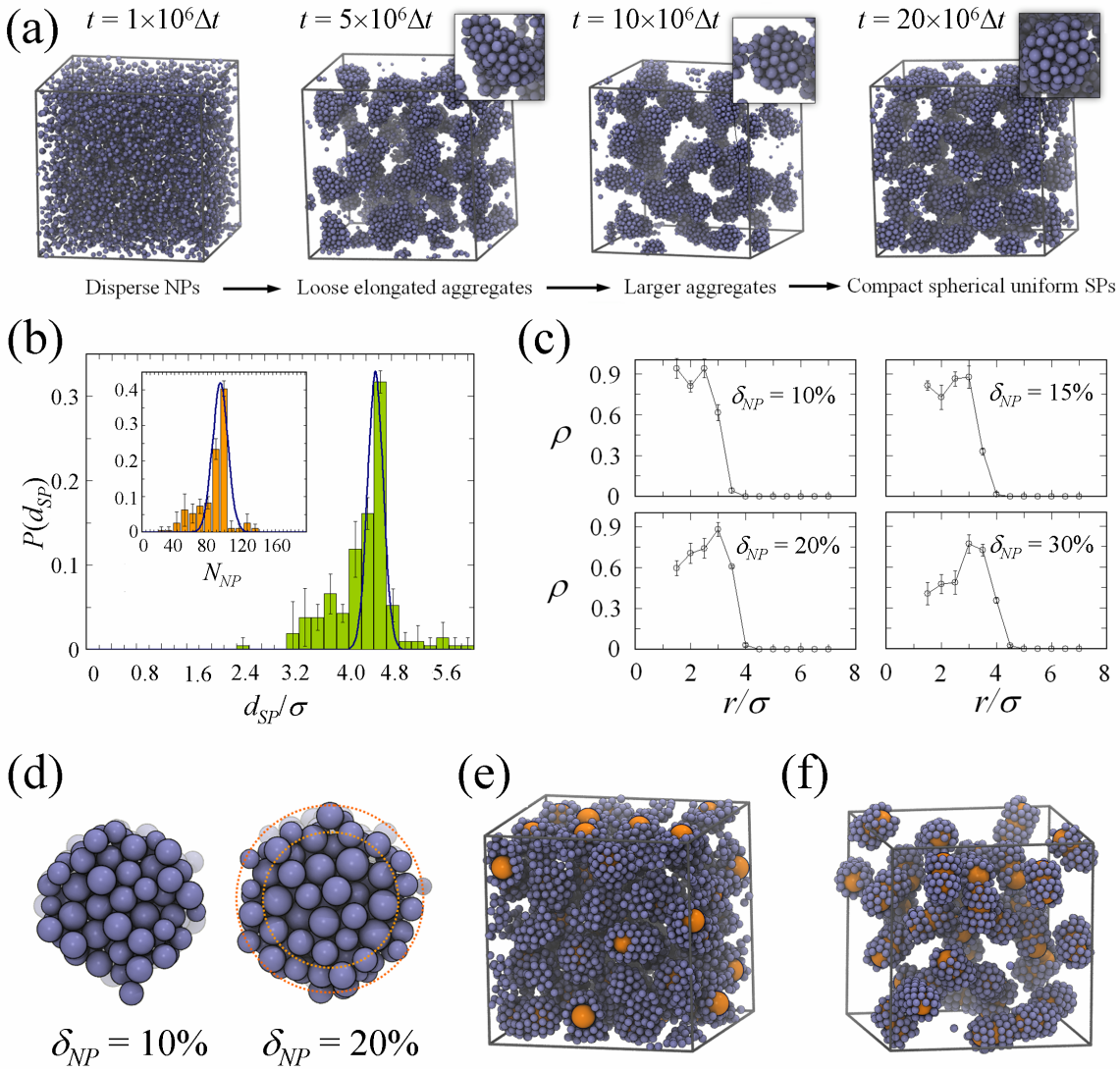

Figure 4.19 (a) Assembly stages over time. The asphericity parameter of the simulated SPs in the final stage of assembly is 0.014±0.006. (b) Size distribution of the simulated SPs assembled from NPs with δ_{NP} = 20%, fitted by a 8% standard deviation Gaussian distribution (blue curve). Inset is the distribution of the number of NPs in an SP. (c) Particle density vs. distance, r, from SP center, scaled by NP average diameter, σ. (d) Snapshot of a typical simulated SP for two different NP polydispersities. (e) Computer simulation of core-shell SPs self-assembled from CdSe NPs (blue) and preformed Au NPs (orange); (f) Computer simulation of core-shell SPs self-assembled from CdSe NPs (blue) and pre-formed Au nanorods (orange).

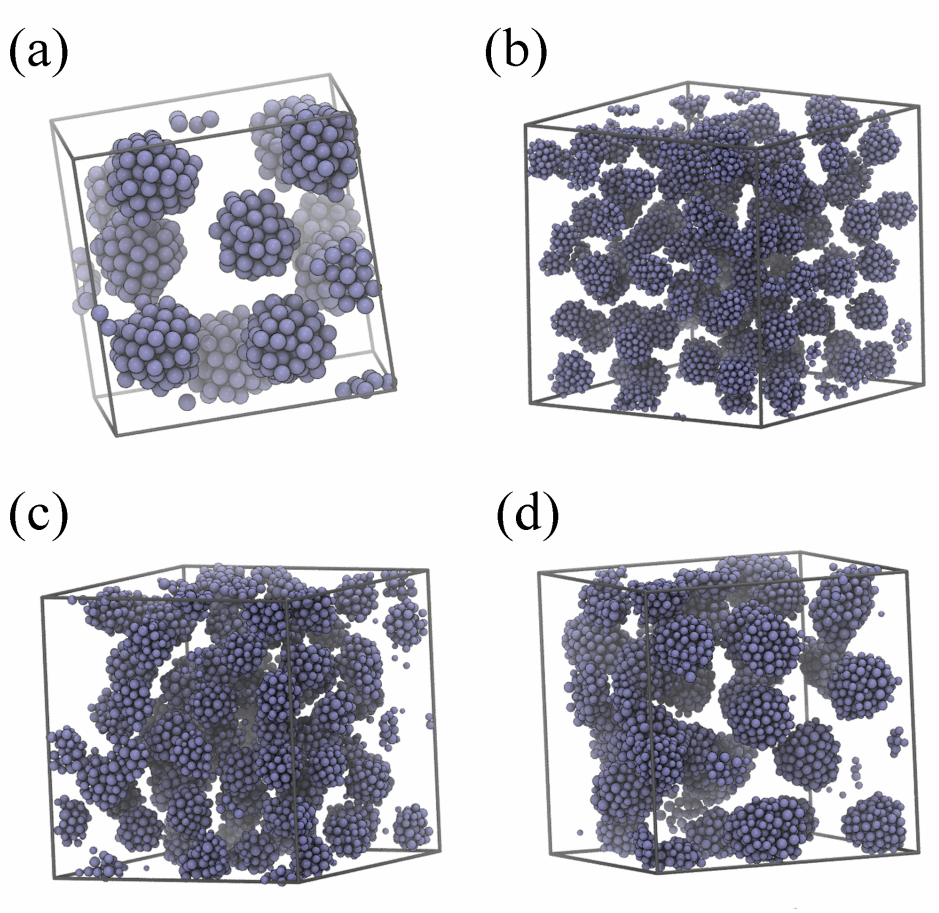

Figure 4.20 Snapshots of 1000-10000 particle systems at different packing densities (ϕ): (a) $\phi = 0.05$: $s = 0.05 k_B T / V_{NP}$, δ_{NP} = 0%, N = 1000; (b) $\phi = 0.007$: $s = 0.05 k_B T / V_{NP}$, δ_{NP} = 20%, N = 10000; (c) $\phi = 0.1$: $s = 0.067 k_B T / V_{NP}$, δ_{NP} = 20%, N = 5000; and (d) $\phi = 0.1$: $s = 0.025 k_B T / V_{NP}$, δ_{NP} = 20%, N = 5000.

reveals that the SPs become more spherical in shape and uniform in size. At the final stage, the SPs are close to spherical in shape with the asphericity parameter of 0.014 ± 0.006.

We note that the reduction in the size polydispersity of the SPs is partially explained by the Central Limit Theorem (CLT)[58] which predicts that the polydispersity of the group (i.e. SP size) of random variables (i.e. NP size) is smaller than that of the random variables by the square root of the number of variables in the group. However, CLT does not predict the mean value of the group, or in other words, CLT does not explain why the SP size converges to a single finite value in our system. We therefore argue that the uniform size of the SPs does not result from statistics, but from the self-limiting nature of the assembly.

Our simulations also reproduce the internal structure of the SPs inferred from the TEM and SAXS measurements. The core-shell structure of the SPs clearly emerges for $\delta_{NP} = 20 - 30\%$ (Figure 4.19(c)), with a disordered packing of the NPs in the core (Figure

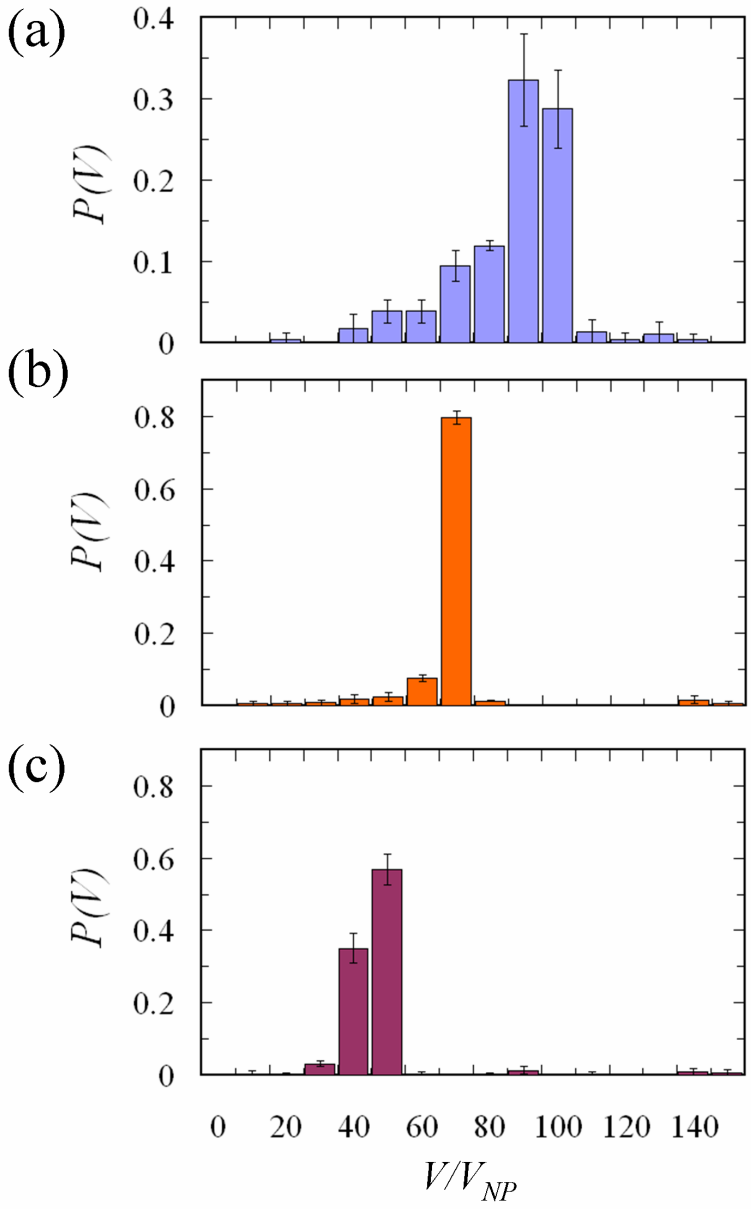

Figure 4.21 Size distribution of N = 5000 NPs with polydispersity δ_{NP} = 20% at different rates of change in the repulsion strength A with respect to the SP volume, s: (a) $s = 0.05 k_B T / V_{NP}$; (b) $s = 0.067 k_B T / V_{NP}$; and (c) $s = 0.1 k_B T / V_{NP}$. The greater the value of s, the smaller the size of the SPs because the repulsion strength reaches A_{agg} more rapidly.

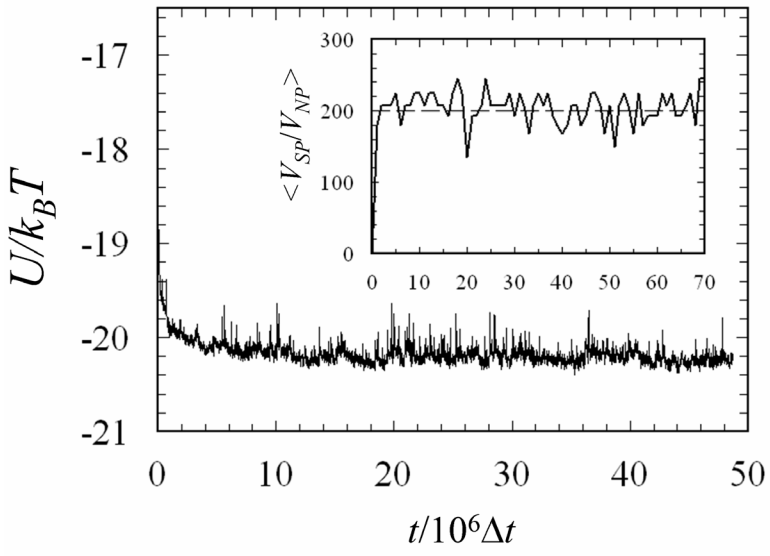

Figure 4.22 Per particle system potential energy during aggregation from disperse NPs. Inset: Average total volume of NPs in an SP during aggregation. The fluctuation indicates that the NPs are able to attach to/detach from the SP, a key feature of thermodynamic equilibrium.

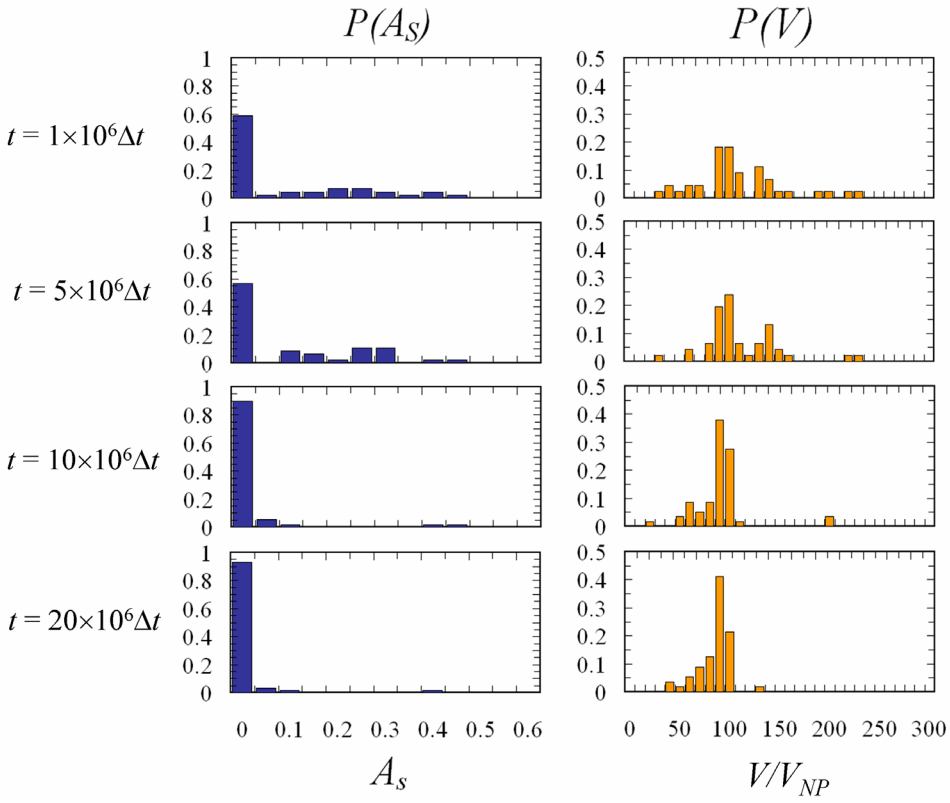

Figure 4.23 Time evolution of the asphericity parameter (left) and size distribution of the simulated SPs (right) during the assembly process. The asphericity parameter A_S varies from zero for perfectly spherical aggregates to unity for cylindrical aggregates.

4.19(d)). For $\delta_{NP} = 20\%$, the simulated packing densities in the core and in the shell are (74±7)% and (89±5)%, respectively; these values correlate well with experiments for the CdSe-50 case. The strong electrostatic repulsion inside the SPs gives rise to the loosely packed core of the SPs; additionally, the remarkable NP polydispersity leads to NP re-arrangement within the SPs such that smaller NPs pack in the outer shell and larger NPs concentrate in the core (Figure 4.19(c)). Further, we observe that the NPs in the shell are more polydisperse than those in the core, which explain the surprisingly high packing density in the shell (Figure 4.24). It is also important to note that when the analogous simulations were run with different NP geometries or different forces (spherical and tetrahedral NPs, with and without dipole interactions, and with and without polydispersity) (Figure 4.25 and 4.26) the geometry of the resulting agglomerates was markedly different from monodisperse spherical SPs.

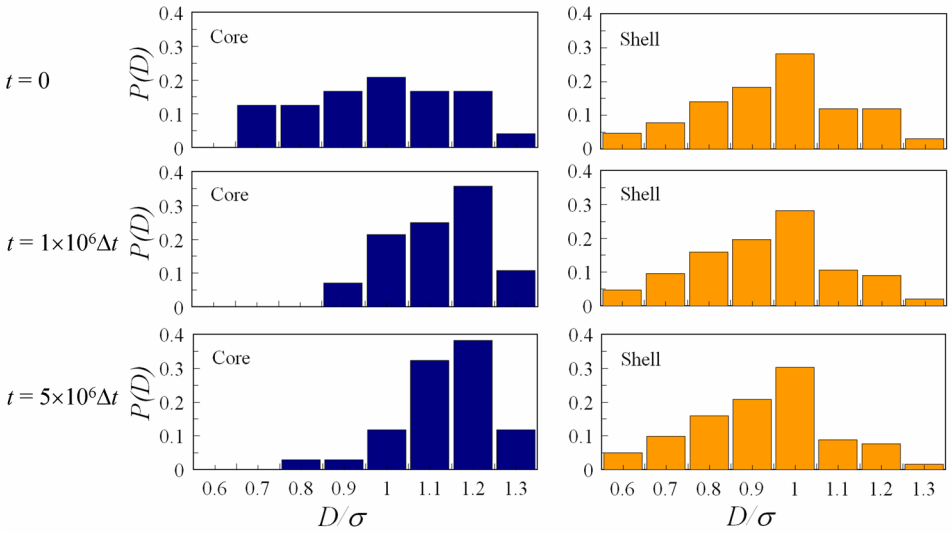

Figure 4.24 Time evolution of the size distribution of the NPs in the core and in the shell showing the re-arrangement of the NPs within an SP. Assuming the NPs are initially randomly distributed throughout the SP, after $(5-10) \times 10^6$ time steps, the NPs in the shell are smaller and more polydisperse (δ_{NP}^{shell} = 15%) than those in the core (δ_{NP}^{core} = 10%).

It is interesting that the NPs form uniform size, core-shell and spiky SPs instead of twisted ribbons, sheets and wires as previously found in other almost identical NP systems[14, 24, 134]. The main reason is attributed to the fact that the CdSe NPs here are stabilized by citrate, a weaker stabilizer as compared to the stabilizers used in previous studies, i.e. TGA and DMAET. This leads to (1) the isotropic van der Waals attraction much stronger than anisotropic charge-dipole and dipole-dipole interactions, (2) stronger charge-charge repulsion and (3) more polydisperse NPs as compared to previously studied NP systems. It is the strong isotropic van der Waals interaction that gives rise to the formation of spherical aggregates. Meanwhile, the strong charge-charge repulsion results in a

greater contribution of many-body effects to the pair-wise particle interaction. The collective electrostatic repulsion coming from the NPs in an SP to approaching NPs, once balanced by the van der Waals attractions, hinders further particle aggregation, resulting in the upper limit of the SP size. It is important to note that the key condition for the self-limiting aggregation is the monotonously increasing repulsion strength A with respect to the aggregate volume V up to A_{agg} at a given temperature T^*. This is consistent with the variation of the electrokinetic potential during the assembly process obtained from experiments (4.17(e)). Note that without the modification in the repulsion strength as a function of V there is no upper bound in the SP size, even with a longer range of the charge-charge repulsion.

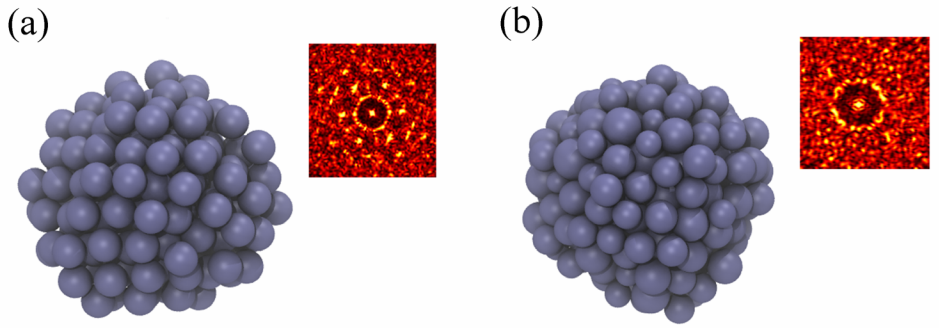

Figure 4.25 (a) Monodisperse NPs form SPs with ordered local packing; (b) NPs with polydispersity of 20% pack into SPs with amorphous local packing. Insets are the corresponding diffraction patterns. Both structures are obtained from simulation runs where the electrostatic repulsion is stronger inside the SP than outside.

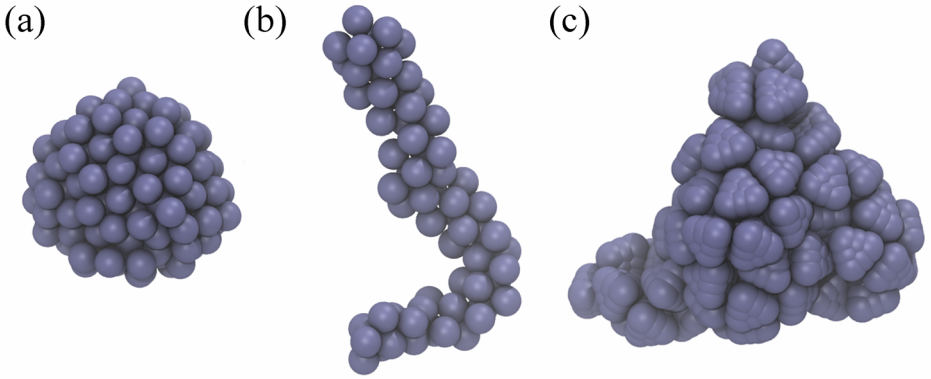

Figure 4.26 Simulations of (a) monodisperse, spherical NPs with dipole moment 100D assemble into monodisperse SPs without core-shell internal structure; (b) Monodisperse, spherical NPs with dipole moment 1000D form chain-like structures; (c) Tetrahedral NPs without dipole moment form non-spherical aggregates. The structures are obtained at $T^* = 0.2$.

The local packing of the NPs within an SP is influenced by the particle polydispersity and the difference between the charge-charge repulsion inside and outside the SP. The particle polydispersity allows for the energetic difference between the aggregation of big

and small NPs. Since the van der Waals interaction between nanometer-sized NPs scales with the particle volume, the size polydispersity of 20-30% is sufficient for the demixing of NPs with different sizes. Additionally, due to the high charge density and long screening length in the core (i.e. $A_{inner} > A_{agg}$), the inner particles are loosely packed and are able to re-arrange to minimize the free energy. The smaller particles tend to move outwards to gain additional entropy instead of being trapped among big particles. In the shell, the charge-charge repulsion between the smaller NPs becomes weaker because they are exposed to the solution with higher dielectric constant. In the opposite direction, the bigger particles are to move inwards to maximize their contacts while minimizing their exposure to the solution. Therefore, at equilibrium, the smaller NPs pack densely in the shell and the bigger pack more loosely in the core, as observed by experiments.

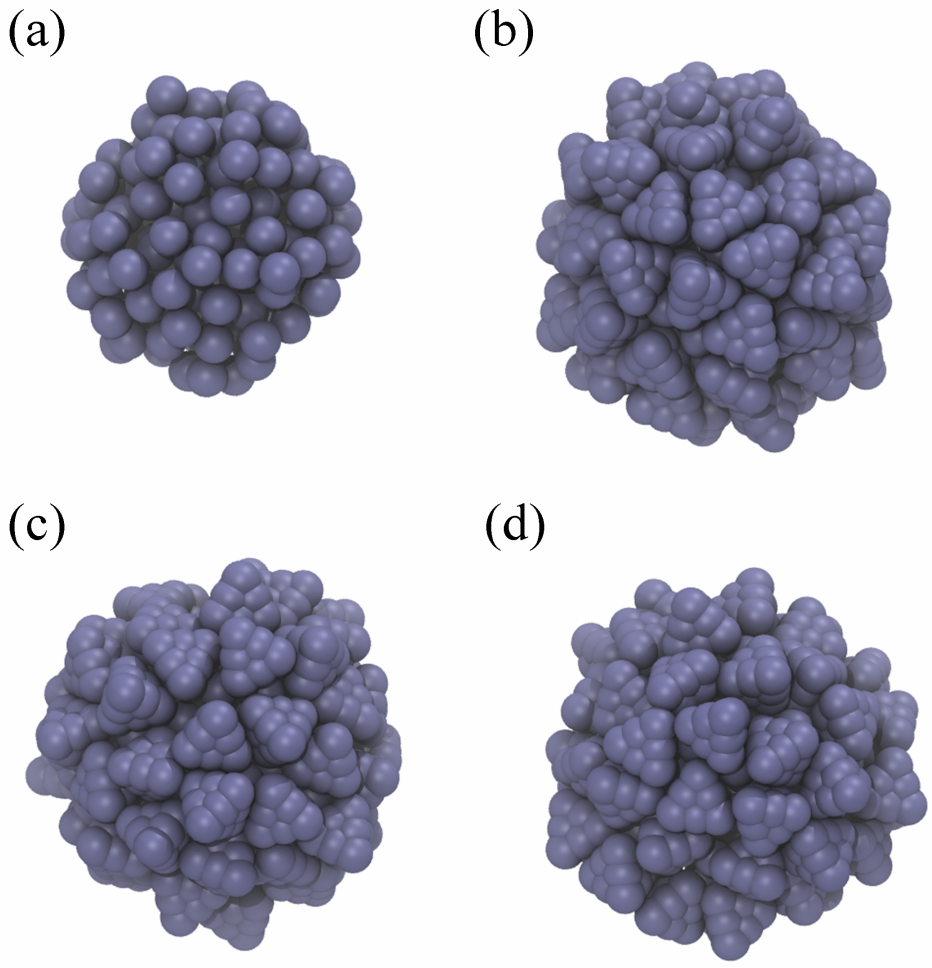

Figure 4.27 SPs resulting from the shape change of the NPs in the shell from spheres to tetrahedra with different growth rates. (a) Initial SP with spherical NPs; (b-d) Resulted SPs: (b) fast growth rate; (c) intermediate growth rate and (d) slow growth rate.

The spiky shell of the SPs is related to the anisotropic growth and closely packed of the

NPs in the shell. As shown in Figure 4.27 when the NPs in the shell grow into tetrahedra, the shell becomes more spiky than the bumpiness of the initial spherical SPs. The NPs in the shell are subject to the strong charge-charge repulsion coming from the NPs in the core, and therefore can gain material mostly from outside. Because the NPs in the shell are already densely packed by their strong van der Waals attraction, they cannot re-arrange themselves to have more face-to-face contacts. Consequently, the NPs in the final shape are trapped in place with their growing part pointing outwards. It follows that the formation of the spikes involves mainly the direction on which the NPs in the shell grow.

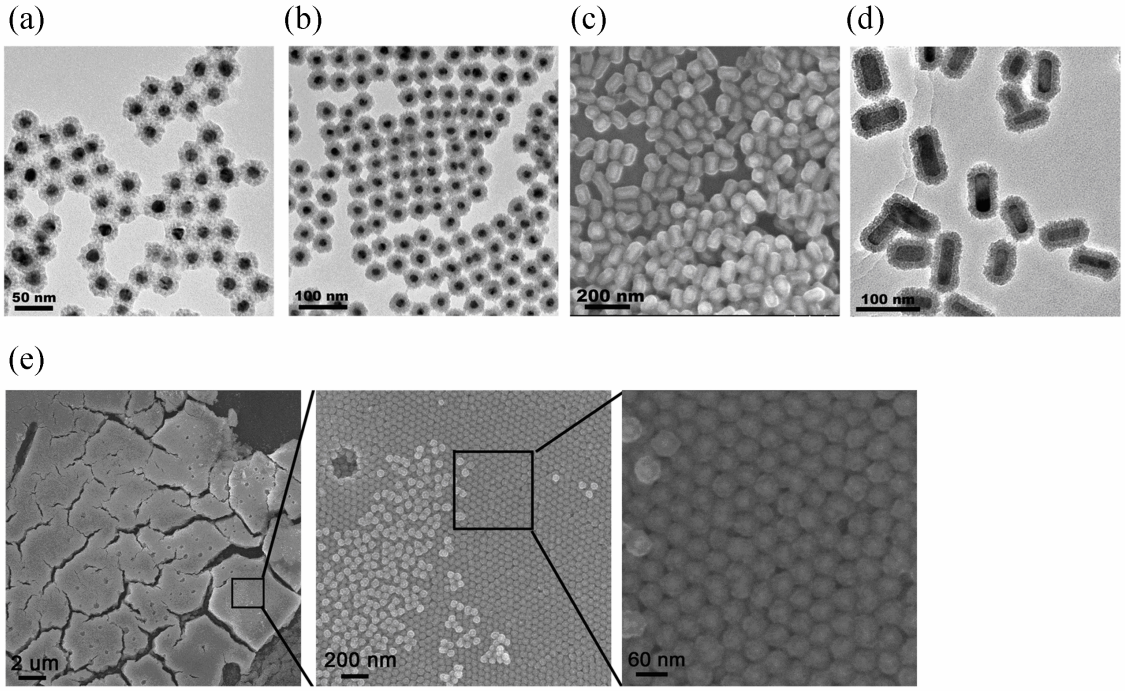

Figure 4.28 Analogous SP assemblies from different materials. TEM and SEM images from CdS (a) Au-NPs/CdS, (b) Au-NPs/CdSe, (c) Au-nanorod/CdS and (d) Au-nanorod/CdSe SPs; (e) SEM image of colloidal crystals from Au-NPs/CdSe SPs. Experimental results are produced by Kotov group.

The forces leading to the formation of monodisperse SPs are general and the approach should be applicable to a large variety of ”imperfect” NPs from other materials. Indeed, similar SPs form from II-VI semiconductors, such as CdS and ZnSe, and from IV-VI semiconductors, such as PbS. Considering the simple balance of forces, we further hypothesized that similar self-limiting structures might form around pre-existing cores. In practice, such cores may be realized through like-charged particles capable of strong van der Waals attraction with NPs in the solution. We note this strategy is opposite to the often-used strategy of employing nanocolloids of opposite charge as core particles[151, 152]. To test our hypothesis, we added Au NPs with $d < d_{SP}$ stabilized by citrate with an electrokinetic

potential of -39.4 mV to a solution of CdSe NPs prior to their assembly into SPs. We indeed observed the assembly of hybrid SPs with a single Au core surrounded by CdSe NPs (Figure 4.28(d-f)). The use of pre-formed cores offers the possibility to further increase the complexity of SPs and can lead to easy-to-make superstructures with a rich variety of geometries and functionalities. The produces metal-semiconductor SPs can self-assemble further into colloidal crystals producing unique hierarchical assemblies and multiple applications (Figure 4.28(e))[142, 144, 147]. We also found that anisotropic Au nanorods yield equally monodisperse cylindrical SPs both in experiments (Figure 4.28(c-d)) and simulations (Figure 4.19(f)). Our work demonstrates that NPs can organize with similar levels of complexity as viruses albeit following a wholly different assembly pathway without any directional interactions specific for proteins and other biomolecules, but instead by a simple balance of generic Coulombic and van der Waals forces. The self-limiting state also distinguishes the SPs found here from self-limiting, "magic number" clusters known for monodisperse nano- and micro-particles[153, 154].

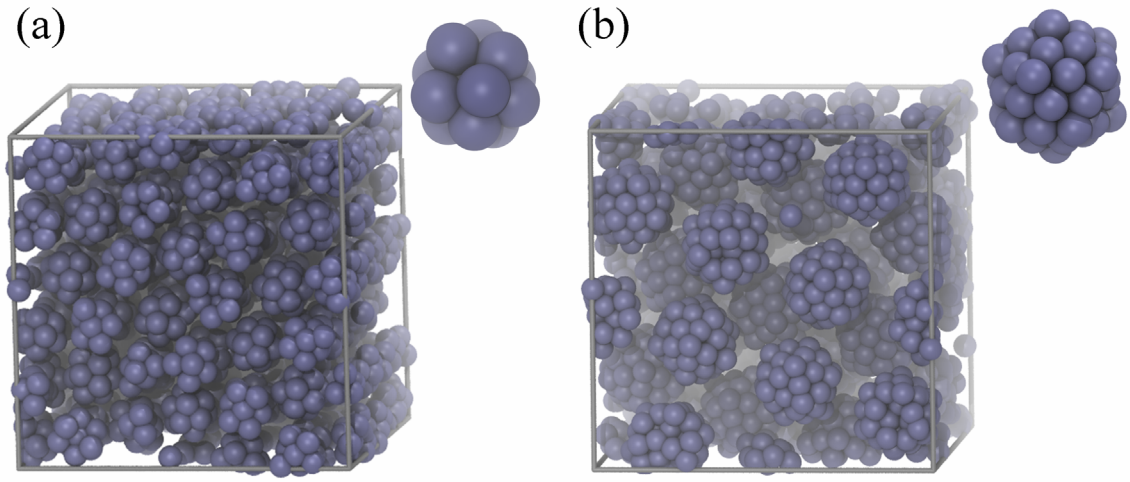

Figure 4.29 Self-limiting SPs at high density (a) each consisting of (a) 13 NPs and (b) 55 NPs. A representative SP for each case is shown in the inset.

We perform additional simulations to demonstrate that our simulation model is capable of capturing the behavior of the SPs beyond self-limiting aggregation. As shown in Figure 4.29, uniform SPs assembled from 13 NPs (Figure 4.29(a)) or 55 NPs (Figure 4.29(b)) crystallize into a face-centered cubic crystalline structure, consistent with experiments. The insets further reveal that individual SPs acquire the minimum potential energy configuration corresponding to 13- and 55-atom clusters. This is interesting because all SPs are able to achieve energy minimum configurations independently without kinetic barriers. This also suggests one possibility that self-limiting aggregation plays an important role in stabilizing energy minimizing clusters for certain cases.

We should note that our present model is developed based on the assumption that the self-limiting aggregation is isotropic. If the simulation model is extended to be anisotropic, i.e. the aggregation is limited in a particular direction, presumably due to the directional interaction between the NPs, we can expect the resulted SPs would have non-spherical morphologies, for example, the twisted bilayer ribbons formed by CdTe tetrahedra in the work of Srivastava et al.[14]

4.2.4 Conclusion

We have shown that polydisperse NPs assemble into monodisperse spherical SPs via a self-limiting aggregation process governed by the balance between generic forces, i.e. van der Waals attraction and Coulombic repulsion. That the resulted SPs are in equilibrium and consist of hundreds of NPs distinguishes the self-assembly process here with kinetically trapped processes, where uniform size aggregates emerge but do not interact with each other (because of dilute concentration and low temperature), and with energy minimizing clusters consisting of tens of NPs. The generic model we developed can be used to explain the aggregation behavior of various inorganic/organic systems. Furthermore, our simulations reveal the dynamics of the aggregation process, particularly of the formation of the core-shell structure, which was previously unclear in experiments. The same mechanism of SP assembly shown here can be further exploited for the experimental engineering of sophisticated nanoscale systems combined with their design and testing in-silico, while hierarchically organized colloidal crystals of SPs will open the door to complex macroscale hybrid materials that are simple to prepare.